ESA Working Paper EWP-2384

GOCE gradiometer calibration and Level 1b data processing

Dr.-Ing. Christian Siemes
ESA Research Fellow
EOP-SME
Noordwijk, The Netherlands - 21 Nov 2011

ESA Working Paper EWP-2384

This work was performed by Christian Siemes during his tenure of European Space Agency Internal Research Fellowship at the European Space Technology and Research Centre (ESA-ESTEC), under the supervision of Roger Haagmans in the Earth Surfaces and Interior Section (EOP-SME) of the Mission Science Division of the Earth Observation Programmes Directorate.

The report contains a selection of results from the scientific research performed during the period January 2010 – November 2011 and fulfils the requirements for completion of the ESA Research Fellowship programme.

Preface

GOCE was launched on 17 March 2009, with various first-of-its-kind technologies on board. Some months after launch, it was discovered that some of these technologies, for example the along-track drag-free control, were performing much better than expected pre-launch. In particular, the performance of the gravity gradiometer was not entirely as expected pre-launch. While the gravity gradients were more accurate than expected at lower frequencies, the measurement noise in the gravity gradient V_{zz} was worse than expected from pre-launch simulations. For these reasons, it was decided to revisit the algorithms for the gradiometer level 1b processing and to investigate the performance of the gradiometer including its calibration. It started from earlier ideas applied to simulated data before launch. Major improvements were necessary when dealing with real data. The investigations showed that significant improvements in GOCE level 1b and level 2 products could be achieved due to a different way of calibrating the gradiometer data and processing of level 1b data. The research fellowship contributed, together with the work of Claudia Stummer of the Technische Universität München, to the upgrade of the official GOCE level 1b processor, bringing the GOCE mission 10–20% closer to reaching its mission goals.

The results presented in this report are submitted for publication in two journal papers: [Siemes et al.(2011)] and [Stummer et al.(2011)]. The contents of the papers is reorganized for better reading and extended for completeness. Naturally, this means that large parts of this report are identical to parts of the papers.

It is worth noting that the original idea for the research fellowship is related to the time series analysis of Swarm magnetic field models for a fast quality check with special emphasis on vector field magnetometer and absolute scalar magnetometer data. A few months after the start of the research fellowship, it became clear that the launch of the Swarm satellites, originally foreseen in mid 2011, would be delayed. At the same time, the performance of the GOCE gradiometer was not entirely as expected pre-launch. Since the cause of this behaviour was unknown, it was agreed to change the focus of the research fellowship to investigating the performance of the GOCE gradiometer. It should be mentioned that many software modules developed during the research fellowship for GOCE data analysis can be easily adapted for Swarm data analysis. One example is the module for deriving a gradiometer-only GOCE level 2 product from level 1b data, which was in fact originally developed for Swarm mission data at the beginning of the research fellowship and then adapted for GOCE mission data. Another example is that every software module (and analysis) related to the attitude measurements can be used for the GOCE and the Swarm mission since in both cases each satellite carries three star sensors as payload.

Contents

1 Introduction

The mission objectives of the Gravity field and steady-state Ocean Circulation Explorer (GOCE) are the determination of the gravity anomaly field with an accuracy of 1 mGal and the geoid with an accuracy of 1–2 cm, and achieving both at a spatial resolution of 100 km half wavelength [Drinkwater et al.(2007)].

The GOCE satellite is equipped with innovative instruments. The electrostatic gravity gradiometer measures the medium to short wavelength signal of the gravity field and the non-gravitational accelerations acting on the satellite. The satellite-to-satellite tracking instrument determines the position and velocity of the satellite and is used for the estimation of the long wavelength signal of the gravity field. Three star sensors provide the satellite attitude while three magnetic torquers are used for attitude control. The ion thruster assembly compensates for non-gravitational accelerations in the along-track direction. The above mentioned sensors and actuators form the drag-free and attitude control system, which is together with the thermal control responsible for providing the quiet environment necessary for the optimal performance of the gradiometer. Furthermore, the satellite is equipped with eight cold-gas thrusters, which are used during the execution of the procedure for the calibrating the gradiometer. The spacecraft has no moving parts and its shape is optimized for minimizing the effect of aerodynamic drag. An overview over the accommodation of the instruments is provided in Fig. 1 [Fehringer(2008)].

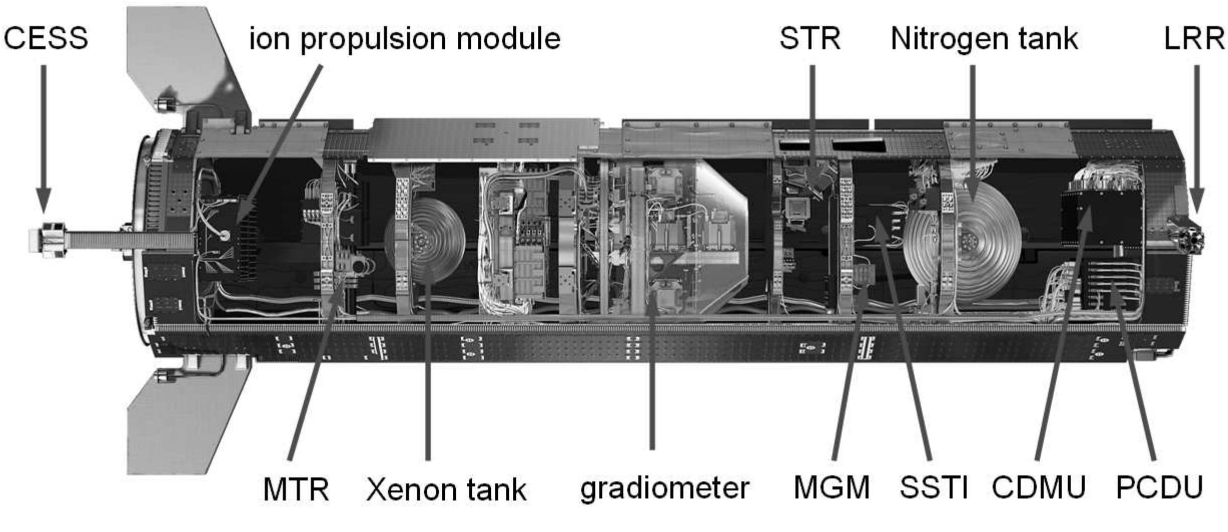

Figure 1: Top-down view on the GOCE satellite showing the accommodation of instruments. The acronyms in the figure stand for: star tracker (STR), coarse Earth-Sun sensor (CESS), magneto-torquers (MTR), magnetometers (MGM), satellite-to-satellite tracking instrument (SSTI), command and data management unit (CDMU), power conditioning and distribution unit (PCDU), and laser retro-reflector (LRR). The Xenon tank contains the fuel for the ion propulsion module while the Nitrogen tank contains the fuel for the cold-gas thrusters.

The most important instrument for achieving the mission objectives is the electrostatic gravity gradiometer, consisting of three pairs of ultra-sensitive accelerometers. The pairs are mounted at the ends of three orthogonal gradiometer arms, whereas the accelerometers forming one pair are separated by half a meter. Each accelerometer consists of a proof-mass levitated at the centre of the accelerometer cage. The levitation is achieved by applying control voltages to electrodes located at the inner walls of the accelerometer cage. The control voltages are representative for the experienced accelerations of the proof-mass relative to the cage.

The linear accelerations measured by the individual accelerometers do not directly yield gravity gradients. They reflect the combined effect of the linear acceleration acting on the satellite center-of-mass (COM) caused by e.g. winds, the angular velocity and angular acceleration of the satellite about its COM caused by e.g. the attitude control of the satellite, and the gravity gradient between the satellite COM and the centre of the individual accelerometer. Due to the geometric configuration of the six accelerometers, the gradiometer measures the linear and angular acceleration of the satellite directly. The angular velocity is obtained by combining the integrated angular acceleration measurements of the gradiometer with the differentiated attitude measurements of the star sensors. The computation of gravity gradients from the accelerometer and star sensor measurements is called gradiometer level 1b processing [SERCO/DATAMAT Consortium(2008)], which also includes the calibration of the gradiometer.

The accurate calibration of the gradiometer is a prerequisite for achieving the mission objectives. Since the gradiometer is designed to operate under micro-g conditions, the calibration, which comprises two parts, must be performed in-flight [Frommknecht et al.(2011)]. The first part is the determination of the quadratic factors of the transfer functions that relate the control voltages to the accelerations by means of a proof-mass shaking procedure. After the determination, the quadratic factors are zeroed by adjusting the position of the proof-masses relative to their cages. The second part is the determination of three so-called inverse calibration matrices (ICMs), one for each gradiometer arm. The ICMs account for scale factors of the transfer functions as well as for instrument imperfections such as non-orthogonal accelerometer axes and accelerometer misalignments. The ICMs are applied to the accelerometer data in the ground processing. In the following we refer to the determination of the ICMs when using the term calibration.

A dedicated calibration procedure called satellite shaking is executed every two months and lasts one day. During the execution of this procedure, the ion thrusters and cold-gas thrusters are used to generate pseudo-random linear and angular accelerations in the frequency band 50–100 mHz, in which we can assume that the gravity gradient signal is much smaller than the noise level of the gradiometer. In addition, pseudo-random angular accelerations are generated at 1.3 mHz, where both star sensor and gradiometer measurements have a large signal-to-noise ratio [Frommknecht et al.(2011)]. For convenience, we refer to data collected during a satellite shaking as shaking data. Data collected during a measurement cycle is referred to as nominal data. Table 1 gives an overview over the shakings performed since the beginning of nominal

Table 1: Availability of nominal and shaking data in the period from October 2009 to June 2011.

Satellite shaking	Satellite anomaly
08/10/2009	12/02/2010 – 01/03/2010
11/01/2010	08/07/2010 – 01/09/2010
04/03/2010	01/01/2011 – 19/01/2011
07/05/2010	
05/10/2010	
07/12/2010	
27/01/2011	
04/04/2011	
07/06/2011	

data acquisition on 31 October 2009, including satellite anomalies.

We distinguish between internal and external calibration methods. Internal calibration methods make use of data collected by the sensors on-board the GOCE satellite only, in particular the gradiometer and the star sensor measurements. They can be further subdivided into methods that rely on shaking data [Frommknecht et al.(2011)] and methods that work with shaking as well as nominal data [Kern et al.(2007)]. External calibration methods make use of additional data that are not measured by the sensors on-board GOCE. [Rispens and Bouman(2011)] as well as [Visser(2008)] use a global gravity field model and star sensor data for computing reference accelerations, which are used to estimate calibration parameters for the accelerometer data. [Bouman et al.(2009), Bouman et al.(2011)] use global gravity field models and terrestrial gravity data for estimating calibration parameters for gravity gradients. All of these external calibration methods make use of nominal data.

In order to assess the impact of the upgraded gradiometer level 1b processing and the calibration of the gradiometer, we validate the gravity gradients. This is a complex task since GOCE was designed to deliver the best ever set of gravity gradients. We use the gravity field model ITG-Grace2010s [Mayer-Gürr et al.(2011)], which is based on data of the Gravity Recovery and Climate Experiment (GRACE) mission [Tapley et al.(2004)], to compute reference gravity gradients along the GOCE orbit. The limitation of this approach is that GRACE measures the short wavelength signal of the gravity field less accurately than GOCE. Thus, reference gravity gradients validate only the long and middle wavelengths. Another way to assess impact is to compute the trace of the gravity gradient tensor. Here, we have no limitations with respect to the wavelengths. However, the trace is invariant against the attitude of the satellite and checks only the sum of diagonal components of the 3×3 gravity gradient tensor instead of checking all gravity gradients individually.

In addition to validating gravity gradients, we also validate the gravity field computed from the gravity gradients. Here, we compare against the gravity field models ITG-Grace2010s and EGM2008 [Pavlis et al.(2008)]. Both gravity fields have their pros and cons. As already mentioned, the ITG-Grace2010s can serve as a reference for the low and middle wavelength signal of the gravity field, but not for the short wavelength signal. EGM2008 is based on GRACE mission data, terrestrial gravity data, satellite altimetry derived gravity data, airborne gravity data, and marine gravity data. In comparison to gravity fields derived from GOCE gradiometer data, it can serve as a reference for the long and short wavelength signal. The middle wavelength signal of the EGM2008 appear to suffer from gaps in Africa, South-America and Antarctica in the terrestrial gravity data sets, which needs to be taken into account in the validation.

2 Reference frames

Throughout this report we make use of different coordinate reference frames. In this section, we provide an overview over these reference frames and clarify the transformations between them. Detailed information can be found in [European GOCE Gravity Consortium(2008)] and [Petit and Luzum(2010)]. The reference frames of interest are

- the gradiometer reference frame (GRF)
- the star sensor reference frame of star sensor x (SSRFx),
- the inertial reference frame (IRF),
- the Earth-fixed reference frame (EFRF), and
- the local north-oriented reference frame (LNOF).

All of these reference frames define orthogonal, right-handed systems.

The GRF is the instrument reference frame of the gradiometer. The attitude of the GOCE satellite is controlled such that the x, y and z axes of the GRF coincide with flight, cross-track and nadir direction, respectively, within a few degrees. The gradiometer arms are precisely aligned with the coordinate axes of the GRF. The origin of the GRF is precisely located in the centre of the gradiometer, i.e. the point where the gradiometer arms cross each other. The COM of the satellite is by construction very close to the origin of the GRF: $x_{\mathrm{COM}}^{(\mathrm{GRF})}$ within a few centimetres, $y_{\mathrm{COM}}^{(\mathrm{GRF})}$ and $z_{\mathrm{COM}}^{(\mathrm{GRF})}$ within a few millimetres (cf. the mass property file available on `http://earth.esa.int`).

Each of the three star sensors has its own instrument reference frame, i.e. the SSRF. The z-axis of the SSRF is the boresight of the star sensor while the x and y axes lie in the focal plane. The relative orientation of the SSRFs and the GRF is provided by so-called mounting matrices $\boldsymbol{R}^{\mathrm{SSRF}\to\mathrm{GRF}}$ which are provided in the AUX_EGG_DB product:

$$\boldsymbol{R}^{\mathrm{SSRF1}\to\mathrm{GRF}} = \begin{bmatrix} 0.99999195396400 & -0.00385545306786 & 0.00110792125081 \\ -0.00287527613216 & -0.49628568537300 & 0.86815450887500 \\ -0.00279728350732 & -0.86815070925200 & -0.49629277773300 \end{bmatrix} \tag{1}$$

$$\boldsymbol{R}^{\mathrm{SSRF2}\to\mathrm{GRF}} = \begin{bmatrix} 0.99986843913500 & 0.01572679351300 & -0.00397144656483 \\ 0.01614931208110 & -0.94226871687900 & 0.33446803272000 \\ 0.00151793982847 & -0.33448816594600 & -0.94239872808700 \end{bmatrix} \tag{2}$$

$$\boldsymbol{R}^{\mathrm{SSRF3}\to\mathrm{GRF}} = \begin{bmatrix} 0.01184624278020 & -0.76918392877300 & 0.63891763964500 \\ -0.49141129308600 & 0.55199930411200 & 0.67365548263700 \\ -0.87084706324300 & -0.32195162987100 & -0.37144655128900 \end{bmatrix} \tag{3}$$

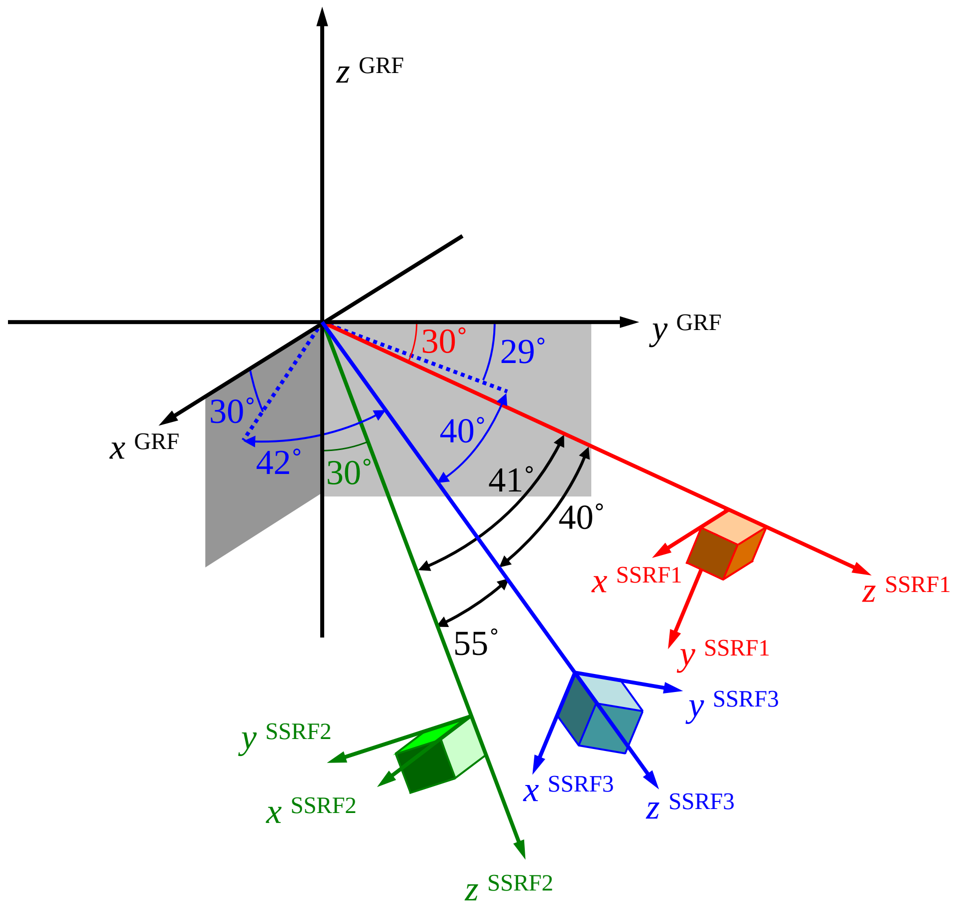

Figure 2: Relative orientation of the GRF and the SSRFs. Note that z^{SSRF1} and z^{SSRF2} lie in the y^{GRF}-z^{GRF}-plane and that x^{SSRF1} and x^{SSRF2} are parallel to x^{GRF}.

The columns of the mounting matrices contain unit vectors representing the coordinate axes of the SSRFs expressed in GRF coordinates. For example the y axis of SSRF1 is

$$\boldsymbol{y}_{\mathrm{SSRF1}}^{(\mathrm{GRF})} = \begin{bmatrix} -0.00385545306786 \\ -0.49628568537300 \\ -0.86815070925200 \end{bmatrix} \tag{4}$$

in the GRF. Fig. 2 indicates the pointing of the axes of the SSRFs with respect to the GRF. Note that the angle between two boresight directions is at least 40°.

The IRF is a celestial reference frame which is fixed in space. It defines the quasi-absolute orientation in space which is measured by the star sensors. The origin of the IRF is located in the geocentre, i.e. the centre of mass of the Earth. The x axis points into the direction of the vernal equinox while the z axis points towards the celestial pole.

The EFRF is a terrestrial reference frame which is fixed to the Earth's surface and, therefore, a rotating reference frame. The origin of the EFRF is located in the geocentre, i.e. the centre of mass of the Earth. The z axis is pointing towards the North Pole. The x and y axes lie in the equatorial plane, with the x axis intersecting the Greenwich Meridian.

The transformation between the IRF and EFRF is a rotation reflecting Earth's diurnal rotation as well as the precession, nutation and polar motion of the Celestial Intermediate Pole (CIP). The transformation parameters are provided by the IERS and contained in the SST_PRM_2 dataset of the SST_PSO_2 product in form of quaternions.

The LNOF is a local reference frame, which means that its origin is located in a point of interest and the pointing of its axes depends on that origin: The z axis points radially outwards, the y axis points westwards, and the x axis points northwards. The axes expressed in the EFRF read

$$\boldsymbol{x}_{\mathrm{LNOF}}^{(\mathrm{EFRF})} = \begin{bmatrix} \cos\lambda\cos\phi \\ \sin\lambda\cos\phi \\ \sin\phi \end{bmatrix}, \quad \boldsymbol{y}_{\mathrm{LNOF}}^{(\mathrm{EFRF})} = \begin{bmatrix} \sin\lambda \\ -\cos\lambda \\ 0 \end{bmatrix}, \quad \text{and} \quad \boldsymbol{z}_{\mathrm{LNOF}}^{(\mathrm{EFRF})} = \begin{bmatrix} -\cos\lambda\sin\phi \\ -\sin\lambda\sin\phi \\ \cos\phi \end{bmatrix} \tag{5}$$

where λ, ϕ and r are the spherical longitude, latitude and radius of the point of interest in the EFRF. The gravity potential field is usually expressed in dependence of λ, ϕ and r. When we compute functionals of the gravity field, such as gravity gradients, we do so in the LNOF and then rotate the results into the target reference frame. Fig. 3 provides an overview over the IRF, EFRF, LNOF and GRF.

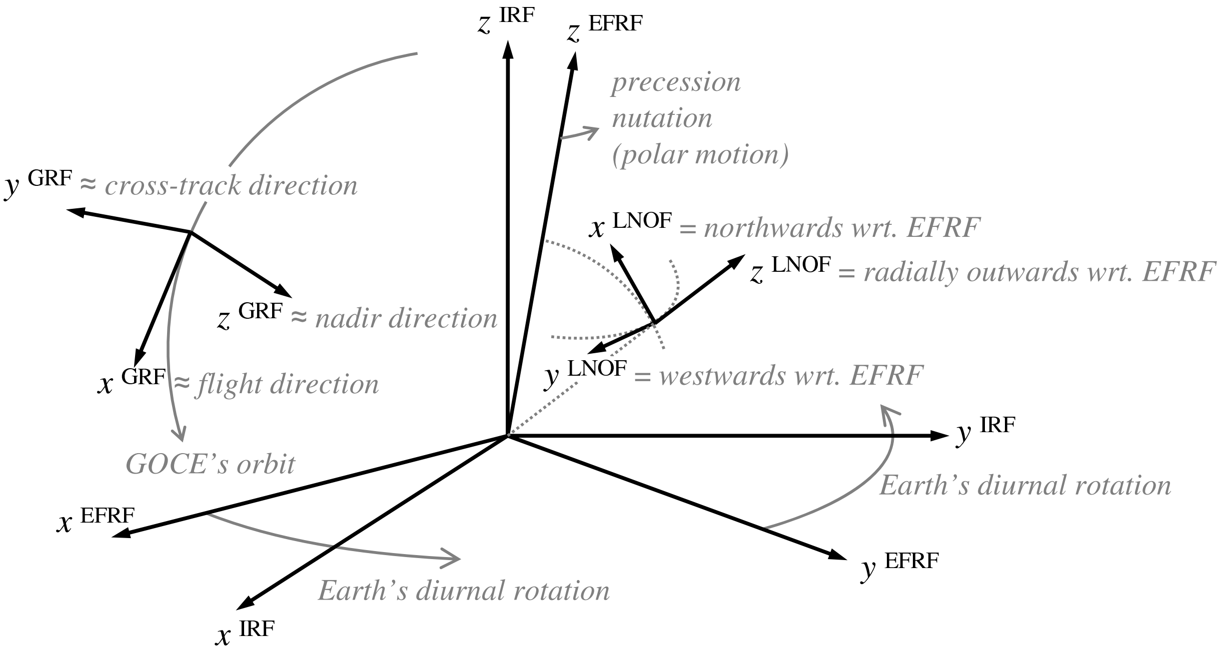

Figure 3: Overview over the IRF, EFRF, LNOF and GRF.

European Space Agency
Agence spatiale européenne

3 Gravity gradiometry

In this section we show how gravity gradients are determined from the accelerometer and star sensor measurements. First, we explain the principles assuming an ideal instrument. Then, we introduce the calibration of the gradiometer which is needed due to instrument imperfections. Finally, we discuss the impact of fact the accelerometers have two ultra-sensitive axes and one less sensitive axis.

3.1 Gravity gradiometry assuming an ideal gradiometer

Let us assume that the accelerometer axes are aligned with the GRF and that the quadratic factors are successfully zeroed and the scale factors are perfectly known and applied in the conversion of electrode control voltages to accelerations. Furthermore, let us assume that accelerations due to other satellite masses (self-gravity) and the coupling of accelerometer proof-masses to the magnetic field can be neglected. Then, each of the six accelerometers measures accelerations

$$\boldsymbol{a}_i = -(\boldsymbol{V} - \boldsymbol{\Omega}^2 - \dot{\boldsymbol{\Omega}})\boldsymbol{r}_i + \boldsymbol{d}, \tag{6}$$

where i is the identifier of the accelerometer (cf. Fig. 4), $\boldsymbol{r}_i$ is the vector from the satellite's centre of mass (COM) to the centre of the i-th accelerometer, $\boldsymbol{V}$ contains the gravity gradients, $\boldsymbol{\Omega}^2\boldsymbol{r}_i$ are centrifugal accelerations due to the rotation of the satellite about its COM, $\dot{\boldsymbol{\Omega}}\boldsymbol{r}_i$ are linear accelerations due to satellite angular accelerations about its COM, and $\boldsymbol{d}$ are linear accelerations of the satellite's COM [Cesare(2008)]. The matrices $\boldsymbol{V}$, $\boldsymbol{\Omega}$, $\dot{\boldsymbol{\Omega}}$ and $\boldsymbol{\Omega}^2$ are defined as follows:

$$\boldsymbol{V} \equiv \begin{bmatrix} V_{xx} & V_{xy} & V_{xz} \\ V_{xy} & V_{yy} & V_{yz} \\ V_{xz} & V_{yz} & V_{zz} \end{bmatrix} \tag{7}$$

$$\boldsymbol{\Omega} \equiv \begin{bmatrix} 0 & -\omega_z & \omega_y \\ \omega_z & 0 & -\omega_x \\ -\omega_y & \omega_x & 0 \end{bmatrix} \tag{8}$$

$$\dot{\boldsymbol{\Omega}} \equiv \begin{bmatrix} 0 & -\dot{\omega}_z & \dot{\omega}_y \\ \dot{\omega}_z & 0 & -\dot{\omega}_x \\ -\dot{\omega}_y & \dot{\omega}_x & 0 \end{bmatrix} \tag{9}$$

$$\boldsymbol{\Omega}^2 \equiv \begin{bmatrix} -\omega_y^2 - \omega_z^2 & \omega_x\omega_y & \omega_x\omega_z \\ \omega_x\omega_y & -\omega_x^2 - \omega_z^2 & \omega_y\omega_z \\ \omega_x\omega_z & \omega_y\omega_z & -\omega_x^2 - \omega_y^2 \end{bmatrix} \tag{10}$$

The accelerations $\boldsymbol{a}_i$ are transformed into common mode (CM) accelerations

$$\boldsymbol{a}_{c,ij} = \frac{1}{2}(\boldsymbol{a}_i + \boldsymbol{a}_j) \tag{11}$$

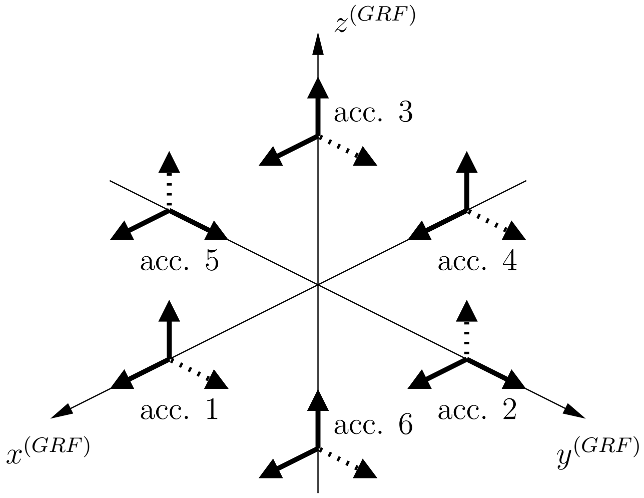

Figure 4: Arrangement of the six accelerometers in the gradiometer reference frame (GRF). Thick lines indicate the ultra-sensitive axes of the accelerometers. Dotted lines indicate the less-sensitive axis of the accelerometers.

and differential mode (DM) accelerations

$$\boldsymbol{a}_{d,ij} = \frac{1}{2}(\boldsymbol{a}_i - \boldsymbol{a}_j) \tag{12}$$

for each accelerometer pair $ij = 14, 25, 36$. Let us replace vector $\boldsymbol{r}_i$ by

$$\boldsymbol{r}_i = \boldsymbol{p}_i - \boldsymbol{c}, \tag{13}$$

where $\boldsymbol{p}_i$ is the vector from the origin of the GRF to the centre of the i-th accelerometer and $\boldsymbol{c}$ is the vector from the origin of the GRF to satellite's COM. Then, inserting Eq. (6) into Eqs. (11) and (12) gives

$$\boldsymbol{a}_{c,ij} = -\frac{1}{2}(\boldsymbol{V} - \boldsymbol{\Omega}^2 - \dot{\boldsymbol{\Omega}})(\boldsymbol{p}_i + \boldsymbol{p}_j) + (\boldsymbol{V} - \boldsymbol{\Omega}^2 - \dot{\boldsymbol{\Omega}})\boldsymbol{c} + \boldsymbol{d} \tag{14}$$

and

$$\boldsymbol{a}_{d,ij} = -\frac{1}{2}(\boldsymbol{V} - \boldsymbol{\Omega}^2 - \dot{\boldsymbol{\Omega}})(\boldsymbol{p}_i - \boldsymbol{p}_j). \tag{15}$$

Let us assume that the accelerometers occupy their nominal position. Then, the following holds:

$$\boldsymbol{p}_1 + \boldsymbol{p}_4 = \begin{bmatrix} 0 \\ 0 \\ 0 \end{bmatrix}, \boldsymbol{p}_2 + \boldsymbol{p}_5 = \begin{bmatrix} 0 \\ 0 \\ 0 \end{bmatrix}, \boldsymbol{p}_3 + \boldsymbol{p}_6 = \begin{bmatrix} 0 \\ 0 \\ 0 \end{bmatrix}, \tag{16}$$

$$\boldsymbol{p}_1 - \boldsymbol{p}_4 = \begin{bmatrix} L_x \\ 0 \\ 0 \end{bmatrix}, \boldsymbol{p}_2 - \boldsymbol{p}_5 = \begin{bmatrix} 0 \\ L_y \\ 0 \end{bmatrix}, \boldsymbol{p}_3 - \boldsymbol{p}_6 = \begin{bmatrix} 0 \\ 0 \\ L_z \end{bmatrix} \tag{17}$$

The gradiometer arm lengths $L_x = 0.5140135$ m, $L_y = 0.4998900$ m and $L_z = 0.5002010$ m are given in the AUX_EGG_DB product. We can simplify Eq. (14) to

$$\boldsymbol{a}_{c,ij} = (\boldsymbol{V} - \boldsymbol{\Omega}^2 - \dot{\boldsymbol{\Omega}})\boldsymbol{c} + \boldsymbol{d} \approx \boldsymbol{d} \tag{18}$$

because the satellite COM is very close to the origin of the GRF, i.e. $\boldsymbol{c}$ is in the order of a few centimetres [Bigazzi and Frommknecht(2010)], and the term $\boldsymbol{V} - \boldsymbol{\Omega}^2 - \dot{\boldsymbol{\Omega}}$ is about 1000 times smaller than the linear acceleration of the satellite COM $\boldsymbol{d}$, which we know from the analysis of GOCE mission data. Thus, we can determine the linear acceleration of the satellite COM by building CM accelerations.

We can derive the angular accelerations $\dot{\boldsymbol{\Omega}}$ of the satellite about its COM in the following way. From Eqs. (15) and (17) we can deduce

$$\boldsymbol{A}_d = -\frac{1}{2}(\boldsymbol{V} - \boldsymbol{\Omega}^2 - \dot{\boldsymbol{\Omega}})\boldsymbol{L} \tag{19}$$

where

$$\boldsymbol{A}_d = \begin{bmatrix} \boldsymbol{a}_{d,14} & \boldsymbol{a}_{d,25} & \boldsymbol{a}_{d,36} \end{bmatrix} \tag{20}$$

and

$$\boldsymbol{L} = \begin{bmatrix} L_x & 0 & 0 \\ 0 & L_y & 0 \\ 0 & 0 & L_z \end{bmatrix}. \tag{21}$$

Since $\boldsymbol{V}$ and $\boldsymbol{\Omega}^2$ are symmetric matrices, i.e. $\boldsymbol{V}^T = \boldsymbol{V}$ and $(\boldsymbol{\Omega}^2)^T = \boldsymbol{\Omega}^2$, and $\dot{\boldsymbol{\Omega}}$ is a skew-symmetric matrix, i.e. $\dot{\boldsymbol{\Omega}}^T = -\dot{\boldsymbol{\Omega}}$, we find

$$\boldsymbol{A}_d\boldsymbol{L}^{-1} - (\boldsymbol{A}_d\boldsymbol{L}^{-1})^T = -\frac{1}{2}(\boldsymbol{V} - \boldsymbol{\Omega}^2 - \dot{\boldsymbol{\Omega}}) + \frac{1}{2}(\boldsymbol{V} - \boldsymbol{\Omega}^2 - \dot{\boldsymbol{\Omega}})^T = \dot{\boldsymbol{\Omega}}. \tag{22}$$

From Eq. (22) we can extract

$$\dot{\omega}_x = \frac{a_{d,25,z}}{L_y} - \frac{a_{d,36,y}}{L_z}, \tag{23}$$

$$\dot{\omega}_y = \frac{a_{d,36,x}}{L_z} - \frac{a_{d,14,z}}{L_x} \tag{24}$$

and

$$\dot{\omega}_z = \frac{a_{d,14,y}}{L_x} - \frac{a_{d,25,x}}{L_y}. \tag{25}$$

Thus, the gradiometer measures the angular acceleration of the satellite about its COM.

For deriving the gravity gradients from the DM accelerations, we need not only the angular acceleration components $\dot{\omega}_x$, $\dot{\omega}_y$ and $\dot{\omega}_z$ but also the angular velocity components ω_x, ω_y and ω_z. The latter are determine from star sensor and gradiometer measurements in the following way. The star sensor attitude, given in form of a rotation matrix $\boldsymbol{R}$ relating the inertial reference frame (IRF) to the GRF, is differentiated using Poisson's equations

$$\dot{\boldsymbol{R}} = -\boldsymbol{\Omega}\boldsymbol{R} \tag{26}$$

to obtain the star sensor angular velocity

$$\boldsymbol{\Omega} = -\dot{\boldsymbol{R}}\boldsymbol{R}^T. \tag{27}$$

In addition, the gradiometer angular acceleration is integrated to obtain the angular acceleration

$$\boldsymbol{\omega} = \int \dot{\boldsymbol{\omega}}\, dt + \boldsymbol{\omega}_0 \tag{28}$$

where

$$\boldsymbol{\omega} = \begin{bmatrix} \omega_x & \omega_y & \omega_z \end{bmatrix}^T, \tag{29}$$

$$\dot{\boldsymbol{\omega}} = \begin{bmatrix} \dot{\omega}_x & \dot{\omega}_y & \dot{\omega}_z \end{bmatrix}^T \tag{30}$$

and $\boldsymbol{\omega}_0$ is the integration constant. Due to the noise characteristics of the star sensors and the gradiometer and the noise propagation due to the differentiation and integration, the angular velocity derived from the star sensor is more accurate in the low frequencies while the angular velocity of the gradiometer is more accurate in the high frequencies. Therefore, the final angular velocity is obtained by a combination of the star sensor and gradiometer angular velocities, taking the noise characteristics into account. In a simplified way, we can regard this combination as adding the low-pass filtered angular velocity of the star sensor to the complementary high-pass filtered angular velocity of the gradiometer:

$$\boldsymbol{\omega} = \text{low-pass}(\boldsymbol{\omega}^{(\text{star sensor})}) + \text{high-pass}(\boldsymbol{\omega}^{(\text{gradiometer})} - \boldsymbol{\omega}_0) \tag{31}$$

Note that the highpass filter should be designed to eliminate the integration constant $\boldsymbol{\omega}_0$. Finally, we can compute the gravity gradients from

$$\boldsymbol{A}_d\boldsymbol{L}^{-1} + (\boldsymbol{A}_d\boldsymbol{L}^{-1})^T = -\boldsymbol{V} + \boldsymbol{\Omega}^2. \tag{32}$$

This leads to the diagonal gravity gradient components

$$V_{xx} = -2\frac{a_{d,14,x}}{L_x} - \omega_y^2 - \omega_z^2, \tag{33}$$

$$V_{yy} = -2\frac{a_{d,25,y}}{L_y} - \omega_x^2 - \omega_z^2 \tag{34}$$

and

$$V_{zz} = -2\frac{a_{d,36,z}}{L_z} - \omega_x^2 - \omega_y^2, \tag{35}$$

and the off-diagonal gravity gradient components

$$V_{xy} = -\frac{a_{d,25,x}}{L_y} - \frac{a_{d,14,y}}{L_x} + \omega_x\omega_y, \tag{36}$$

$$V_{xz} = -\frac{a_{d,14,z}}{L_x} - \frac{a_{d,36,x}}{L_z} + \omega_x\omega_z \tag{37}$$

and

$$V_{yz} = -\frac{a_{d,36,y}}{L_z} - \frac{a_{d,25,z}}{L_y} + \omega_y\omega_z. \tag{38}$$

3.2 Model for instrument imperfections

Even though the manufacturing was following strict requirements, the gradiometer is subject to small instrument imperfections such as [Cesare(2008)]:

- Accelerometers do not exactly occupy their nominal positions
- Accelerometer axes are not fully aligned with the GRF
- Accelerometer axes are not perfectly orthogonal to each other
- Accelerations are obtained with a scale factor due to the uncertain knowledge of the electrostatic gains and the read-out gain for the conversion of the electrode control voltages to accelerations
- Imperfections could slightly change over time

In order to account for these imperfections, the method presented in this paper uses the calibration model

$$\boldsymbol{a}_i = \boldsymbol{M}_i \tilde{\boldsymbol{a}}_i \tag{39}$$

where i is the identifier of the accelerometer, $\tilde{\boldsymbol{a}}_i$ are measured accelerations, $\boldsymbol{a}_i$ are calibrated accelerations and $\boldsymbol{M}_i$ is the calibration matrix. The calibration matrix

$$\boldsymbol{M}_i = \begin{bmatrix} s_{i,x} & \alpha_i + \zeta_i & \beta_i - \epsilon_i \\ \alpha_i - \zeta_i & s_{i,y} & \gamma_i + \delta_i \\ \beta_i + \epsilon_i & \gamma_i - \delta_i & s_{i,z} \end{bmatrix} \tag{40}$$

composes of scale factors $s_{i,x}$, $s_{i,y}$ and $s_{i,z}$, shear parameters α_i, β_i and γ_i, and rotation parameters δ_i, ϵ_i and ζ_i assuming small shear and rotation angles. We can also formulate the calibration model in terms of CM and DM accelerations.

$$\begin{bmatrix} \boldsymbol{a}_{c,ij} \\ \boldsymbol{a}_{d,ij} \end{bmatrix} = \boldsymbol{M}_{ij} \begin{bmatrix} \tilde{\boldsymbol{a}}_{c,ij} \\ \tilde{\boldsymbol{a}}_{d,ij} \end{bmatrix} \tag{41}$$

Herein, $\boldsymbol{a}_{c,ij}$ and $\boldsymbol{a}_{d,ij}$ are calibrated CM and DM accelerations, respectively, $\tilde{\boldsymbol{a}}_{c,ij}$ and $\tilde{\boldsymbol{a}}_{d,ij}$ are their measured counterparts, and $\boldsymbol{M}_{ij}$ is the ICM for the gradiometer arm ij. The latter is related to the calibration matrices $\boldsymbol{M}_i$ and $\boldsymbol{M}_j$ by

$$\boldsymbol{M}_{ij} = \frac{1}{2} \begin{bmatrix} \boldsymbol{M}_i + \boldsymbol{M}_j & \boldsymbol{M}_i - \boldsymbol{M}_j \\ \boldsymbol{M}_i - \boldsymbol{M}_j & \boldsymbol{M}_i + \boldsymbol{M}_j \end{bmatrix} = \begin{bmatrix} \boldsymbol{C}_{ij} & \boldsymbol{D}_{ij} \\ \boldsymbol{D}_{ij} & \boldsymbol{C}_{ij} \end{bmatrix}, \tag{42}$$

where

$$\boldsymbol{C}_{ij} = \begin{bmatrix} \bar{s}_{ij,x} & \bar{\alpha}_{ij} + \bar{\zeta}_{ij} & \bar{\beta}_{ij} - \bar{\epsilon}_{ij} \\ \bar{\alpha}_{ij} - \bar{\zeta}_{ij} & \bar{s}_{ij,y} & \bar{\gamma}_{ij} + \bar{\delta}_{ij} \\ \bar{\beta}_{ij} + \bar{\epsilon}_{ij} & \bar{\gamma}_{ij} - \bar{\delta}_{ij} & \bar{s}_{ij,z} \end{bmatrix} \tag{43}$$

contains common scale factors $\bar{s}_{ij,x}$, $\bar{s}_{ij,y}$ and $\bar{s}_{ij,z}$, common shear parameters $\bar{\alpha}_{ij}$, $\bar{\beta}_{ij}$ and $\bar{\gamma}_{ij}$, and common rotation parameters $\bar{\delta}_{ij}$, $\bar{\epsilon}_{ij}$ and $\bar{\zeta}_{ij}$, and

$$\boldsymbol{D}_{ij} = \begin{bmatrix} \Delta s_{ij,x} & \Delta\alpha_{ij} + \Delta\zeta_{ij} & \Delta\beta_{ij} - \Delta\epsilon_{ij} \\ \Delta\alpha_{ij} - \Delta\zeta_{ij} & \Delta s_{ij,y} & \Delta\gamma_{ij} + \Delta\delta_{ij} \\ \Delta\beta_{ij} + \Delta\epsilon_{ij} & \Delta\gamma_{ij} - \Delta\delta_{ij} & \Delta s_{ij,z} \end{bmatrix} \tag{44}$$

contains differential scale factors $\Delta s_{ij,x}$, $\Delta s_{ij,y}$ and $\Delta s_{ij,z}$, differential shear parameters $\Delta\alpha_{ij}$, $\Delta\beta_{ij}$ and $\Delta\gamma_{ij}$, and differential rotation parameters $\Delta\delta_{ij}$, $\Delta\epsilon_{ij}$ and $\Delta\zeta_{ij}$.

3.3 Impact of less sensitive accelerometer axes on gravity gradients

Each accelerometer has two ultra-sensitive axes and one less sensitive axis, which is less accurate by a factor of 100. Due to the way in which the less sensitive axes are arranged (cf. Fig. 4), the gravity gradients V_{xx}, V_{yy}, V_{zz} and V_{xz} are very accurate while V_{xy} and V_{yz} suffer from the low accuracy of the less sensitive axes. This can be clearly seen in Fig. 5 where we compare GOCE gravity gradients to gravity gradients computed on the basis of the ITG-Grace2010s gravity field model along the GOCE orbit.

The main cause for the larger noise in the gravity gradients V_{xy} and V_{yz} is most likely the larger noise in the DM accelerations $a_{d,14,y}$, $a_{d,36,y}$ and $a_{d,25,z}$, which are the measurements of less sensitive axes. This assumption is supported by the decomposition of the gravity gradients into terms containing DM accelerations and terms containing centrifugal accelerations according to Eqs. (33)–(38). For example, V_{xx} composes of the term $-2\frac{a_{d,14,x}}{L_x}$ and the term $-\omega_y^2 - \omega_z^2$. Fig. 5 shows that the contribution of the terms containing centrifugal accelerations to V_{xy} and V_{yz} is negligible for frequencies 10–100 mHz.

The fact that V_{xy} and V_{yz} are much less accurate than the other gravity gradients needs to be considered when performing reference frame transformations. The transformation of the gravity gradients from the GRF to another reference frame, e.g. the EFRF, is defined by the rotation of the gravity gradient tensor

$$\boldsymbol{V}^{(\mathrm{EFRF})} = \boldsymbol{R}^{\mathrm{GRF}\rightarrow\mathrm{EFRF}} \boldsymbol{V}^{(\mathrm{GRF})} (\boldsymbol{R}^{\mathrm{GRF}\rightarrow\mathrm{EFRF}})^T \tag{45}$$

where $\boldsymbol{V}^{(\mathrm{GRF})}$ and $\boldsymbol{V}^{(\mathrm{EFRF})}$ are the gravity gradient tensor in the GRF and EFRF, respectively, and $\boldsymbol{R}^{\mathrm{GRF}\rightarrow\mathrm{EFRF}}$ is the rotation matrix from the GRF to the EFRF. Eq. (45) shows that the larger noise in V_{xy} and V_{yz} propagates to all gravity gradients due to the rotation of the gravity gradient tensor. For this reason, we compare gravity gradients in this report always in the GRF. Note that in case of spatial plots, we need to separate ascending and descending orbital arcs due to the different orientation of the GRF.

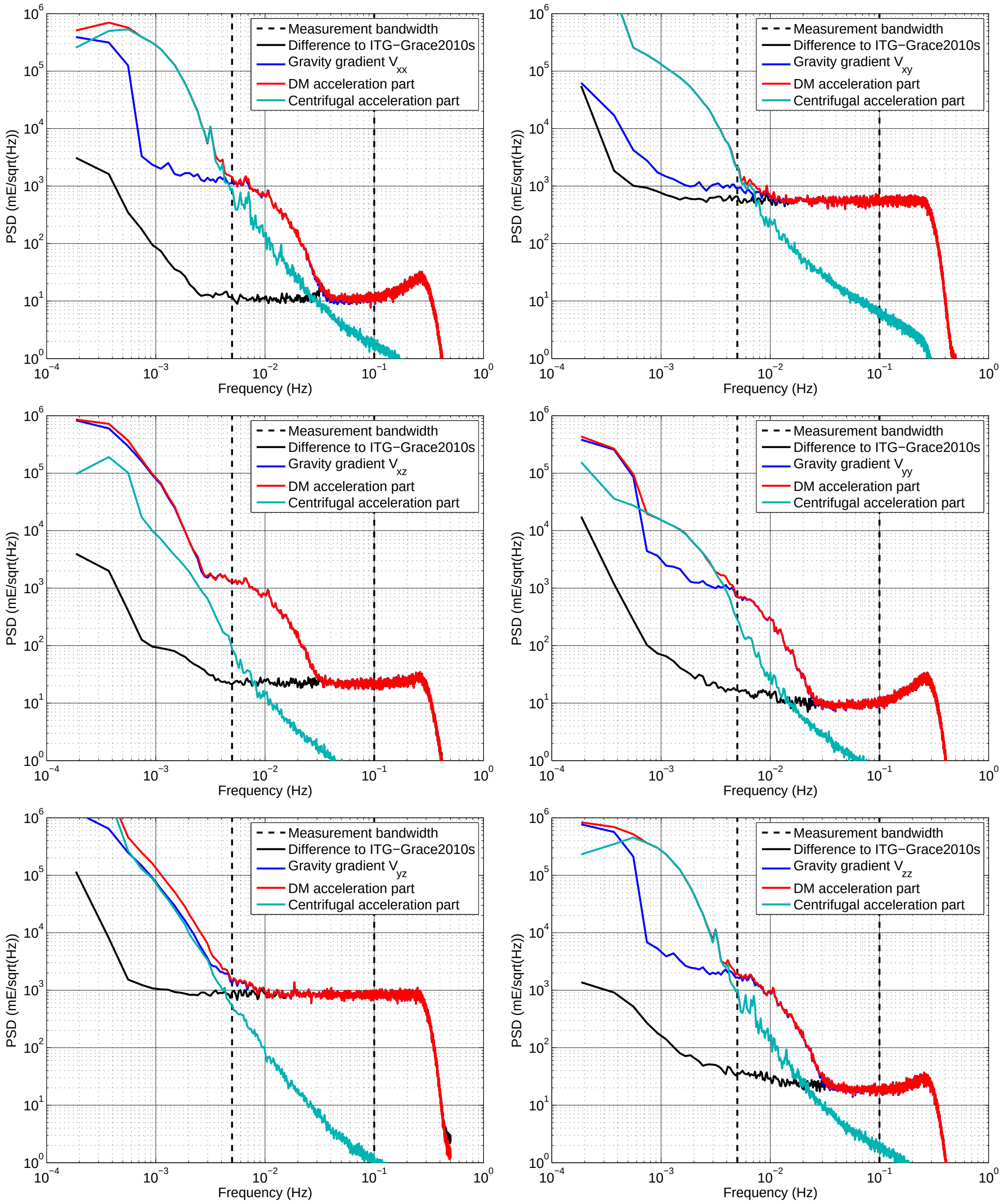

Figure 5: Comparison of GOCE gravity gradients to gravity gradients computed from the ITG-Grace2010s gravity field model. The gravity gradients have been de-composed into terms containing DM accelerations and terms containing centrifugal accelerations.

4 Combining data of star sensors

The GOCE satellite is equipped with three star sensors pointing in different directions [Drinkwater et al.(2007)]. The data of at least two star sensors are down-linked at a time. The star sensors provide the inertial attitude of the satellite, from which we can derive by numerical differentiation the rotational part of the satellite motion, represented by the angular velocity $\boldsymbol{\omega}$ and the angular acceleration $\dot{\boldsymbol{\omega}}$. The latter can also be computed from accelerometer data and, therefore, we can use star sensor angular accelerations for the calibration of the gradiometer.

A property of the star sensors is that the angular velocity about the boresight, which is perpendicular to the star sensor's focal plane and points into the direction of the field-of-view [Liebe(2002)], is less accurately measured than angular velocities about axes that are perpendicular to the boresight [Jørgensen(2003)]. The star sensor reference frame (SSRF) is defined as follows. The z-axis is the boresight while the x- and y-axis are lying in the focal plane of the star sensor, perpendicular to the boresight and forming a right-handed system. Therefore, when expressing the angular velocity in the SSRF, as indicated by the superscript, $\omega_z^{(SSRF)}$ is less accurate than $\omega_x^{(SSRF)}$ and $\omega_y^{(SSRF)}$. In order to relate the star sensor data to accelerometer data, we transform the angular velocity from the SSRF to the GRF. In this transformation, the errors of the less accurate $\omega_z^{(SSRF)}$ propagate to errors in $\omega_x^{(GRF)}$, $\omega_y^{(GRF)}$ and $\omega_z^{(GRF)}$ in the GRF depending on the orientation of the star sensor with respect to the gradiometer. The propagation of errors in the reference frame transformation is demonstrated in Fig. 6.

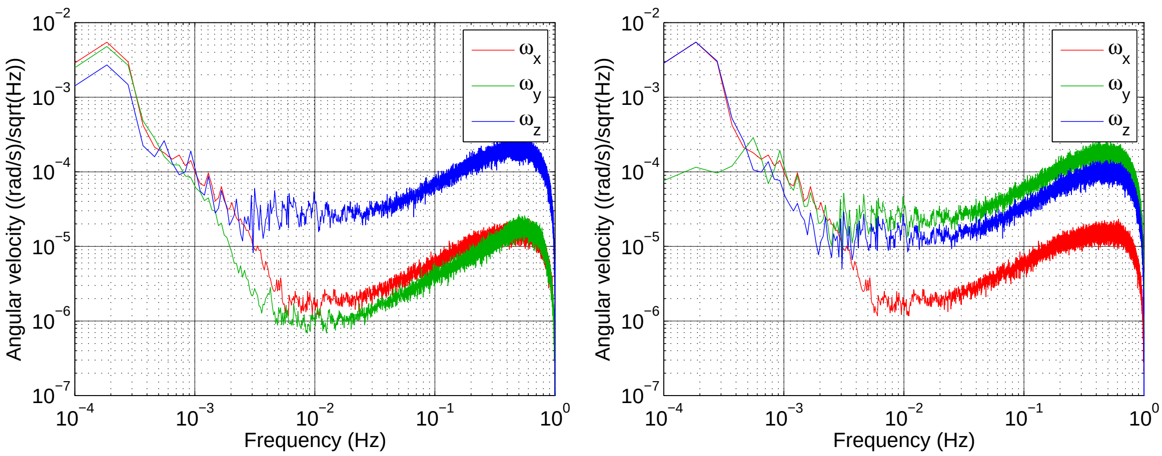

Figure 6: Square-roots of the PSDs of angular velocities measured by star sensor one in the $SSRF_1$ (top panel) and in the GRF (bottom panel). The square-roots of the PSDs largely reflect measurement noise above 10 mHz. The noise in the less accurate ω_z in the $SSRF_1$ propagates to ω_y and ω_z in the GRF because the transformation from the $SSRF_1$ to the GRF is mainly a rotation about the x-axis of the $SSRF_1$. We used data of 23 Nov 2009 for this plot.

The angle between the boresights of two star sensors is at minimum 40° [Bigazzi and Frommknecht(2010)]. Thus, the less accurately measured component of the angular velocity of one star sensor is measured with a better accuracy by another. For this reason, the combination of the angular velocities from different star sensors can prevent the propagation of the less accurate component due to the reference frame transformation.

We consider two methods of combining star sensor data, which are both performed by means of a least-squares adjustment. The first method is based on the combination of attitude quaternions. It is used for the attitude determination of the GRACE satellites, which have each two star sensors onboard [Romans(2003)]. The second method is based on the combination of angular velocities. It should be mentioned that the angular velocities calculated by one or the other method are of equal quality. Thus, if only angular velocities are needed, both methods may be used. In order to maximize the comparability of our results to those of ESA's baseline method for estimating gradiometer calibration parameters, we use the same method for combining star sensor data, namely the method that combines angular velocities. However, if also the attitude is needed, which is the case for level 1b processing, we use the method that combines the star sensor data on attitude level.

4.1 Combination of attitude quaternions

The following presents the mathematical background of the attitude quaternion combination provided by [Romans(2003)] in the notation we use for the GOCE mission. Let $\boldsymbol{q}^{\text{measured IRF}\rightarrow\text{SSRFx}}$ be a quaternion describing the rotation from IRF to SSRFx as measured by STRx. It can be related to the true rotation from IRF to SSRFx by

$$\boldsymbol{q}^{\text{measured IRF}\rightarrow\text{SSRFx}} = \boldsymbol{q}^{\text{true IRF}\rightarrow\text{SSRFx}}\boldsymbol{q}^{\text{noise STRx}} \tag{46}$$

In words, we model the measured quaternion as the true quaternion rotated by

$$\boldsymbol{q}^{\text{noise STRx}} = \begin{bmatrix} 1 \\ 0.5e_1^{\text{STRx}} \\ 0.5e_2^{\text{STRx}} \\ 0.5e_3^{\text{STRx}} \end{bmatrix} \tag{47}$$

where e_1^{STRx}, e_2^{STRx} and e_3^{STRx} represent small angles. The factor 0.5 is introduced such that $\boldsymbol{q}^{\text{noise STRx}}$ is equivalent to the rotation matrix

$$\boldsymbol{R}^{\text{noise STRx}} = \begin{bmatrix} 1 & e_3^{\text{STRx}} & -e_2^{\text{STRx}} \\ -e_3^{\text{STRx}} & 1 & e_1^{\text{STRx}} \\ e_2^{\text{STRx}} & -e_1^{\text{STRx}} & 1 \end{bmatrix}. \tag{48}$$

Furthermore, let $\boldsymbol{q}^{\text{SSRFx}\rightarrow\text{GRF}}$ be a quaternion describing the rotation from SSRFx to GRF, i.e. being the equivalent to the mounting matrix $\boldsymbol{R}^{\text{SSRFx}\rightarrow\text{GRF}}$ (we assume that the mounting information is correct). Now, the following condition holds:

$$\boldsymbol{q}^{\mathrm{GRF}\to\mathrm{SSRFx}}\boldsymbol{q}^{\mathrm{true\,SSRFx}\to\mathrm{IRF}}\boldsymbol{q}^{\mathrm{true\,IRF}\to\mathrm{SSRFy}}\boldsymbol{q}^{\mathrm{SSRFy}\to\mathrm{GRF}} = \begin{bmatrix}1\\0\\0\\0\end{bmatrix} \tag{49}$$

For the measured quaternions of two star sensors, however, we observe a small relative error

$$\boldsymbol{q}^{\mathrm{GRF}\to\mathrm{SSRFx}}\boldsymbol{q}^{\mathrm{measured\,SSRFx}\to\mathrm{IRF}}\boldsymbol{q}^{\mathrm{measured\,IRF}\to\mathrm{SSRFy}}\boldsymbol{q}^{\mathrm{SSRFy}\to\mathrm{GRF}} = \begin{bmatrix}1\\0.5d_1^{\mathrm{STRxy}}\\0.5d_2^{\mathrm{STRxy}}\\0.5d_3^{\mathrm{STRxy}}\end{bmatrix}, \tag{50}$$

which is related to the star sensors' noise by

$$\begin{bmatrix}d_1^{\mathrm{STRxy}}\\d_2^{\mathrm{STRxy}}\\d_3^{\mathrm{STRxy}}\end{bmatrix} = \boldsymbol{R}^{\mathrm{SSRFy}\to\mathrm{GRF}}\begin{bmatrix}e_1^{\mathrm{STRy}}\\e_2^{\mathrm{STRy}}\\e_3^{\mathrm{STRy}}\end{bmatrix} - \boldsymbol{R}^{\mathrm{SSRFx}\to\mathrm{GRF}}\begin{bmatrix}e_1^{\mathrm{STRx}}\\e_2^{\mathrm{STRx}}\\e_3^{\mathrm{STRx}}\end{bmatrix} \tag{51}$$

We obtain the optimal quaternion by minimizing the weighted square-sum

$$S = \sum_x (\boldsymbol{e}^{\mathrm{STRx}})^T \boldsymbol{P}^{\mathrm{STRx}}\boldsymbol{e}^{\mathrm{STRx}} \tag{52}$$

where

$$\boldsymbol{e}^{\mathrm{STRx}} = \begin{bmatrix}e_1^{\mathrm{STRx}}\\e_2^{\mathrm{STRx}}\\e_3^{\mathrm{STRx}}\end{bmatrix} \tag{53}$$

contains the star sensor noise and

$$\boldsymbol{P}^{\mathrm{STRx}} = \begin{bmatrix}1 & 0 & 0\\0 & 1 & 0\\0 & 0 & 0.01\end{bmatrix} \tag{54}$$

is the weighting matrix. The element being equal to 0.01 reflects that the attitude about the boresight is 10 times less accurate than the attitude about the axes in the focal plane of the star sensor. For convenience, we express S by

$$S = \sum_x (\tilde{\boldsymbol{e}}^{\mathrm{STRx}})^T \tilde{\boldsymbol{P}}^{\mathrm{STRx}}\tilde{\boldsymbol{e}}^{\mathrm{STRx}} \tag{55}$$

where

$$\tilde{\boldsymbol{e}}^{\mathrm{STRx}} = \boldsymbol{R}^{\mathrm{SSRFx}\to\mathrm{GRF}}\boldsymbol{e}^{\mathrm{STRx}} \tag{56}$$

is the star sensor noise transformed to the GRF and

$$\tilde{\boldsymbol{P}}^{\mathrm{STRx}} = \boldsymbol{R}^{\mathrm{SSRFx}\to\mathrm{GRF}}\boldsymbol{P}^{\mathrm{STRx}}(\boldsymbol{R}^{\mathrm{SSRFx}\to\mathrm{GRF}})^T \tag{57}$$

is obtained by variance propagation. By rearranging Eq. (51) to

$$\tilde{\boldsymbol{e}}^{\mathrm{STRy}} = \boldsymbol{d}^{\mathrm{STRxy}} + \tilde{\boldsymbol{e}}^{\mathrm{STRx}}, \tag{58}$$

where

$$\boldsymbol{d}^{\mathrm{STRxy}} = \begin{bmatrix} d_1^{\mathrm{STRxy}} \\ d_2^{\mathrm{STRxy}} \\ d_3^{\mathrm{STRxy}} \end{bmatrix}, \tag{59}$$

we find that all $\tilde{\boldsymbol{e}}^{\mathrm{STRy}}$ depend one single $\tilde{\boldsymbol{e}}^{\mathrm{STRx}}$ because the $\boldsymbol{d}^{\mathrm{STRxy}}$ are defined by the measurements. Therefore, we can choose $\tilde{\boldsymbol{e}}^{\mathrm{STRx}}$ as the parameters of this least-squares problem. Next, we express S in dependence of the parameters $\tilde{\boldsymbol{e}}^{\mathrm{STRx}}$:

$$\begin{aligned} S &= \sum_x (\tilde{\boldsymbol{e}}^{\mathrm{STRx}})^T \tilde{\boldsymbol{P}}^{\mathrm{STRx}} \tilde{\boldsymbol{e}}^{\mathrm{STRx}} && (60) \\ &= (\tilde{\boldsymbol{e}}^{\mathrm{STRx}})^T \tilde{\boldsymbol{P}}^{\mathrm{STRx}} \tilde{\boldsymbol{e}}^{\mathrm{STRx}} + \sum_{y \neq x} (\tilde{\boldsymbol{e}}^{\mathrm{STRy}})^T \tilde{\boldsymbol{P}}^{\mathrm{STRy}} \tilde{\boldsymbol{e}}^{\mathrm{STRy}} && (61) \\ &= (\tilde{\boldsymbol{e}}^{\mathrm{STRx}})^T \tilde{\boldsymbol{P}}^{\mathrm{STRx}} \tilde{\boldsymbol{e}}^{\mathrm{STRx}} + \sum_{y \neq x} (\boldsymbol{d}^{\mathrm{STRxy}} + \tilde{\boldsymbol{e}}^{\mathrm{STRx}})^T \tilde{\boldsymbol{P}}^{\mathrm{STRy}} (\boldsymbol{d}^{\mathrm{STRxy}} + \tilde{\boldsymbol{e}}^{\mathrm{STRx}}) && (62) \end{aligned}$$

The first derivative of S with respect to $\tilde{\boldsymbol{e}}^{\mathrm{STRx}}$ is

$$\begin{aligned} \frac{\partial S}{\partial \tilde{\boldsymbol{e}}^{\mathrm{STRx}}} &= 2 \tilde{\boldsymbol{P}}^{\mathrm{STRx}} \tilde{\boldsymbol{e}}^{\mathrm{STRx}} + 2 \sum_{y \neq x} \tilde{\boldsymbol{P}}^{\mathrm{STRy}} (\boldsymbol{d}^{\mathrm{STRxy}} + \tilde{\boldsymbol{e}}^{\mathrm{STRx}}) && (63) \\ &= 2 (\sum_y \tilde{\boldsymbol{P}}^{\mathrm{STRy}}) \tilde{\boldsymbol{e}}^{\mathrm{STRx}} + 2 \sum_{y \neq x} \tilde{\boldsymbol{P}}^{\mathrm{STRy}} \boldsymbol{d}^{\mathrm{STRxy}} && (64) \end{aligned}$$

Setting the first derivative to zero and solving for $\tilde{\boldsymbol{e}}^{\mathrm{STRx}}$ gives

$$\tilde{\boldsymbol{e}}^{\mathrm{STRx}} = -(\sum_y \tilde{\boldsymbol{P}}^{\mathrm{STRy}})^{-1} (\sum_{y \neq x} \tilde{\boldsymbol{P}}^{\mathrm{STRy}} \boldsymbol{d}^{\mathrm{STRxy}}). \tag{65}$$

By inserting this estimate of $\tilde{\boldsymbol{e}}^{\mathrm{STRx}}$ into Eq. (46), we obtain the optimal quaternion

$$\begin{aligned} \boldsymbol{q}^{\mathrm{optimal\,IRF \rightarrow}}\mathrm{SSRFx} &= \boldsymbol{q}^{\mathrm{measured\,IRF \rightarrow SSRFx}} (\boldsymbol{q}^{\mathrm{noise\,STRx}})^* && (66) \\ &= \boldsymbol{q}^{\mathrm{measured\,IRF \rightarrow SSRFx}} \begin{bmatrix} 1 \\ -0.5 \boldsymbol{e}^{\mathrm{STRx}} \end{bmatrix} && (67) \\ &= \boldsymbol{q}^{\mathrm{measured\,IRF \rightarrow SSRFx}} \begin{bmatrix} 1 \\ -0.5 \boldsymbol{R}^{\mathrm{GRF \rightarrow SSRFx}} \tilde{\boldsymbol{e}}^{\mathrm{STRx}} \end{bmatrix}. && (68) \end{aligned}$$

where $\boldsymbol{q}^{\mathrm{optimal\,IRF \rightarrow}}\mathrm{SSRFx}$ replaces $\boldsymbol{q}^{\mathrm{true\,IRF \rightarrow}}\mathrm{SSRFx}$.

4.2 Combination of angular velocities

Let $\boldsymbol{R}_k$ be the so-called mounting matrix describing the rotation from the GRF to the SSRF$_k$, where k is the identifier of the star sensor. The transformation for the k-th star sensor reads

$$\boldsymbol{\omega}_k^{(SSRF)} = \boldsymbol{R}_k \boldsymbol{\omega}_k^{(GRF)}. \tag{69}$$

The accuracy of the angular velocities in the SSRF$_k$ is represented by the covariance matrix

$$\boldsymbol{\Sigma}_k \equiv \Sigma(\boldsymbol{\omega}_k^{(SSRF)}) = \sigma^2 \begin{bmatrix} q_x & 0 & 0 \\ 0 & q_y & 0 \\ 0 & 0 & q_z \end{bmatrix}. \tag{70}$$

The top panel of Fig. 6 shows the power spectral densities (PSDs) of the angular velocities of a single star sensor in the associated SSRF. Assuming that PSDs largely reflect measurement noise above 10 mHz, we can conclude that the noise level of ω_z is ten times larger than the noise level of ω_x and ω_y in the SSRF. For this reason, we choose $q_x = q_y = 1$ and $q_z = 10^2$. Since the choice of σ^2 has no influence on the least-squares estimate of the angular velocities, we set $\sigma^2 = 1$ for convenience. Because the true angular velocities of the three star sensors are equal in the GRF, we assume that

$$\boldsymbol{\omega}^{(GRF)} \equiv E(\boldsymbol{\omega}_1^{(GRF)}) = E(\boldsymbol{\omega}_2^{(GRF)}) = E(\boldsymbol{\omega}_3^{(GRF)}), \tag{71}$$

where E is the expectation operator. Then, we obtain from Eq. (69)

$$E(\boldsymbol{\omega}_k^{(SSRF)}) = \boldsymbol{R}_k \boldsymbol{\omega}^{(GRF)}. \tag{72}$$

Assuming that the data of different star sensors are uncorrelated, the least-squares estimate of the angular velocities in the GRF is

$$\boldsymbol{\omega}^{(GRF)} = (\sum_k \boldsymbol{R}_k^T \boldsymbol{\Sigma}_k^{-1} \boldsymbol{R}_k)^{-1} \sum_k \boldsymbol{R}_k^T \boldsymbol{\Sigma}_k^{-1} \boldsymbol{\omega}_k^{(SSRF)}. \tag{73}$$

Fig. 7 shows that the angular velocities resulting from the star sensor combination do not suffer from the less accurately measured boresight component of the individual star sensors as it was the case in the lower plot of Fig. 6.

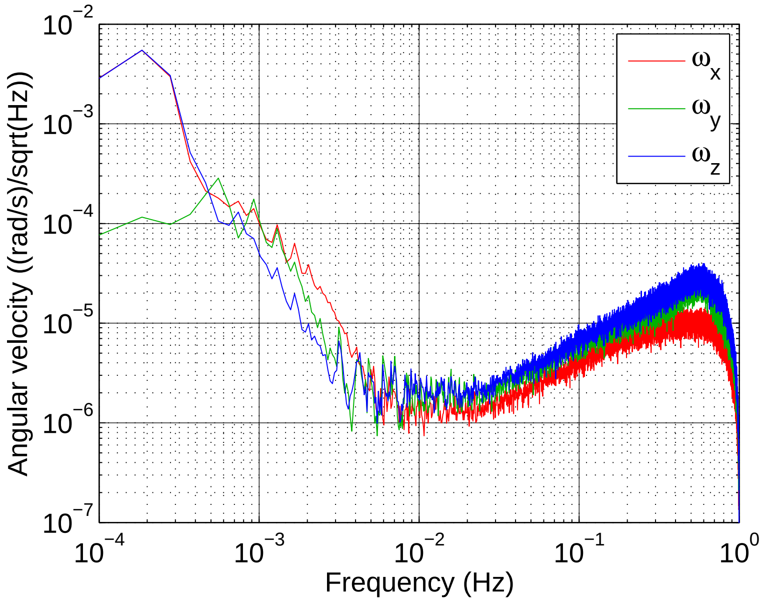

Figure 7: Angular velocities in the GRF resulting from the combination of star sensor one and two. The PSDs reflect measurement noise above 10 mHz. We used data of 23 Nov 2009 for this plot.

5 Redundancy

Eqs. (14) and (15) contain in total eleven independent unknowns per epoch: three linear accelerations $\boldsymbol{d}$, three angular velocities $\boldsymbol{\Omega}$, from which angular accelerations $\dot{\boldsymbol{\Omega}}$ follow by differentiation, and five independent gravity gradients $\boldsymbol{V}$, taking the trace condition

$$\mathrm{trace}(\boldsymbol{V}) = V_{xx} + V_{yy} + V_{zz} = 0 \tag{74}$$

into account. These unknowns are determined from 21 measurements per epoch: 18 accelerometer measurements $\boldsymbol{a}_i$, $i = 1, \ldots, 6$, and three angular velocities $\boldsymbol{\Omega}_S$ measured by the star sensors, from which angular accelerations $\dot{\boldsymbol{\Omega}}_S$ follow by differentiation. Thus, accelerometer and star sensor measurements are redundant and it is possible to find 21 - 11 = 10 conditions, which we derive in the following.

From Eq. (14) follow six are linear independent conditions

$$\boldsymbol{a}_{c,ij} - \boldsymbol{a}_{c,kl} \stackrel{!}{=} \boldsymbol{0}, \;\; ij \neq kl, \tag{75}$$

where E denotes the expectation operator. From Eq. (15) follows

$$\boldsymbol{A}_d \boldsymbol{L}^{-1} - \boldsymbol{L}^{-1} \boldsymbol{A}_d^T = \dot{\boldsymbol{\Omega}} \stackrel{!}{=} \dot{\boldsymbol{\Omega}}_S, \tag{76}$$

which gives three conditions since both the left and right-hand side of the equations are skew-symmetric matrices with zeros on the diagonal. Further, Eq. (15) gives

$$\boldsymbol{A}_d \boldsymbol{L}^{-1} + \boldsymbol{L}^{-1} \boldsymbol{A}_d^T = -\boldsymbol{V} + \boldsymbol{\Omega}^2 \stackrel{!}{=} -\boldsymbol{V} + \boldsymbol{\Omega}_S^2, \tag{77}$$

from which the last condition follows in combination with the trace condition $\mathrm{trace}(\boldsymbol{V}) = 0$.

$$\mathrm{trace}(\boldsymbol{A}_d \boldsymbol{L}^{-1} + \boldsymbol{L}^{-1} \boldsymbol{A}_d^T) = \mathrm{trace}(\boldsymbol{\Omega}^2) \stackrel{!}{=} \mathrm{trace}(\boldsymbol{\Omega}_S^2) \tag{78}$$

Eqs. (75)–(78) are used by several authors in different ways. In the following, we provide a short overview.

5.1 Approach of [Rispens and Bouman(2011)]

[Rispens and Bouman(2011)] use a (non-GOCE) gravity field model for calculating $\boldsymbol{V}$ and star sensor measurements $\dot{\boldsymbol{\Omega}}_S$ and $\boldsymbol{\Omega}_S^2$ in combination with Eq. (15) for estimating calibration parameters, which is in principal equivalent to using Eqs. (76) and (77). Further, they employ a stochastic model that accounts for temporal correlations in the conditions' misclosures. They demonstrate that this approach works well with nominal data. However, the validation of their results by gravity field models such as ITG-Grace2010s is limited by the model that was used for calculating $\boldsymbol{V}$.

5.2 Approach of [Kern et al.(2007)]

[Kern et al.(2007)] propose to filter Eqs. (75) and (77) to the frequency band 50–100 mHz and assume that $\boldsymbol{V} = \boldsymbol{0}$, both for shaking and nominal data. They use a stochastic model that accounts for correlations between the misclosures of different conditions. It should be noted that star sensor data is only used for determining the long wavelength part (frequencies lower than 10 mHz) of the angular velocities, which makes it difficult to estimate common scale factors reliably with this method, in particular from nominal data.

5.3 ESA's baseline method

ESA's baseline method described in [Frommknecht et al.(2011)], which we use as reference in Sect. 7 and 7.1, is tailored to the signals generated in a satellite shaking. These signals are the linear and angular accelerations in the frequency band 50–100 mHz and the angular accelerations at 1.3 mHz. The baseline method assumes that when shaking data is filtered to 50–100 mHz, Eq. (15) can be approximated by

$$\boldsymbol{A}_d = \frac{1}{2}\dot{\boldsymbol{\Omega}}\boldsymbol{L}, \tag{79}$$

which simplifies Eq. (77) to

$$\boldsymbol{A}_d\boldsymbol{L}^{-1} + \boldsymbol{L}^{-1}\boldsymbol{A}_d^T = \boldsymbol{0}. \tag{80}$$

Then, the calibration parameters are estimated in a two-step approach. In the first step, the baseline method uses Eqs. (75) and (80), filtered to the frequency band 50–100 mHz. Any deviation of the ICMs in Eq. (41) from a priori assumed values leads to misclosures in the conditions that are equal to linear combinations of the accelerations d_x, d_y, d_z, $\dot{\omega}_x$, $\dot{\omega}_y$ and $\dot{\omega}_z$, from which the calibration parameters are estimated. Since it is not possible to estimate all calibration parameters from the accelerometer data alone, the conditions are complemented by 28 additional conditions. For example, one of the additional conditions is that the average of the scale factors equals one. Consequently, the calibration parameters determined in the first step are regarded as relative calibration parameters. In the second step of the baseline method, the absolute scale factor of the gradiometer and the relative orientation of the gradiometer and star sensors are determined by fitting the angular velocities of gradiometer to those of the star sensors, both filtered to a frequency band that is 1 mHz wide and centred at 1.3 mHz. While the absolute scale factor is used to scale the relative calibration parameters obtained in the first step, the relative orientation is not further used.

5.4 Ideal approach

From a methodological point of view, Eqs. (75)–(78) should be used directly to determine calibration parameters. In the following, we outline how this works and where one encounters numerical problems. It should be pointed out that, as a side effect, one determines also adjusted accelerometer and star sensor measurements, from which gravity gradients can be calculated. Thus, the purpose of the method described in the following is not only to determine calibration parameters, but also to calculate gravity gradients. The later is currently performed in the gradiometer Level 1b processing as described in Sect. 8.

Let us first consider measurement noise $\tilde{\boldsymbol{n}}_i$ in the uncalibrated accelerations $\tilde{\boldsymbol{a}}_i$. Then, Eq. (39) changes to

$$\boldsymbol{a}_i + \boldsymbol{n}_i = \boldsymbol{M}_i(\tilde{\boldsymbol{a}}_i + \tilde{\boldsymbol{n}}_i), \tag{81}$$

where $\boldsymbol{n}_i$ is measurement noise in the calibrated accelerations $\boldsymbol{a}_i$. Further, let us denote noise in the star sensor angular rates $\omega_{S,x}$, $\omega_{S,y}$, and $\omega_{S,z}$ by $\phi_{S,x}$, $\phi_{S,y}$, and $\phi_{S,z}$, respectively. Then, inserting Eq. (81) into Eq. (75) gives

$$\frac{1}{2}(\boldsymbol{M}_i(\tilde{\boldsymbol{a}}_i + \tilde{\boldsymbol{n}}_i) + \boldsymbol{M}_j(\tilde{\boldsymbol{a}}_j + \tilde{\boldsymbol{n}}_j)) - \frac{1}{2}(\boldsymbol{M}_k(\tilde{\boldsymbol{a}}_k + \tilde{\boldsymbol{n}}_k) + \boldsymbol{M}_l(\tilde{\boldsymbol{a}}_l + \tilde{\boldsymbol{n}}_l)) = \boldsymbol{0}, \quad ij \neq kl. \tag{82}$$

Further, Eq. (76) changes to

$$\boldsymbol{A}_d \boldsymbol{L}^{-1} - \boldsymbol{L}^{-1} \boldsymbol{A}_d^T = \dot{\boldsymbol{\Omega}}_S + \dot{\boldsymbol{\Phi}}_S, \tag{83}$$

where

$$\begin{aligned} \boldsymbol{A}_d &= \frac{1}{2}\left[\boldsymbol{M}_1(\tilde{\boldsymbol{a}}_{d,1} + \tilde{\boldsymbol{n}}_{d,1}) \quad \boldsymbol{M}_2(\tilde{\boldsymbol{a}}_{d,2} + \tilde{\boldsymbol{n}}_{d,2}) \quad \boldsymbol{M}_3(\tilde{\boldsymbol{a}}_{d,3} + \tilde{\boldsymbol{n}}_{d,3})\right] \\ &\quad -\frac{1}{2}\left[\boldsymbol{M}_4(\tilde{\boldsymbol{a}}_{d,4} + \tilde{\boldsymbol{n}}_{d,4}) \quad \boldsymbol{M}_5(\tilde{\boldsymbol{a}}_{d,5} + \tilde{\boldsymbol{n}}_{d,5}) \quad \boldsymbol{M}_6(\tilde{\boldsymbol{a}}_{d,6} + \tilde{\boldsymbol{n}}_{d,6})\right]. \end{aligned} \tag{84}$$

Finally, Eq. (78) becomes

$$\mathrm{trace}(\boldsymbol{A}_d)\boldsymbol{L}^{-1} + \boldsymbol{L}^{-1}\boldsymbol{A}_d^T) = \mathrm{trace}((\boldsymbol{\Omega}_S + \boldsymbol{\Phi}_S)^2), \tag{85}$$

where $\boldsymbol{A}_d$ is defined as in Eq. (84).

The conditions in Eqs. (82)–(85) are non-linear functions of observations and calibration parameters. Therefore, the calibration parameters should be estimated in a mixed model least-squares adjustment from the statistical point of view. We discuss later on the problems ones encounters when implementing this approach. The linearized conditions have the general form

$$\boldsymbol{0} = \boldsymbol{f}(\boldsymbol{x}, \boldsymbol{v}) \approx \boldsymbol{f}(\boldsymbol{x}_0, \boldsymbol{v}_0) + \boldsymbol{A}(\boldsymbol{x} - \boldsymbol{x}_0) + \boldsymbol{B}^T(\boldsymbol{v} - \boldsymbol{v}_0). \tag{86}$$

The covariance matrix $\boldsymbol{\Sigma}$ of the observations can be modelled as block-diagonal matrix, where each block is symmetric Toeplitz matrix. The least-squares estimates of the parameters and residuals read

$$\boldsymbol{x} = \boldsymbol{x}_0 + (\boldsymbol{A}^T(\boldsymbol{B}^T\boldsymbol{Q}\boldsymbol{B})^{-1}\boldsymbol{A})^{-1}\boldsymbol{A}^T(\boldsymbol{B}^T\boldsymbol{Q}\boldsymbol{B})^{-1}(\boldsymbol{B}^T\boldsymbol{v}_0 - \boldsymbol{f}(\boldsymbol{x}_0, \boldsymbol{v}_0)) \tag{87}$$

and

$$\boldsymbol{v} = -\boldsymbol{Q}\boldsymbol{B}(\boldsymbol{B}^T\boldsymbol{Q}\boldsymbol{B})^{-1}(\boldsymbol{f}(\boldsymbol{x}_0, \boldsymbol{v}_0) + \boldsymbol{A}(\boldsymbol{x} - \boldsymbol{x}_0) - \boldsymbol{B}^T\boldsymbol{v}_0), \tag{88}$$

respectively.

Since Eqs. (83) and (85) contain star sensor angular accelerations and star sensor anguler velocities. These can be related by $\dot{\omega}_{S,x}(n) = \frac{\omega_{S,x}(n+1)-\omega_{S,x}(n-1)}{2\Delta t}$, which needs to be taken into account when determining matrix $\boldsymbol{B}$.

Let us define $\boldsymbol{I}_{+1}$ and $\boldsymbol{I}_{-1}$ as shift matrices, for example

$$\underset{3\times3}{\boldsymbol{I}_{+1}} = \begin{bmatrix} 0 & 1 & 0 \\ 0 & 0 & 1 \\ 0 & 0 & 0 \end{bmatrix} \quad \underset{3\times3}{\boldsymbol{I}_{-1}} = \begin{bmatrix} 0 & 0 & 0 \\ 1 & 0 & 0 \\ 0 & 1 & 0 \end{bmatrix}. \tag{89}$$

Then, matrix $\boldsymbol{B}$ has the following structure.

$$\underset{10N\times21N}{\boldsymbol{B}^T} = \begin{bmatrix} \underset{6\times18}{\boldsymbol{H}_1} \otimes \underset{N\times N}{\boldsymbol{I}} & \underset{6N\times N}{\boldsymbol{0}} & \underset{6N\times N}{\boldsymbol{0}} & \underset{6N\times N}{\boldsymbol{0}} \\ \underset{1\times18}{\boldsymbol{H}_2} \otimes \underset{N\times N}{\boldsymbol{I}} & \frac{1}{2\Delta t}\underset{N\times N}{(\boldsymbol{I}_{+1} - \boldsymbol{I}_{-1})} & \underset{N\times N}{\boldsymbol{0}} & \underset{N\times N}{\boldsymbol{0}} \\ \underset{1\times18}{\boldsymbol{H}_3} \otimes \underset{N\times N}{\boldsymbol{I}} & \underset{N\times N}{\boldsymbol{0}} & \frac{1}{2\Delta t}\underset{N\times N}{(\boldsymbol{I}_{+1} - \boldsymbol{I}_{-1})} & \underset{N\times N}{\boldsymbol{0}} \\ \underset{1\times18}{\boldsymbol{H}_4} \otimes \underset{N\times N}{\boldsymbol{I}} & \underset{N\times N}{\boldsymbol{0}} & \underset{N\times N}{\boldsymbol{0}} & \frac{1}{2\Delta t}\underset{N\times N}{(\boldsymbol{I}_{+1} - \boldsymbol{I}_{-1})} \\ \underset{1\times18}{\boldsymbol{H}_5} \otimes \underset{N\times N}{\boldsymbol{I}} & \underset{N\times N}{\mathrm{diag}(\boldsymbol{\omega}_{S,x})} & \underset{N\times N}{\mathrm{diag}(\boldsymbol{\omega}_{S,y})} & \underset{N\times N}{\mathrm{diag}(\boldsymbol{\omega}_{S,z})} \end{bmatrix} \tag{90}$$

Note that this structure assumes that $\omega_{S,x}(0)$, $\omega_{S,y}(0)$, $\omega_{S,z}(0)$, $\omega_{S,x}(N+1)$, $\omega_{S,y}(N+1)$, $\omega_{S,z}(N+1)$ are estimated as additional parameters.

Matrix $\boldsymbol{B}^T\boldsymbol{Q}\boldsymbol{B}$ is symmetric and positive definite, but has no Toeplitz structure, mainly because the last N rows of $\boldsymbol{B}^T$ contain diagonal matrices with non-constant diagonals. Further, N should be at least in the order of 10^5 in case of a sampling rate of 1 Hz, such that the stochastic model utilized for matrix $\boldsymbol{Q}$ can capture the increase in the noise PSD below the measurement band. Thus, the calculation of $\boldsymbol{A}^T(\boldsymbol{B}^T\boldsymbol{Q}\boldsymbol{B})^{-1}\boldsymbol{A}$ is numerically very demanding and cannot be performed on a single PC in praxis. For this reason, we do not pursue this approach.

Note that alternatively one can treat ω_x, ω_y and ω_z as parameters. Then, matrix $\boldsymbol{B}^T\boldsymbol{Q}\boldsymbol{B}$ is a block-matrix, where each block is a symmetric Toeplitz matrix. This allows for using vector-autoregressive (VAR) filters (cite Hamilton and Whittle) to efficiently apply $(\boldsymbol{B}^T\boldsymbol{Q}\boldsymbol{B})^{-1}$ to a vector or matrix with not too many columns. Since in this case, $\boldsymbol{A}$ would have more than $3N$ columns due to the angular velocities, a direct computation of $\boldsymbol{A}^T(\boldsymbol{B}^T\boldsymbol{Q}\boldsymbol{B})^{-1}\boldsymbol{A}$ is not an option. One could use the pre-conditioned conjugate gradient (PCG) algorithm to solve $\boldsymbol{A}^T(\boldsymbol{B}^T\boldsymbol{Q}\boldsymbol{B})^{-1}\boldsymbol{A}(\boldsymbol{x} - \boldsymbol{x}_0) = \boldsymbol{A}^T(\boldsymbol{B}^T\boldsymbol{Q}\boldsymbol{B})^{-1}(\boldsymbol{B}^T\boldsymbol{v}_0 - \boldsymbol{f}(\boldsymbol{x}_0, \boldsymbol{v}_0))$ since matrix-vector products of type $\boldsymbol{A}\boldsymbol{x}$ and $\boldsymbol{A}^T\boldsymbol{y}$ are easily calculated due to the sparseness of matrix $\boldsymbol{A}$. A good pre-conditioner is a must in this case because matrix $(\boldsymbol{A}^T(\boldsymbol{B}^T\boldsymbol{Q}\boldsymbol{B})^{-1}\boldsymbol{A})$ has a bad conditioner number (tests showed it is in the order of 10^7). However, we did not find a matrix that can be implemented in praxis while approximating $(\boldsymbol{A}^T(\boldsymbol{B}^T\boldsymbol{Q}\boldsymbol{B})^{-1}\boldsymbol{A})$ well enough to improve the condition number of the problem significantly.

6 Calibration of the gradiometer measurements

During the research fellowship, a method for estimating calibration parameters from nominal as well as shaking data was developed on the basis of [Kern et al.(2007)]. The method is based on twelve conditions for accelerometer and star sensor data as well as a stochastic model for the misclosures in these conditions. The latter is the new and unique feature of the method due to which it is possible to estimate calibration parameters not only from shaking data but also from nominal data. Moreover, we made important modifications to the conditions presented in [Kern et al.(2007)]. In Sect. 6.1, we outline the method before providing a detailed description of the conditions and the stochastic model, in Sect. 6.2 and Sect. 6.3, respectively. Results of the calibration for November 2009 to May 2010 are presented in Sect. 7. The validation of these results is documented in Sect. 7.1.

6.1 Outline of the estimation method

An overview over the method is provided by the flowchart in Fig. 8. In the following, we explain the individual boxes in the flowchart. We start by writing the conditions in the form

$$\mathbf{0} = \boldsymbol{f}(\boldsymbol{x}) + \boldsymbol{e} \tag{91}$$

where $\mathbf{0} = \boldsymbol{f}(\boldsymbol{x})$ are the conditions, $\boldsymbol{x}$ contains the calibration parameters, and $\boldsymbol{e}$ are the misclosures in the conditions. The conditions are described in detail in Sect. 6.2. Because $\boldsymbol{f}(\boldsymbol{x})$ is non-linear in our case, we linearize it by means of a Taylor series expansion truncated after the linear term:

$$\boldsymbol{f}(\boldsymbol{x}) = \boldsymbol{f}(\boldsymbol{x}_0) + \boldsymbol{J}(\boldsymbol{x}_0)(\boldsymbol{x} - \boldsymbol{x}_0) \tag{92}$$

Here, $\boldsymbol{J}(\boldsymbol{x}_0)$ is the Jacobian matrix, i.e. the matrix of the first derivatives of $\boldsymbol{f}(\boldsymbol{x})$. Inserting Eq. (92) into Eq. (91) yields the linearized conditions

$$\boldsymbol{J}\boldsymbol{x}_0 - \boldsymbol{f} = \boldsymbol{J}\boldsymbol{x} + \boldsymbol{e}, \tag{93}$$

where $\boldsymbol{J} \equiv \boldsymbol{J}(\boldsymbol{x}_0)$ and $\boldsymbol{f} \equiv \boldsymbol{f}(\boldsymbol{x}_0)$. The calibration parameters are estimated by minimizing $\vec{e}^T \boldsymbol{\Sigma}^{-1} \vec{e}$, where $\boldsymbol{\Sigma} \equiv \boldsymbol{\Sigma}(\boldsymbol{e})$ is the covariance matrix. It is described in detail in Sect. 6.3. The estimated calibration parameters are obtained by

$$\begin{aligned} \boldsymbol{x} &= (\boldsymbol{J}^T \boldsymbol{\Sigma}^{-1} \boldsymbol{J})^{-1} \boldsymbol{J}^T \boldsymbol{\Sigma}^{-1} (\boldsymbol{J}\boldsymbol{x}_0 - \boldsymbol{f}) \\ &= \boldsymbol{x}_0 - (\boldsymbol{J}^T \boldsymbol{\Sigma}^{-1} \boldsymbol{J})^{-1} \boldsymbol{J}^T \boldsymbol{\Sigma}^{-1} \boldsymbol{f}. \end{aligned} \tag{94}$$

The computation of the calibration parameters according to Eq. (94) involves the inverse of the covariance matrix. In our application, we compute 90 sets of calibration parameters for the period 1 Nov 2009 to 17 May 2010. Since each set is based on two days of nominal data, the size of $\boldsymbol{\Sigma}$ is 2073600×2073600 where $2073600 = 12$ conditions $\times$ 172800 seconds (the sampling

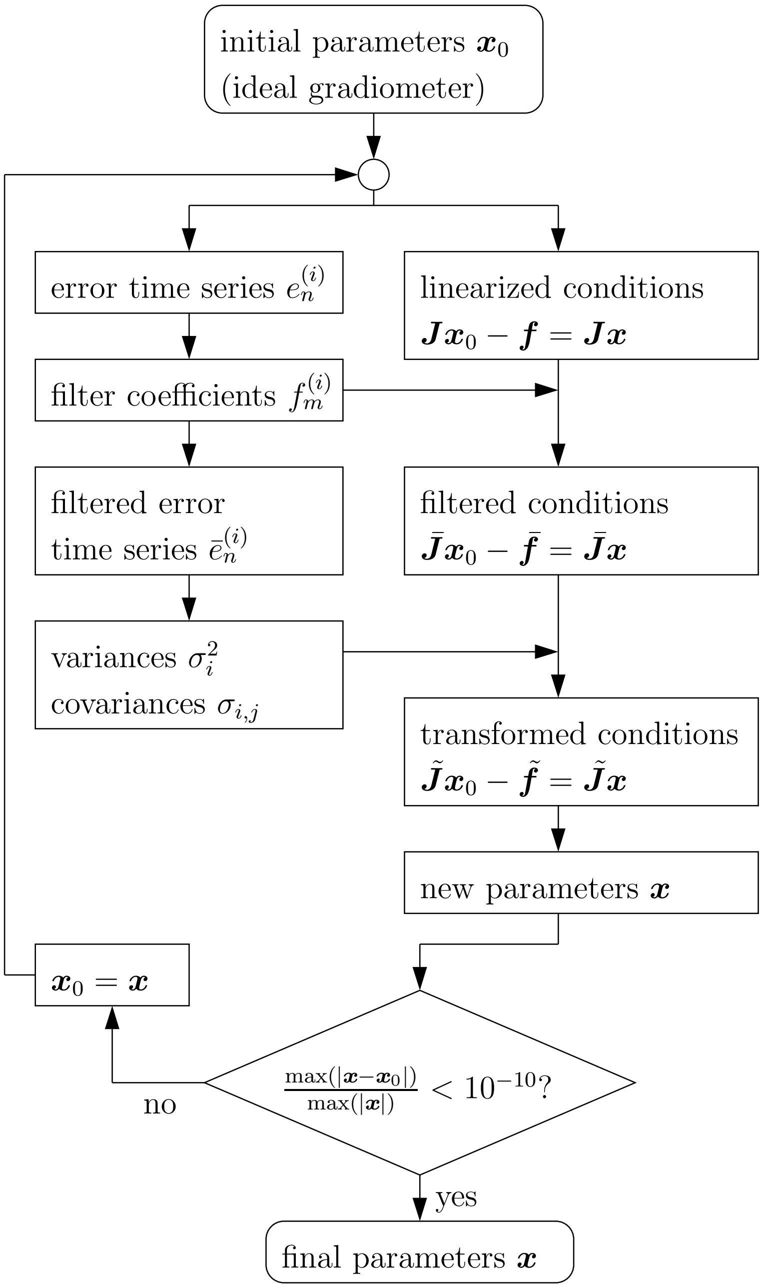

Figure 8: Flowchart of the method for the estimation of calibration parameters, using the same symbols as in Sect. 6.1 to 6.3.

period is one second). Furthermore, the computation of one set of calibration parameters involves approximately 30 iterations due to the linearization and the stochastic model (cf. Fig. 8). For all these reasons, it is in our application practically impossible to compute Eq. (94) in a straight forward way on a single PC in a reasonable time. However, we can tremendously reduce the complexity of the computation by factorizing the inverse covariance matrix according to

$$(\boldsymbol{\Sigma}(\boldsymbol{e}))^{-1} = \boldsymbol{F}^T \boldsymbol{G}^T \boldsymbol{G} \boldsymbol{F}. \tag{95}$$

Here, $\boldsymbol{F}$ models the temporal correlations of the misclosure time series in the individual conditions while $\boldsymbol{G}$ models the variances of and covariances between the misclosure time series of the different conditions. A detailed derivation of $\boldsymbol{F}$ and $\boldsymbol{G}$ is provided in Sect. 6.3.1 and 6.3.2, respectively. We use the factorization in Eq. (95) for transforming the linearized conditions in Eq. (93) in to steps. The first step yields

$$\bar{\boldsymbol{J}} \boldsymbol{x}_0 - \bar{\boldsymbol{f}} = \bar{\boldsymbol{J}} \boldsymbol{x} + \bar{\boldsymbol{e}}, \tag{96}$$

where $\bar{\boldsymbol{J}} = \boldsymbol{F}\boldsymbol{J}$, $\bar{\boldsymbol{f}} = \boldsymbol{F}\boldsymbol{f}$ and $\bar{\boldsymbol{e}} = \boldsymbol{F}\boldsymbol{e}$. The second steps gives

$$\tilde{\boldsymbol{J}} \boldsymbol{x}_0 - \tilde{\boldsymbol{f}} = \tilde{\boldsymbol{J}} \boldsymbol{x} + \tilde{\boldsymbol{e}}, \tag{97}$$

where $\tilde{\boldsymbol{J}} = \boldsymbol{G}\bar{\boldsymbol{J}}$, $\tilde{\boldsymbol{f}} = \boldsymbol{G}\bar{\boldsymbol{f}}$ and $\tilde{\boldsymbol{e}} = \boldsymbol{G}\bar{\boldsymbol{e}}$. Since the covariance matrix of the transformed misclosures is

$$\boldsymbol{\Sigma}(\tilde{e}) = \boldsymbol{G}\boldsymbol{F}(\boldsymbol{F}^T \boldsymbol{G}^T \boldsymbol{G}\boldsymbol{F})^{-1}(\boldsymbol{G}\boldsymbol{F})^T = \boldsymbol{I}, \tag{98}$$

the calibration parameters are computed by

$$\boldsymbol{x} = \boldsymbol{x}_0 - (\tilde{\boldsymbol{J}}^T \tilde{\boldsymbol{J}})^{-1} \tilde{\boldsymbol{J}}^T \tilde{\boldsymbol{f}}. \tag{99}$$

This equation needs to be computed several times, each time $\boldsymbol{x}_0$ being $\boldsymbol{x}$ of the previous computation, until the truncation error in Eq. (92) becomes sufficiently small. A good choice for the initial $\boldsymbol{x}_0$ are calibration parameters corresponding to an ideal gradiometer, i.e. all scale factors are equal to one and all other calibration parameters are equal to zero. Using a good initial $\boldsymbol{x}_0$ is particularly important for the modelling of temporal correlations in the conditions.

6.2 Conditions for gradiometer and star sensor data

The twelve conditions comprise of six conditions for CM accelerations and six conditions for DM accelerations similar to those in [Kern et al.(2007)]. They result from linear combinations of Eq. (14) and (15). The conditions are formulated in terms of calibrated CM and DM accelerations, which we regard as a linear function of the calibration parameters according to Eq. (41). In the following, we list the function $\boldsymbol{f}(\boldsymbol{x})$ of the conditions in Eq. (91). The conditions for CM accelerations are given by

$$f^{(1)} = (a_{c,36,x} - a_{c,25,x})(\frac{1}{s_{3,x}} + \frac{1}{s_{6,x}} + \frac{1}{s_{2,x}} + \frac{1}{s_{5,x}}), \tag{100}$$

$$f^{(2)} = (a_{c,36,x} - a_{c,14,x})(\frac{1}{s_{3,x}} + \frac{1}{s_{6,x}} + \frac{1}{s_{1,x}} + \frac{1}{s_{4,x}}), \tag{101}$$

$$f^{(3)} = (a_{c,14,z} - a_{c,36,z})(\frac{1}{s_{1,z}} + \frac{1}{s_{4,z}} + \frac{1}{s_{3,z}} + \frac{1}{s_{6,z}}), \tag{102}$$

$$f^{(4)} = (a_{c,25,y} - a_{c,14,y})(\frac{1}{s_{2,y}} + \frac{1}{s_{5,y}} + \frac{1}{s_{1,y}} + \frac{1}{s_{4,y}}), \tag{103}$$

$$f^{(5)} = (a_{c,25,z} - a_{c,14,z})(\frac{1}{s_{2,z}} + \frac{1}{s_{5,z}} + \frac{1}{s_{1,z}} + \frac{1}{s_{4,z}}) \tag{104}$$

and

$$f^{(6)} = (a_{c,36,y} - a_{c,25,y})(\frac{1}{s_{3,y}} + \frac{1}{s_{6,y}} + \frac{1}{s_{2,y}} + \frac{1}{s_{5,y}}), \tag{105}$$

where the superscript serves as an identifier for the condition. The conditions are composed of two parts: The first part containing a difference of CM accelerations is based on Eq. (14). The second part containing a sum of reciprocal scaling factors is required for the following reason. If the condition was only the difference of CM accelerations, it would be fulfilled when all calibration parameters are equal to zero. Thus, the least-squares estimate of the calibration parameters would be biased towards zero. This contradicts in particular our expectation that the scaling factors are approximately equal to one. The purpose of the second factor is to counteract such a biased estimation. The conditions hold for all frequencies.

Three of the six conditions for DM accelerations use angular accelerations $\dot{\boldsymbol{\omega}}$ measured by the star sensors:

$$f^{(7)} = \frac{1}{L_y} a_{d,25,z} - \frac{1}{L_z} a_{d,36,y} - \dot{\omega}_x \tag{106}$$

$$f^{(8)} = \frac{1}{L_z} a_{d,36,x} - \frac{1}{L_x} a_{d,14,z} - \dot{\omega}_y \tag{107}$$

$$f^{(9)} = \frac{1}{L_x} a_{d,14,y} - \frac{1}{L_y} a_{d,25,x} - \dot{\omega}_z \tag{108}$$

The conditions are based on linear combinations of Eq. (15). The angular accelerations $\dot{\boldsymbol{\omega}}$ are computed by first using Eq. (73) to obtain angular velocities $\boldsymbol{\omega}$, then applying numerical differentiation. The conditions hold for all frequencies.

The final three conditions are different for nominal and shaking data. In both cases the conditions are based on Eq. (15). The conditions hold only in the upper measurement bandwidth (UMB) ranging from 50–100 mHz, in which the gravity gradient signal is much smaller than the DM acceleration noise [Cesare and Catastini(2008)]. Therefore, we assume $\boldsymbol{V} = \boldsymbol{0}$ in the UMB.

In case of nominal data, we assume that also the centrifugal accelerations are much smaller than the DM acceleration noise in the UMB. This means that $\boldsymbol{\Omega}^2 = \boldsymbol{0}$ in addition to $\boldsymbol{V} = \boldsymbol{0}$ in

Eq. (15), leading to the following conditions:

$$f^{(10)} = 2a_{d,14,x}(\frac{1}{s_{1,x}} + \frac{1}{s_{4,x}}) \tag{109}$$

$$f^{(11)} = 2a_{d,25,y}(\frac{1}{s_{2,y}} + \frac{1}{s_{5,y}}) \tag{110}$$

$$f^{(12)} = 2a_{d,36,z}(\frac{1}{s_{3,z}} + \frac{1}{s_{6,z}}) \tag{111}$$

These conditions are composed of two parts: Differential mode accelerations and sums of reciprocal scaling factors. The latter have the same purpose as in Eqs. (100)–(105).

The satellite shaking is designed to generate pseudo-random linear and angular accelerations in the UMB and angular accelerations at 1.3 mHz. Thus, the centrifugal accelerations $\boldsymbol{\Omega}^2(\boldsymbol{p}_i - \boldsymbol{p}_j)$ are non-zero in the UMB in case of shaking data. Consequently, we assume only $\boldsymbol{V} = \boldsymbol{0}$ in Eq. (15), leading to the following conditions:

$$f^{(10)} = 2a_{d,14,x} + L_x(\omega_y^2 + \omega_z^2) \tag{112}$$

$$f^{(11)} = 2a_{d,25,y} + L_y(\omega_x^2 + \omega_z^2) \tag{113}$$

$$f^{(12)} = 2a_{d,36,z} + L_z(\omega_x^2 + \omega_y^2) \tag{114}$$

Here, the angular velocities $\boldsymbol{\omega}$ are computed from star sensor data according to Eq. (73).

The accelerometer and star sensor data are recorded at a fixed sampling rate. This means that accelerations, angular velocities and angular accelerations are available in form of time series. This gives us the options to sort the elements of $\boldsymbol{f}$ in Eq. (91) either by condition or by time. Because it supports the factorization in Eq. (95), we arrange the conditions in the following way:

$$\boldsymbol{f} = \begin{bmatrix} \boldsymbol{f}^{(1)} \\ \vdots \\ \boldsymbol{f}^{(12)} \end{bmatrix}, \quad \text{where} \quad \boldsymbol{f}^{(i)} = \begin{bmatrix} f_1^{(i)} \\ \vdots \\ f_N^{(i)} \end{bmatrix} \tag{115}$$

Then, the vector $\boldsymbol{f}$ comprises of twelve time series $f_n^{(i)}$, where the superscript i is the identifier of the condition and the subscript n corresponds to the time.

6.3 Covariance matrix

The measured CM and DM accelerations as well as the angular velocities computed from star sensor data contain measurement noise. The measurement noise propagates to the misclosure $\boldsymbol{e}$ in Eq. (91). When setting up the covariance matrix $\boldsymbol{\Sigma}(\boldsymbol{e})$, we need to take into account that

- misclosures in the different conditions are correlated,
- misclosures in the individual conditions are correlated in time and
- the variance of the misclosures is different for each condition.

Correlations between the misclosures in different conditions result from the fact that the conditions use the same accelerometer and star sensor data. Correlations in time result from e.g. the numerical differentiation when deriving angular accelerations from star sensor attitude data. Different variances can be justified by the fact that e.g. the accelerometers have ultra-sensitive and less-sensitive axes.

The arrangement of the conditions as indicated in Eq. (115) implies that the vector $\boldsymbol{e}$ comprises of twelve misclosure time series $e_n^{(i)}$. According to this arrangement, the covariance matrix can be written as

$$\boldsymbol{\Sigma}(\boldsymbol{e}) = \begin{bmatrix} \sigma_1^2 \boldsymbol{Q}_{1,1} & \sigma_{1,2}\boldsymbol{Q}_{1,2} & \cdots & \sigma_{1,12}\boldsymbol{Q}_{1,12} \\ \sigma_{2,1}\boldsymbol{Q}_{2,1} & \sigma_2^2\boldsymbol{Q}_{2,2} & \cdots & \sigma_{2,12}\boldsymbol{Q}_{2,12} \\ \vdots & \vdots & \ddots & \vdots \\ \sigma_{12,1}\boldsymbol{Q}_{12,1} & \sigma_{12,2}\boldsymbol{Q}_{12,2} & \cdots & \sigma_{12}^2\boldsymbol{Q}_{12,12} \end{bmatrix}, \tag{116}$$

where $\boldsymbol{Q}_{i,j} \equiv \boldsymbol{Q}(\boldsymbol{e}^{(i)}, \boldsymbol{e}^{(j)})$ is the covariance matrix of the misclosure time series $e_n^{(i)}$ and $e_n^{(j)}$, which models the correlations in time. The variances σ_i^2 and the covariances $\sigma_{i,j}$ model the correlations between the misclosures in the different conditions and the variances of the misclosures in the individual conditions.

In our application, the blocks $\boldsymbol{Q}_{i,j}$ are huge in size. As already mentioned, we use two days of nominal data recorded at a sampling rate of 1 Hz, which results in blocks $\boldsymbol{Q}_{i,j}$ of size 172800×172800. However, we assume that the misclosure time series are stationary which seems justified from the analysis of misclosures in the conditions (see Fig. 9– 12). Note that we require stationarity only for a period of two days. Then, the diagonal blocks are symmetric Toeplitz matrices

$$\boldsymbol{Q}_{i,i} = \begin{bmatrix} \gamma_0^{(i)} & \gamma_1^{(i)} & \cdots & \gamma_{N-1}^{(i)} \\ \gamma_1^{(i)} & \gamma_0^{(i)} & \cdots & \gamma_{N-2}^{(i)} \\ \vdots & \vdots & \ddots & \vdots \\ \gamma_{N-1}^{(i)} & \gamma_{N-2}^{(i)} & \cdots & \gamma_0^{(i)} \end{bmatrix}, \tag{117}$$

where $\gamma_0^{(i)}, \ldots, \gamma_{N-1}^{(i)}$ are the autocovariances of the misclosure time series $e_n^{(i)}$. Furthermore, the off-diagonal blocks are Toeplitz matrices

$$\boldsymbol{Q}_{i,j} = \begin{bmatrix} \gamma_0^{(i,j)} & \gamma_1^{(i,j)} & \cdots & \gamma_{N-1}^{(i,j)} \\ \gamma_{-1}^{(i,j)} & \gamma_0^{(i,j)} & \cdots & \gamma_{N-2}^{(i,j)} \\ \vdots & \vdots & \ddots & \vdots \\ \gamma_{1-N}^{(i,j)} & \gamma_{2-N}^{(i,j)} & \cdots & \gamma_0^{(i,j)} \end{bmatrix}, \tag{118}$$

where $\gamma_{1-N}^{(i,j)}, \ldots, \gamma_{N-1}^{(i,j)}$ are the cross-covariances of the misclosure time series $e_n^{(i)}$ and $e_n^{(j)}$.

In the following, we derive the matrices $\boldsymbol{F}$ and $\boldsymbol{G}$ in Eq. (95) from the covariance matrix $\boldsymbol{\Sigma}(\boldsymbol{e})$, assuming that it has the structure in Eq. (116). Moreover, we show how the multiplication by these matrices can be implemented efficiently.

6.3.1 Derivation of matrix $\boldsymbol{F}$

The Toeplitz structure of the blocks $\boldsymbol{Q}_{i,i}$ allows for the modelling of the correlations in time of the individual misclosure time series $e_n^{(i)}$ by a whole range of numerical efficient operators, confer [Schuh(1996)] for an overview. We choose symmetric moving-average (SMA) decorrelation operators, which are defined by

$$\bar{e}_n^{(i)} = \sum_{m=-M}^{M} f_m^{(i)} e_{n-m}^{(i)}, \quad f_{-m}^{(i)} = f_m^{(i)}, \tag{119}$$

where $f_m^{(i)}$ are the coefficients of the decorrelation operator, $e_n^{(i)}$ is the correlated misclosure time series, $\bar{e}_n^{(i)}$ is the decorrelated misclosure time series and M is the order of the decorrelation operator. We show examples of the decorrelated misclosure time series $\bar{e}_n^{(i)}$ in Fig. 9– 12. The effect of the decorrelation becomes particularly visible for $i = 4, \ldots, 9$. The coefficients of the decorrelation operator can be derived in the following way.

The power spectral density (PSD) of the misclosure time series $P_e^{(i)}(\omega)$ is the Fourier transform of the autocovariances $\gamma_n^{(i)}$:

$$P_e^{(i)}(\omega) = F(\gamma_n^{(i)}) \tag{120}$$

The PSD of the decorrelated misclosure time series $P_{\bar{e}}^{(i)}(\omega)$ is related to $P_e^{(i)}(\omega)$ by

$$P_{\bar{e}}^{(i)}(\omega) = P_f^{(i)}(\omega) P_e^{(i)}(\omega), \tag{121}$$

where $P_f^{(i)}(\omega)$ is the PSD of the SMA decorrelation operator. The objective is that the time series $\bar{e}_n^{(i)}$ corresponds to white noise, which implies $P_{\bar{e}}^{(i)}(\omega) = \text{const}$. Thus, we choose the coefficients $f_m^{(i)}$ such that

$$P_f^{(i)}(\omega) = \frac{1}{P_e^{(i)}(\omega)}. \tag{122}$$

The PSD of the SMA decorrelation operator is related to the coefficients $f_m^{(i)}$ by

$$|F(f_m^{(i)})|^2 = P_f^{(i)}(\omega), \tag{123}$$

where $F(f_m^{(i)})$ denotes the Fourier transform of the coefficients. Note that the sign of $F(f_m^{(i)})$ is irrelevant. The only restriction is that $F(f_m^{(i)})$ is a real and even function, because the

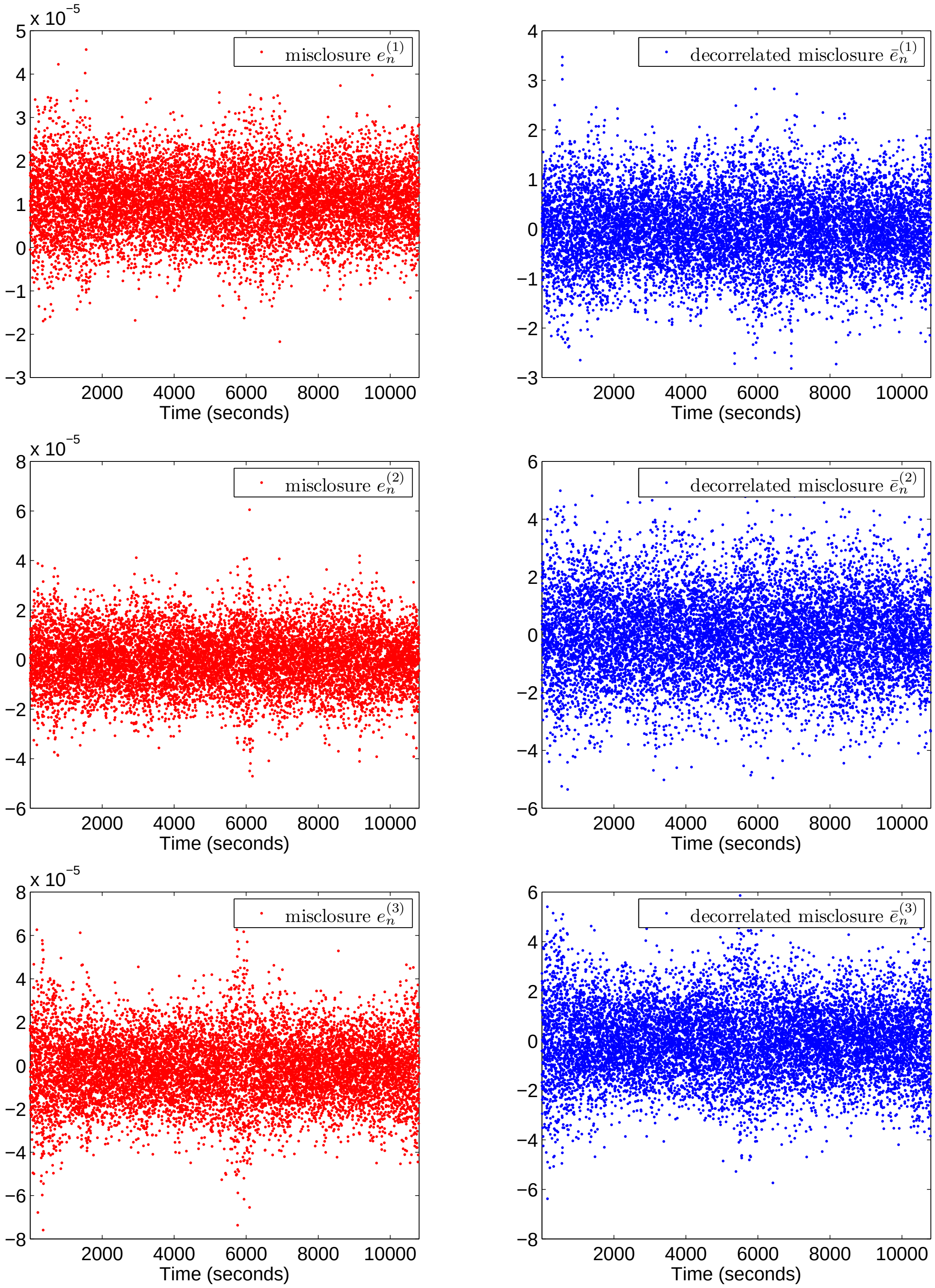

Figure 9: Misclosures $e_n^{(i)}$ and decorrelated misclosures $\bar{e}_n^{(i)}$ for $i = 1, 2, 3$.

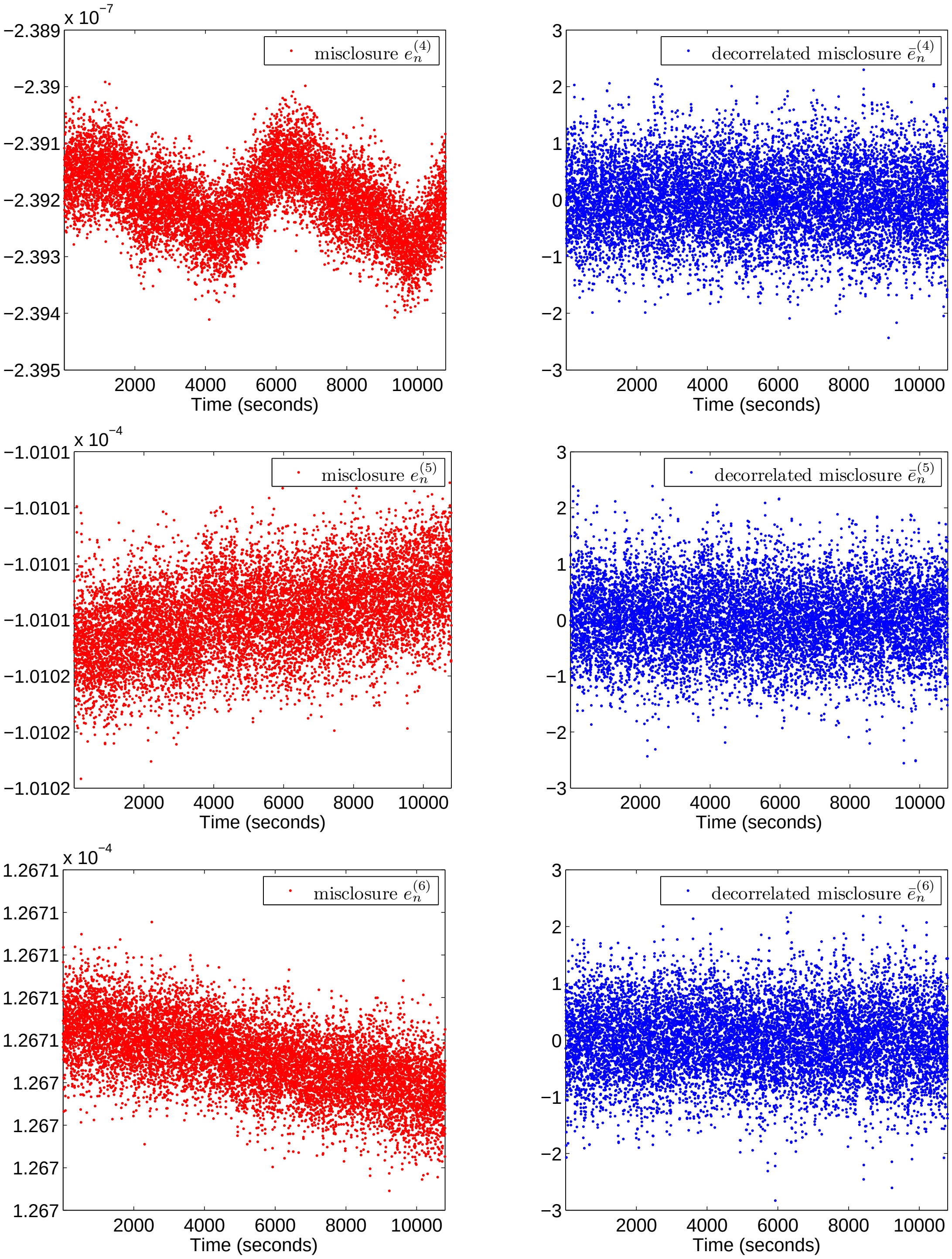

Figure 10: Misclosures $e_n^{(i)}$ and decorrelated misclosures $\bar{e}_n^{(i)}$ for $i = 4, 5, 6$.

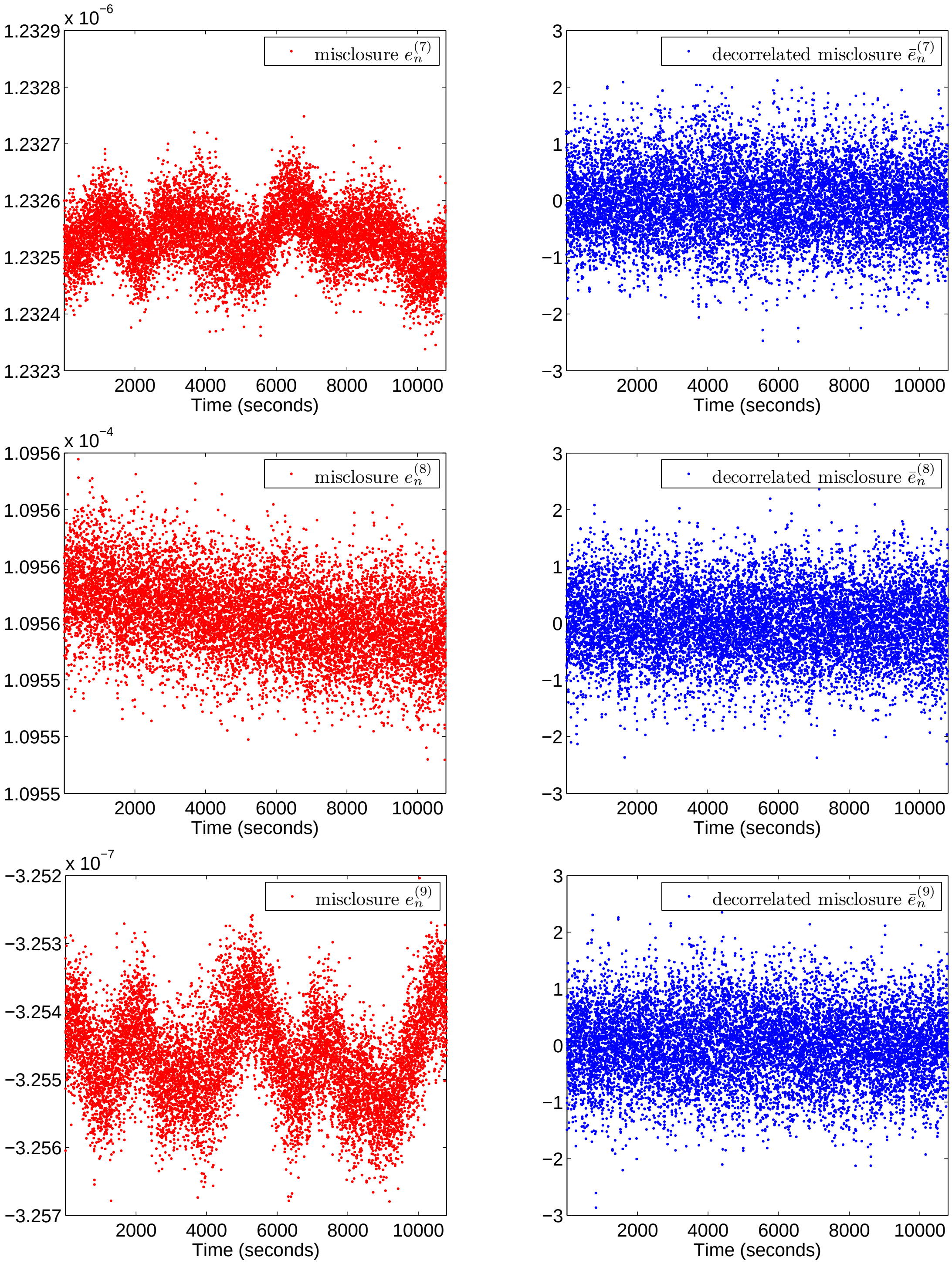

Figure 11: Misclosures $e_n^{(i)}$ and decorrelated misclosures $\bar{e}_n^{(i)}$ for $i = 7, 8, 9$.

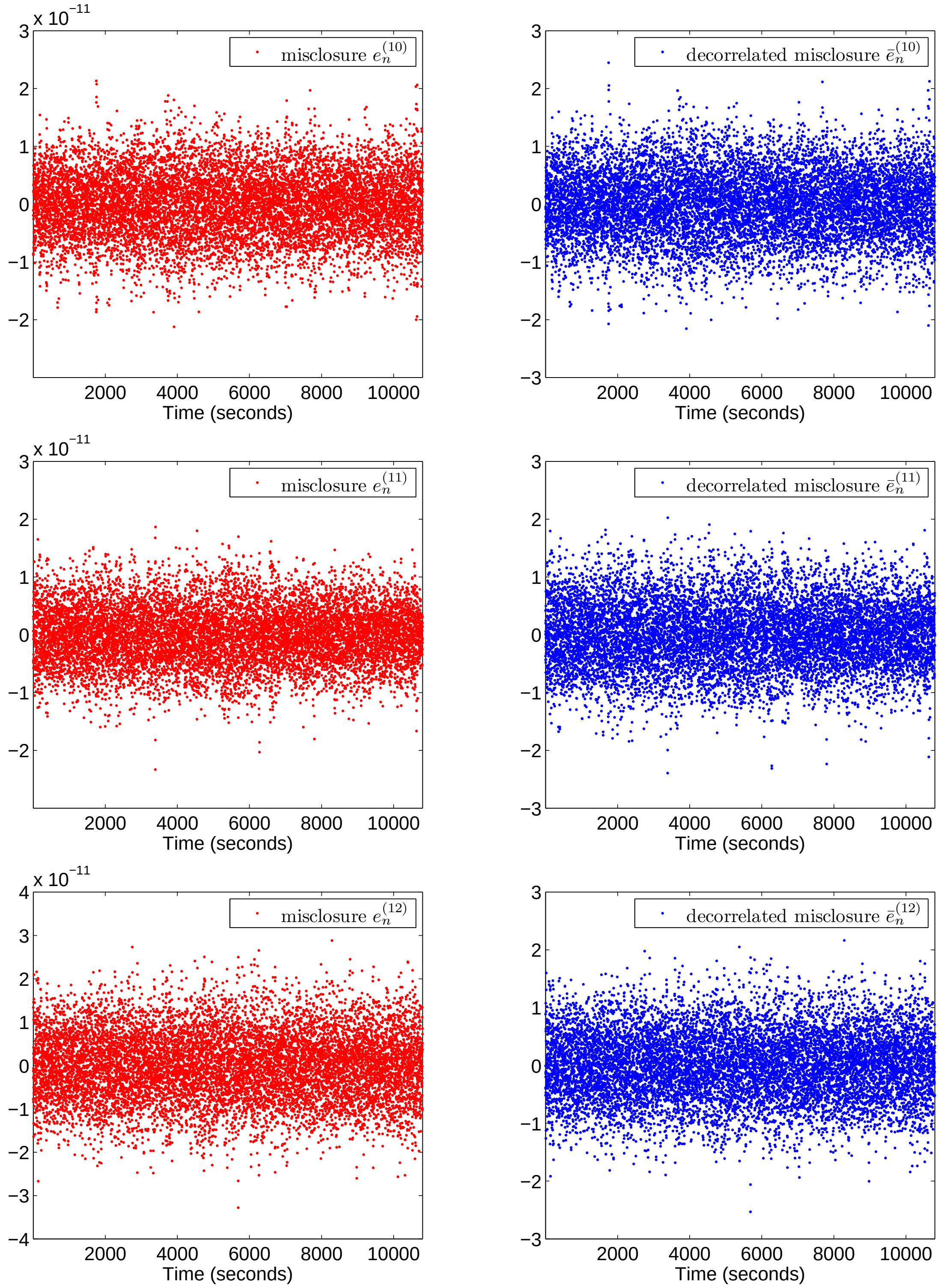

Figure 12: Misclosures $e_n^{(i)}$ and decorrelated misclosures $\bar{e}_n^{(i)}$ for $i = 10, 11, 12$.

coefficients $f_m^{(i)}$ are real and $f_{-m}^{(i)} = f_m^{(i)}$. Therefore, the coefficients can be obtained by

$$f_m^{(i)} = F^{-1}(\sqrt{P_f^{(i)}(\omega)}), \tag{124}$$

where F^{-1} denotes the inverse Fourier transform.

The coefficients $f_m^{(i)}$ enter the matrix $\boldsymbol{F}$ in the following way. Eq. (119) for filtering a single misclosure time series can be written in matrix notation as

$$\bar{\boldsymbol{e}}^{(i)} = \boldsymbol{F}_i \boldsymbol{e}^{(i)}, \tag{125}$$

where

$$\boldsymbol{F}_i = \begin{bmatrix} f_0^{(i)} & f_1^{(i)} & \dots & f_M^{(i)} & & \\ f_1^{(i)} & f_0^{(i)} & \ddots & & \ddots & \\ \vdots & \ddots & \ddots & \ddots & & f_M^{(i)} \\ f_M^{(i)} & & \ddots & \ddots & \ddots & \\ & \ddots & & \ddots & f_0^{(i)} & f_1^{(i)} \\ & & f_M^{(i)} & \dots & f_1^{(i)} & f_0^{(i)} \end{bmatrix}. \tag{126}$$

Then, decorrelating all misclosure time series can be written as

$$\bar{\boldsymbol{e}} = \boldsymbol{F}\boldsymbol{e}, \tag{127}$$

where $\bar{\boldsymbol{e}}$ contains the decorrelated misclosure time series and

$$\boldsymbol{F} = \begin{bmatrix} \boldsymbol{F}_1 & & \\ & \ddots & \\ & & \boldsymbol{F}_{12} \end{bmatrix}. \tag{128}$$

Let us investigate the effect of the decorrelation operator on the covariance matrix. By covariance propagation we find

$$\begin{aligned} \boldsymbol{\Sigma}(\bar{\boldsymbol{e}}) &= \boldsymbol{F}\boldsymbol{\Sigma}(\boldsymbol{e})\boldsymbol{F}^T \\ &= \begin{bmatrix} \sigma_1^2 \boldsymbol{F}_1 \boldsymbol{Q}_{1,1} \boldsymbol{F}_1^T & \dots & \sigma_{1,12} \boldsymbol{F}_1 \boldsymbol{Q}_{1,12} \boldsymbol{F}_{12}^T \\ \vdots & \ddots & \vdots \\ \sigma_{12,1} \boldsymbol{F}_{12} \boldsymbol{Q}_{1,12} \boldsymbol{F}_{12}^T & \dots & \sigma_{12}^2 \boldsymbol{F}_{12} \boldsymbol{Q}_{12,12} \boldsymbol{F}_{12}^T \end{bmatrix}. \end{aligned} \tag{129}$$

We have computed coefficients for which $P_{\bar{e}}^{(i)}(\omega) = \text{const}$. Since the autocovariances $\bar{\gamma}_n^{(i)}$ of the filtered time series $\bar{e}_n^{(i)}$ are related to the PSD by the inverse Fourier transform $\bar{\gamma}_n^{(i)} = F^{-1}(P_{\bar{e}}^{(i)}(\omega))$, it follows that

$$\bar{\gamma}_n^{(i)} = \begin{cases} \text{const}, & n = 0 \\ 0, & n \neq 0 \end{cases}. \tag{130}$$

Therefore, the diagonal blocks are

$$Q(\bar{\boldsymbol{e}}^{(i)}, \bar{\boldsymbol{e}}^{(i)}) = \boldsymbol{F}_i \boldsymbol{Q}_{i,i} \boldsymbol{F}_i^T \propto \boldsymbol{I}. \tag{131}$$

The off-diagonal blocks $Q(\bar{\boldsymbol{e}}^{(i)}, \bar{\boldsymbol{e}}^{(j)})$ reflect the cross-covariances $\gamma_n^{(i,j)}$ between the time series $\bar{e}_n^{(i)}$ and $\bar{e}_n^{(j)}$. Since $\bar{e}_n^{(i)}$ and $\bar{e}_n^{(j)}$ have no correlations in time, we assume that also their cross-covariances shows no correlations in time. Based on this assumption we find

$$\bar{\gamma}_n^{(i,j)} = \begin{cases} \text{const}, & n = 0 \\ 0, & n \neq 0 \end{cases}, \tag{132}$$

which leads to

$$Q(\bar{\boldsymbol{e}}^{(i)}, \bar{\boldsymbol{e}}^{(j)}) = \boldsymbol{F}_i \boldsymbol{Q}_{i,j} \boldsymbol{F}_j^T \propto \boldsymbol{I}. \tag{133}$$

Thus, the covariance matrix of the decorrelated misclosure time series is

$$\boldsymbol{\Sigma}(\bar{\boldsymbol{e}}) = \begin{bmatrix} \sigma_1^2 & \dots & \sigma_{1,12} \\ \vdots & \ddots & \vdots \\ \sigma_{12,1} & \dots & \sigma_{12}^2 \end{bmatrix} \otimes \boldsymbol{I}, \tag{134}$$

where $\otimes$ denotes the Kronecker product.

6.3.2 Derivation of matrix $\boldsymbol{G}$

The next step is to choose matrix $\boldsymbol{G}$ in

$$\tilde{\boldsymbol{e}} = \boldsymbol{G}\boldsymbol{F}\boldsymbol{e} = \boldsymbol{G}\bar{\boldsymbol{e}} \tag{135}$$

such that

$$\boldsymbol{\Sigma}(\tilde{\boldsymbol{e}}) = \boldsymbol{G}\boldsymbol{\Sigma}(\bar{\boldsymbol{e}})\boldsymbol{G}^T = \boldsymbol{I}. \tag{136}$$

Let $\boldsymbol{U}$ be the upper triangular matrix resulting from the Cholesky factorization

$$\boldsymbol{U}^T\boldsymbol{U} = \begin{bmatrix} \sigma_1^2 & \dots & \sigma_{1,12} \\ \vdots & \ddots & \vdots \\ \sigma_{12,1} & \dots & \sigma_{12}^2 \end{bmatrix}. \tag{137}$$

Then, the covariance matrix of the decorrelated time series can be expressed by

$$\boldsymbol{\Sigma}(\bar{\boldsymbol{e}}) = \boldsymbol{U}^T\boldsymbol{U} \otimes \boldsymbol{I} = (\boldsymbol{U} \otimes \boldsymbol{I})^T(\boldsymbol{U} \otimes \boldsymbol{I}), \tag{138}$$

where the right-hand side is the Cholesky factorization of $\boldsymbol{\Sigma}(\bar{\boldsymbol{e}})$. Therefore, we set

$$\boldsymbol{G} = (\boldsymbol{U} \otimes \boldsymbol{I})^{-T} = \boldsymbol{U}^{-T} \otimes \boldsymbol{I}. \tag{139}$$

For the covariance matrix of $\tilde{\boldsymbol{e}}$ we find

$$\begin{aligned}\boldsymbol{\Sigma}(\tilde{\boldsymbol{e}}) &= \boldsymbol{G}\boldsymbol{\Sigma}(\bar{\boldsymbol{e}})\boldsymbol{G}^T \\ &= (\boldsymbol{U}^{-T} \otimes \boldsymbol{I})(\boldsymbol{U}^T\boldsymbol{U} \otimes \boldsymbol{I})(\boldsymbol{U}^{-T} \otimes \boldsymbol{I})^T \\ &= \boldsymbol{U}^{-T}\boldsymbol{U}^T\boldsymbol{U}\boldsymbol{U}^{-1} \otimes \boldsymbol{III} \\ &= \boldsymbol{I}. \end{aligned} \tag{140}$$

6.3.3 Practical implementation

The PSD of the misclosure time series is obtained in the following way. Based on the calibration parameters we compute the misclosure time series $e_n^{(i)}$. Then, we estimate the PSD of the misclosure time series $P_e^{(i)}(\omega)$ by Welch's method [Welch(1967)] using a Hanning window for reducing spectral leakage [Harris(1978)]. Next, we set the PSD of the SMA decorrelation operators equal to the inverse PSD of the misclosure time series according to Eq. (122). Before we proceed with the computation of the coefficients of the SMA decorrelation operators, we need to consider that

- the accelerometer biases cause biases in the misclosure time series,
- different de-aliasing filters have been applied to accelerometer and star sensor data, and
- a subset of the conditions hold only in the UMB.

In order to avoid any influence of biases, we set $P_f(\omega) = 0$ for $\omega = 0\,\text{Hz}$. In this way, we obtain SMA decorrelation operators which remove any biases from the misclosure time series. Different de-aliasing filters were applied to accelerometer and star sensor data, which causes systematic differences in the high frequencies. For this reason, we set $P_f(\omega) = 0$ for $\omega > 0.2\,\text{Hz}$. In case of the conditions which hold only for the UMB, we set $P_f(\omega) = 0$ for $\omega \notin [0.05\,\text{Hz}, 0.1\,\text{Hz}]$. The effect of the latter is that the SMA decorrelation operators model the correlations inside the UMB and, at the same time, are bandpass filters with the UMB as passband.

The next step is the computation of the decorrelation operator coefficients according to Eq. (124). Applying the SMA decorrelation operator to the misclosure time series yields the decorrelated misclosure time series $\bar{e}_n^{(i)}$. Based on the latter, we estimate variances and covariances by

$$\sigma_i^2 = \frac{1}{N}\sum_{n=1}^{N}(\bar{e}_n^{(i)})^2 \tag{141}$$

and

$$\sigma_{i,j} = \frac{1}{N}\sum_{n=1}^{N}\bar{e}_n^{(i)}\bar{e}_n^{(j)}, \tag{142}$$

respectively. Finally, we compute new calibration parameters based on the decorrelation operator coefficients, variances and covariances. This procedure is repeated until the calibration parameters converge (cf. Fig. 8).

The matrix $\tilde{\boldsymbol{J}}$ and the vector $\tilde{\boldsymbol{f}}$ in Eq. (99) are computed in two steps. The first step is the computation of

$$\bar{\boldsymbol{J}} = \boldsymbol{F}\boldsymbol{J} = \begin{bmatrix} \boldsymbol{F}_1\boldsymbol{J}_1 \\ \vdots \\ \boldsymbol{F}_{12}\boldsymbol{J}_{12} \end{bmatrix} \text{ and } \bar{\boldsymbol{f}} = \boldsymbol{F}\boldsymbol{f} = \begin{bmatrix} \boldsymbol{F}_1\boldsymbol{f}_1 \\ \vdots \\ \boldsymbol{F}_{12}\boldsymbol{f}_{12} \end{bmatrix}. \tag{143}$$

The products $\boldsymbol{F}_i\boldsymbol{J}_i$ and $\boldsymbol{F}_i\boldsymbol{f}_i$ correspond to the convolution of the columns of the matrices $\boldsymbol{J}_i$ and vectors $\boldsymbol{f}_i$ with the decorrelation operator coefficients $f_m^{(i)}$ according to Eq. (119). The convolution can be implemented efficiently using fast Fourier transform (FFT) techniques. The second step is the computation of

$$\tilde{\boldsymbol{J}} = \boldsymbol{G}\bar{\boldsymbol{J}} = (\boldsymbol{U}^{-T} \otimes \boldsymbol{I})\bar{\boldsymbol{J}} = \begin{bmatrix} \sum_{i=1}^{1} U_{1,i}^{-T}\bar{\boldsymbol{J}}_i \\ \vdots \\ \sum_{i=1}^{12} U_{12,i}^{-T}\bar{\boldsymbol{J}}_i \end{bmatrix} \tag{144}$$

and

$$\tilde{\boldsymbol{f}} = \boldsymbol{G}\bar{\boldsymbol{f}} = (\boldsymbol{U}^{-T} \otimes \boldsymbol{I})\bar{\boldsymbol{f}} = \begin{bmatrix} \sum_{i=1}^{1} U_{1,i}^{-T}\bar{\boldsymbol{f}}_i \\ \vdots \\ \sum_{i=1}^{12} U_{12,i}^{-T}\bar{\boldsymbol{f}}_i \end{bmatrix}, \tag{145}$$

where $U_{m,n}^{-T}$ is the element of the matrix $\boldsymbol{U}^{-T}$ in the m-th row and n-th column.

6.3.4 Example for correlations in time

In order to show that in particular the modelling of temporal correlations is vital for the developed method, we show in Fig. 13 an example of the PSDs of the misclosure time series $e_n^{(i)}$. Depending on the noise characteristic, we can subdivide the misclosure time series into four groups: The misclosure time series $e_n^{(1)}$, $e_n^{(2)}$ and $e_n^{(3)}$ are computed according to Eqs. (100)–(102) from data of the ultra-sensitive accelerometer axes only. The computation of the misclosure time series $e_n^{(4)}$, $e_n^{(5)}$ and $e_n^{(6)}$ according to Eqs. (100)–(102) involves data of less sensitive accelerometer axes, leading to a higher noise level in comparison to the misclosure time series $e_n^{(1)}$, $e_n^{(2)}$ and $e_n^{(3)}$. Furthermore, the misclosure time series $e_n^{(7)}$, $e_n^{(8)}$ and $e_n^{(9)}$ are based angular accelerations which are obtained by double numerical differentiation of the star sensor attitude data, resulting in coloured noise whose PSD is approximately proportional to f^4, where f is the frequency. The misclosure time series $e_n^{(10)}$, $e_n^{(11)}$ and $e_n^{(12)}$ are computed according to Eqs. (109)–(111) using only accelerometer data of ultra-sensitive axes. In comparison to the misclosure time series $e_n^{(1)}$, $e_n^{(2)}$ and $e_n^{(3)}$, half the number of accelerations are used in the conditions, leading to lower noise level.

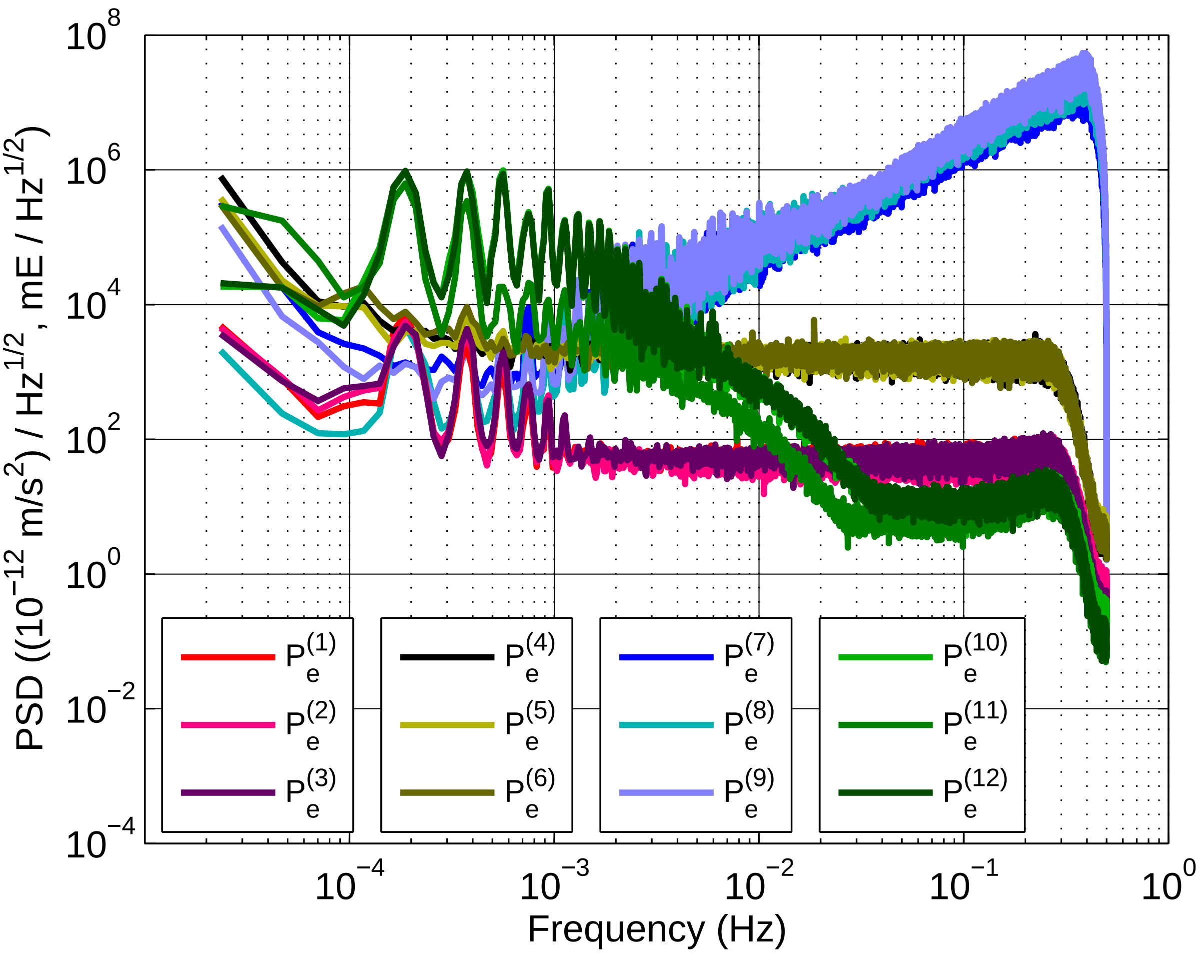

Figure 13: PSDs of the misclosure time series. The PSDs show that the conditions can be subdivided into four groups based on the noise characteristics. We plotted a different legend box for each group. We used data of 19 and 20 Nov 2009 for this plot. It should be noted that $P_e^{(7)}$, $P_e^{(8)}$ and $P_e^{(9)}$ are shown in the unit $10^{-12}s^{-2}/\sqrt{Hz}$ while the other PSDs are shown in the unit $10^{-12}\mathrm{m\,s}^{-2}/\sqrt{Hz}$.

7 Results of calibration parameter estimation

Using the method presented in this report, we computed time series of calibration parameters for the period from 1 Nov 2009 to 17 May 2010. Each element of the time series is based on two days of nominal data. We used the following Level 1b products as input for the method.

- EGG_NOM_1b (EGG_NCD_DS dataset)
  nominal CM and DM accelerations
- STR_VC2_1b, STR_VC3_1b
  star sensor inertial attitude quaternions
- AUX_EGG_DB
  lengths of the gradiometer arms,
  rotation matrices relating the SSRFs to the GRF

Details on these products can be found in the GOCE L1b products user handbook [SERCO/DATAMAT Consortium(2008)]. The data of the star sensors are combined using the method described in App. 4.

In addition to the time series based on nominal data, we computed calibration parameters from shaking data of 8/9 Oct 2009, 11/12 Jan 2010, 4/5 Mar 2010 and 6/7 May 2010. Each satellite shaking lasted one day.

In Fig. 14 we show time series of three elements of the ICMs together with the results from four satellite shakings. For comparison, we also show the elements of the ICMs computed by the baseline method of the ground processing, which are shown in [Frommknecht et al.(2011)], too. The input data for the baseline method was exactly the same data that we used, i.e. the same CM and DM accelerations as well as the same angular velocities of the combination of the star sensors.

The time series shown in Fig. 14 reveal that the calibration parameters change over time, which can be seen most clearly in the top panel of Fig. 14. These changes can be characterized as slow drifts. In order to assess the magnitude of the drifts in a simple way, we approximate the time series of the elements of the ICMs by a linear trend (red line in Fig. 14). Note that the purpose of the trend is thus not to provide the best possible description of the temporal evolution. Because the time series contain some outliers, which result from outliers in the accelerometer and star sensor data, we use a robust estimator (cf. App. A). Table 2 lists the slopes of the linear trends, which we interpret as a measure for the drifts in the calibration parameters. The drifts are in the order of 10^{-4} to 10^{-5} for scale factors (diagonal elements of $\boldsymbol{M}_{ij}$) and 10^{-5} to 10^{-6} for shear and rotation parameters (off-diagonal elements of $\boldsymbol{M}_{ij}$). This indicates a very stable behaviour of the gradiometer over time.

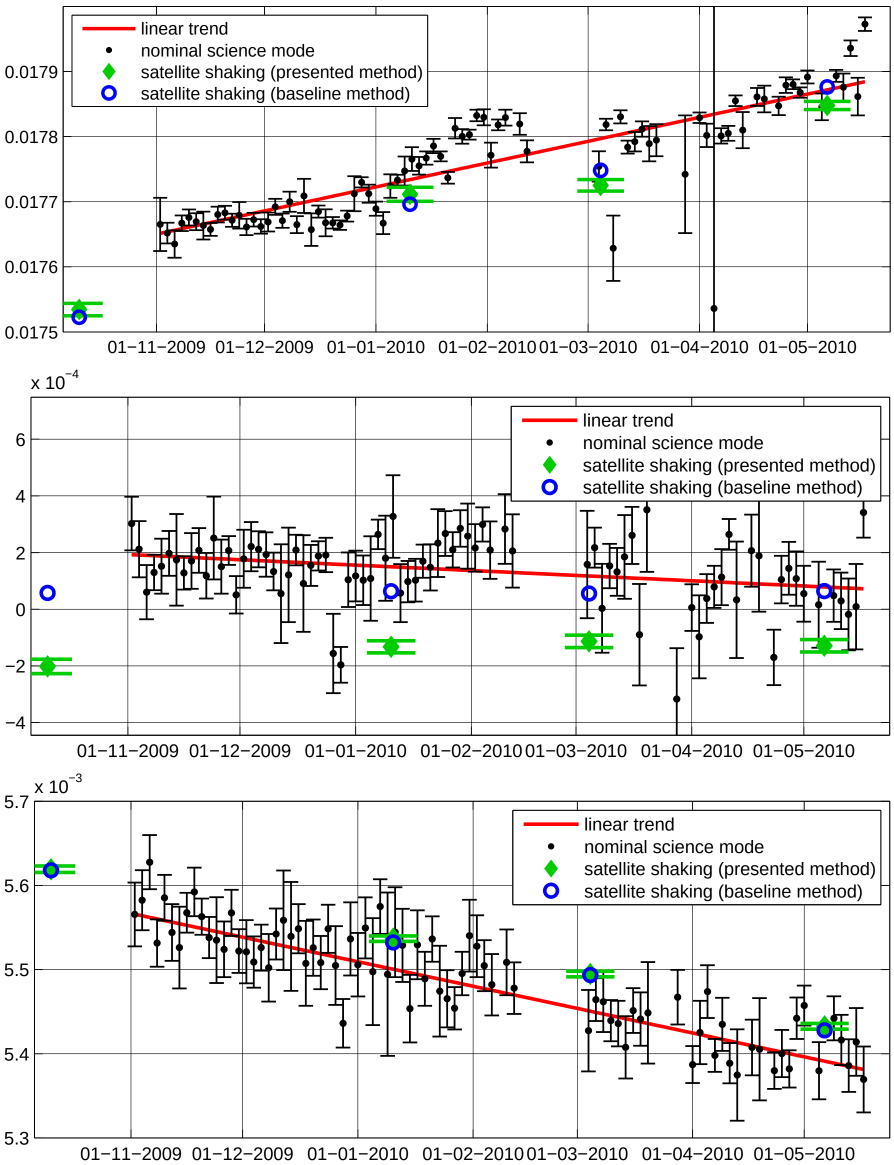

Figure 14: Time series of selected elements of the ICMs. The top panel shows the element in row four and column one of $\boldsymbol{M}_{14}$ (related to mapping of linear acceleration d_x onto calibrated DM acceleration $a_{d,14,x}$) as an example of significant drifts. The middle panel shows the element in row four and column six of $\boldsymbol{M}_{14}$ (related to mapping of uncalibrated DM acceleration $\tilde{a}_{d,14,z}$ onto calibrated DM acceleration $a_{d,14,x}$) as an example of systematic differences. The bottom panel shows the element in row five and column two of $\boldsymbol{M}_{25}$ (related to mapping of linear acceleration d_y onto calibrated DM acceleration $a_{d,25,y}$) as an example of the smaller standard deviation of results based on data recorded during the satellite shakings. The error bars reflect $\pm 2\sigma$, where σ is the standard deviation estimated in the least-squares adjustment.

Table 2: Drifts of calibration parameters (slope of red lines in Fig. 14) in 10^{-6}/month.

ICM $\boldsymbol{M}_{14}$, rows 4–6					
$\boldsymbol{D}_{14}$			$\boldsymbol{C}_{14}$		
37 ± 2	2 ± 2	-1 ± 1	-11 ± 14	0 ± 5	-19 ± 7
2 ± 34	75 ± 20	1 ± 10	-54 ± 53	-121 ± 64	2 ± 8
-7 ± 5	3 ± 3	43 ± 2	-8 ± 17	1 ± 2	-76 ± 20
ICM $\boldsymbol{M}_{25}$, rows 4–6					
$\boldsymbol{D}_{25}$			$\boldsymbol{C}_{25}$		
-20 ± 2	59 ± 2	0 ± 1	-44 ± 14	0 ± 5	-18 ± 7
0 ± 34	-29 ± 20	-4 ± 10	-34 ± 53	-52 ± 64	1 ± 8
-27 ± 5	2 ± 3	2 ± 2	-1 ± 17	-1 ± 2	-149 ± 20
ICM $\boldsymbol{M}_{36}$, rows 4–6					
$\boldsymbol{D}_{36}$			$\boldsymbol{C}_{36}$		
-3 ± 2	0 ± 2	3 ± 1	-62 ± 14	0 ± 5	-20± 7
0 ± 34	-3 ± 20	44 ± 10	-12 ± 53	-169 ± 64	35± 8
-10 ± 5	0 ± 3	1 ± 2	-8 ± 17	1 ± 2	-125± 20

When we compare the time series based on nominal data with the results from shaking data in Fig. 14, we observe for some elements of the ICMs systematic differences. This can be most clearly seen in the middle panel of Fig 14. One source of these differences is the different characteristics of nominal and shaking data, due to which we use different conditions in the method (cf. Sect. 6). Furthermore, we observe some systematic differences between the results of the presented method and the baseline method for shaking data. Since the input data for both methods have been the same, the conclusion is that also the methodology itself contributes to the systematic differences. Whether the systematic differences have a significant impact on the calibrated gravity gradients is discussed in Sect. 7.1.

Another interesting feature in Fig. 14 is that the results based on shaking data have smaller formal errors than the time series based on nominal data. This indicates that the pseudo-random signals generated in the course of the satellite shaking improve the precision of the estimated calibration parameters.

7.1 Validation

The validation of the estimated calibration parameters is subdivided into four steps. In Sect. 7.2, we verify the drifts of the calibration parameters by investigating the gravity gradient trace computed for each day in November and December 2009. In Sect. 7.3, we compare the performance of the different calibration methods on the basis of the gravity gradient trace and differences of calibrated gravity gradients to the ITG-Grace2010s gravity field model. In Sect. 7.4, we analyze the sensitivity of gravity gradients to biases in the ICMs. The purpose of this is to identify the ICM elements that are responsible for the differences in the performance of the gravity gradients. In Sect. 7.5, we highlight the connection between a prominent signature in the cross-track CM accelerations $a_{c,25,y}$ and the gravity gradient V_{yy} that we observe near the magnetic poles. Moreover, we discuss the relation of that signature and the calibration parameters.

7.2 Verification of drifts in the calibration parameters

The quality of the gravity gradients is degraded when the slow drifts in the calibration parameters are not taken into account. In order to demonstrate this, we calibrate nominal data from November and December 2009 in two different ways.

The first way is using the nearest ICM in the past, which means in our case using the ICMs of October 2009. This is equivalent to the implementation of the gradiometer calibration in the ground processing that was used for the first official release of GOCE data. Meanwhile, the ground processing was upgraded [Stummer et al.(2011)]. In particular, the gradiometer calibration was upgraded such that the nearest ICMs in the past and future are linearly interpolated. This is the second way in which we calibrate nominal data, which means that we linearly interpolate the ICMs of October 2009 and January 2010. In this report, we refer to the first way of calibrating gradiometer data as the old implementation in the ground processing and to the second way as the current implementation in the ground processing.

It should be noted that the work presented in this paper as well as the work of [Bouman et al.(2010)], who study the linear interpolation of one ICM element, namely the differential scale factor $\Delta s_{25,y}$, and the work of [Stummer et al.(2011)], who suggest a different reconstruction of the angular velocities from gradiometer and star sensor data, triggered the upgrade of the ground processing.

We compute gravity gradients from both sets of calibrated nominal data. Fig. 15 shows the square-roots of the power spectral densities (PSDs) of the gravity gradient trace computed for each day in November and December 2009. We may note that the gravity gradient trace should be equal to zero in case of perfect gravity gradients. We can clearly see that it worsens over time in the frequency band 1–10 mHz when the ICM of October 2009 is used. In contrast, we do not see any worsening over time when the ICMs are interpolated. This motivates studying the linear interpolation of the ICMs further.

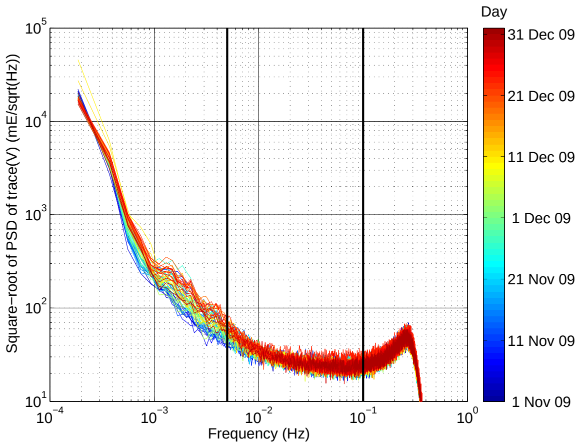

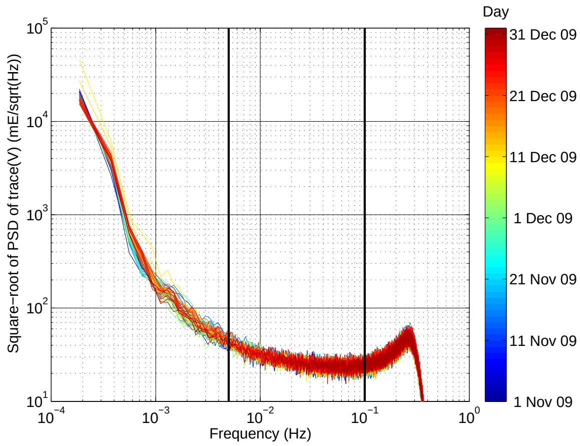

Figure 15: Square-roots of the PSDs of the gravity gradient trace computed for each day of November and December 2009. Top panel: Square-roots of the PSDs are computed using the ICM of the baseline method from October 2009 (old implementation in the ground processing). Bottom panel: Square-roots of the PSDs are computed based on the linear interpolation of the ICMs of the baseline method from October 2009 and January 2010 (current implementation in the ground processing). Vertical thick black lines indicate the measurement band 5–100 mHz.

7.3 Performance of the calibration methods

In this section, we compare the performance of the calibration methods indicated in Fig. 14, i.e. (a) the baseline method (blue circles), the method presented in this paper based on (b) shaking data (green diamonds) as well as on (c) nominal data (black dots), and (d) using the linear trend estimated from results for nominal data (red lines). As discussed in Sect. 7.2, we linearly interpolate the ICMs of the methods using shaking data between the nearest shakings in the past and future in order to account for the drifts in the calibration parameters. In case of the presented method using nominal data (black dots), we apply each set of calibration parameters to the same data of two days, from which that set was estimated. Finally, using the linear trend (red lines) for the calibration means using ICMs that change linearly with time according to Fig. 14.

The comparison is based on the gravity gradient trace as well as differences of calibrated gravity gradients to gravity gradients computed along the GOCE orbits from the ITG-Grace2010s model, the inertial attitude quaternions in the EGG_NOM_1b product, the reduced-dynamic orbits and the quaternions relating the Earth-fixed reference frame to the inertial reference frame in the SST_PSO_2 product [European GOCE Gravity Consortium(2008), Visser(2009)]. ITG-Grace2010s is a satellite-only model calculated from 7 years of GRACE data up to spherical harmonic degree and order 180. We perform the comparison for nominal data from November to December 2009.

The gradiometer is designed to have the lowest noise level in the measurement band 5–100 mHz. Below the measurement band, the noise level strongly increases as the frequency decreases. These features are clearly visible in the gravity gradient trace shown in Fig. 16. The GRACE mission is designed to perform best for low to middle frequencies [Tapley et al.(2004)]. Therefore, we expect that the gravity gradients computed from the ITG-Grace2010s model can serve as a reference up to some frequency within the measurement band of the gradiometer. We show the differences ΔV_{xx}, ΔV_{yy} and ΔV_{zz} of calibrated gravity gradients with respect to the ITG-Grace2010s model in Fig. 16. For ΔV_{xx} and ΔV_{zz}, we observe a small peak between 25–40 mHz. Since the peaks coincide with the frequency corresponding to 180 cycles-per-revolution, we assume that they reflect noise in the higher spherical harmonic degrees of the ITG-Grace2010s model.

The comparison in Fig. 16 shows that all considered calibration methods perform well within the measurement band. We can see this in particular, when we compare calibrated and uncalibrated gravity gradients. Larger differences between the considered calibration methods are only visible below the measurement band. Judging on the gravity gradient trace, ΔV_{xx} and ΔV_{zz}, we obtain the following ranking of the methods: the baseline method (solid blue line) performs best, the method using nominal data (dashed black line) performs worst, and the methods using shaking data (solid green line) and linearly approximating the results from nominal data (dashed red line) are in between. For ΔV_{yy}, however, we observe that the method linearly approximating the results from nominal data (dashed red line) performs better than the other methods between 2–9 mHz. We analyze in Sect. 7.4 which elements of the ICMs could be responsible for this.

7.4 Sensitivity of gravity gradients to biases in the elements of the ICMs

In Sect. 7.3, we observed that the method linearly approximating the results from nominal data performs better than the baseline method for V_{yy}. This indicates that we can use the method presented in this paper to find corrections for the ICMs of the baseline method. Fig. 15 provides no indication that drifts in the calibration parameters are not properly taken into account by the linear interpolation of the ICMs. Thus, we consider only corrections that are constant over time, i.e. biases in the ICM elements. This means, for example, that the correction for the ICMs in October 2009 is the same as in January 2010.

In order to identify which ICM elements may need to be corrected, we analyze the sensitivity of the gravity gradients to biases in the individual ICM elements. As benchmark, we use the standard deviations in the measurement band 5–100 mHz of differences ΔV_{xx}, ΔV_{yy} and ΔV_{zz} of calibrated gravity gradients with respect to the ITG-Grace2010s model. The standard deviations $\sigma_{xx}^{(\mathrm{ref})} = 3.6$ mE for ΔV_{xx}, $\sigma_{yy}^{(\mathrm{ref})} = 3.2$ mE for ΔV_{yy} and $\sigma_{zz}^{(\mathrm{ref})} = 6.5$ mE for ΔV_{zz} obtained by using the ICMs of the baseline method serve as the reference.

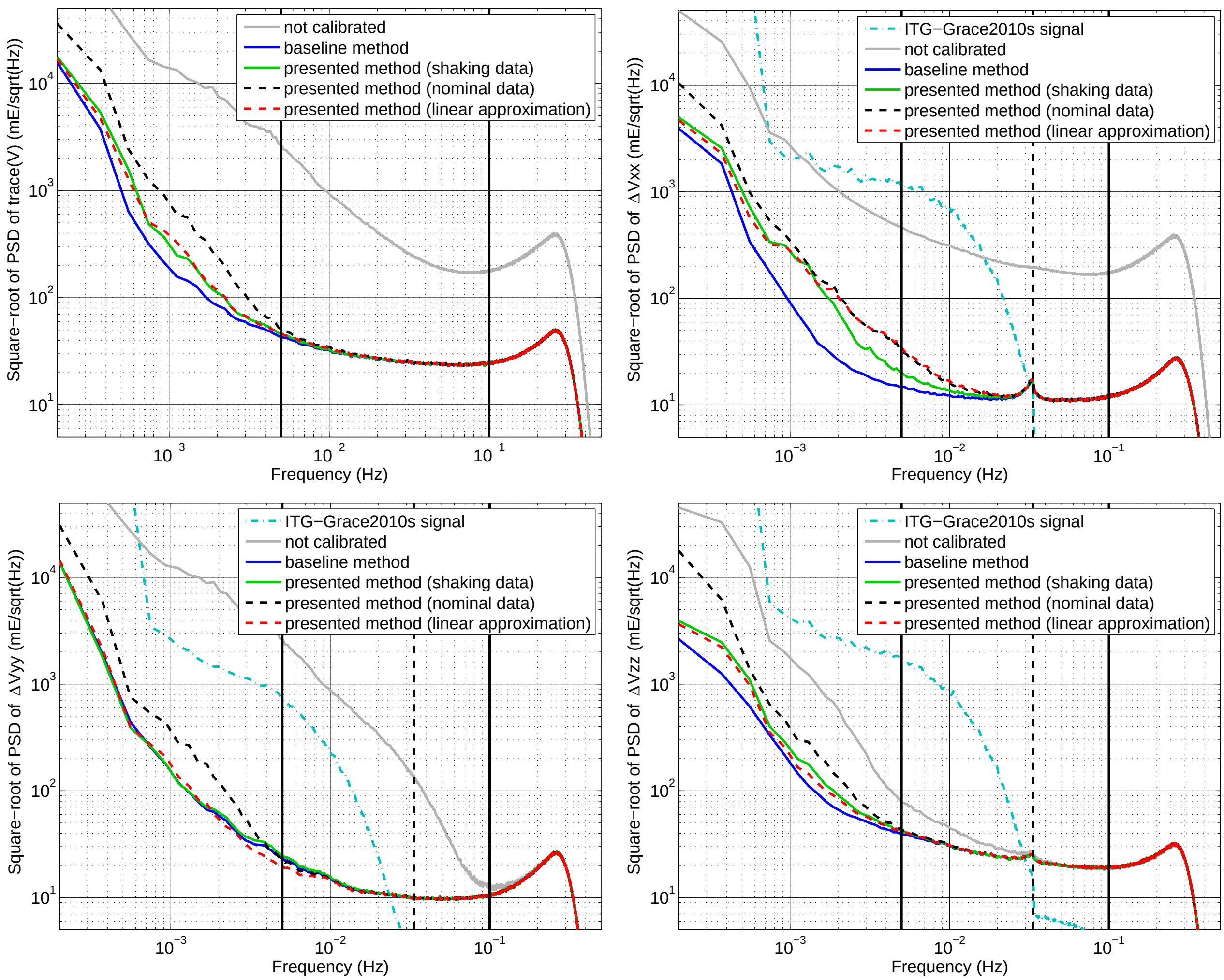

Figure 16: Square-roots of the PSDs for November to December 2009: gravity gradient trace (top left panel), differences of gravity gradients V_{xx} (top right panel), V_{yy} (bottom left panel) and V_{zz} (bottom right panel) with respect to the ITG-Grace2010s model. For reference, the signal of the ITG-Grace2010s model is plotted in dashed-dotted cyan lines. Vertical thick black lines indicate the measurement band 5–100 mHz. The vertical dashed black line indicates the frequency corresponding to 180 cycles-per-revolution.

Table 3: Change of the standard deviation of the gravity gradients in the measurement band 5–100 mHz due to random biases in ICM elements. The random biases are normal distributed with zero mean and standard variation 10^{-4}. Not listed changes of standard deviations are equal to 0.0% when rounded to one decimal place.

V_{xx}, ICM $\boldsymbol{M}_{14}$, row 4					
$(\boldsymbol{M}_1 - \boldsymbol{M}_4)/2$			$(\boldsymbol{M}_1 + \boldsymbol{M}_4)/2$		
+0.2%	+21.9%	+4.1%	0.0%	0.0%	+0.1%
V_{yy}, ICM $\boldsymbol{M}_{25}$, row 5					
$(\boldsymbol{M}_2 - \boldsymbol{M}_5)/2$			$(\boldsymbol{M}_2 + \boldsymbol{M}_5)/2$		
+0.2%	+27.0%	+4.4%	0.0%	0.0%	+0.3%
V_{zz}, ICM $\boldsymbol{M}_{36}$, row 6					
$(\boldsymbol{M}_3 - \boldsymbol{M}_6)/2$			$(\boldsymbol{M}_3 + \boldsymbol{M}_6)/2$		
+0.1%	+7.3%	+1.0%	0.0%	+0.1%	0.0%

Then, we perform the following Monte Carlo simulation. We add a random bias to a single ICM element, where the random bias is normal distributed with zero mean and standard deviation 10^{-4}. We use the biased ICMs to compute calibrated gravity gradients. The standard deviations $\sigma_{xx}^{(\text{bias})}$, $\sigma_{yy}^{(\text{bias})}$ and $\sigma_{zz}^{(\text{bias})}$ are computed in the same way as $\sigma_{xx}^{(\text{ref})}$, $\sigma_{yy}^{(\text{ref})}$ and $\sigma_{zz}^{(\text{ref})}$, except that we use the gravity gradients computed using the biased ICMs. In this way, we generate 100 samples of $\sigma_{xx}^{(\text{bias})}$, $\sigma_{yy}^{(\text{bias})}$ and $\sigma_{zz}^{(\text{bias})}$, from which we first compute the mean variances and, then, the standard deviations $\bar{\sigma}_{xx}^{(\text{bias})}$, $\bar{\sigma}_{yy}^{(\text{bias})}$ and $\bar{\sigma}_{zz}^{(\text{bias})}$ as the square-roots of the mean variances. Table 3 lists the change of these standard deviations with respect to the reference standard deviations.

Table 3 shows that the gravity gradients V_{xx}, V_{yy} and V_{zz} are most sensitive to ICM elements that are used to calibrate the accelerations $a_{d,14,x}$, $a_{d,25,y}$ and $a_{d,36,z}$, respectively. The gravity gradients are computed by

$$V_{xx} = -\frac{2}{L_x} a_{d,14,x} - \omega_y^2 - \omega_z^2, \tag{146}$$

$$V_{yy} = -\frac{2}{L_y} a_{d,25,y} - \omega_x^2 - \omega_z^2 \tag{147}$$

and

$$V_{zz} = -\frac{2}{L_z} a_{d,36,z} - \omega_x^2 - \omega_y^2, \tag{148}$$

where ω_x, ω_y and ω_z do not depend on $a_{d,14,x}$, $a_{d,25,y}$ and $a_{d,36,z}$. This means that the gravity gradients have a linear relationship to the DM accelerations $a_{d,14,x}$, $a_{d,25,y}$ and $a_{d,36,z}$. The second and third column of Table 3 show the largest changes. According to Eq. (41), these columns correspond to calibration parameters that describe the mapping of uncalibrated CM accelerations $a_{c,ij,y}$ and $a_{c,ij,z}$ onto calibrated DM accelerations $\boldsymbol{a}_{d,ij}$ and, thus, on the gravity gradients. These calibration parameters cause larger changes because the CM accelerations $a_{c,ij,y}$ and $a_{c,ij,z}$ reflect the linear accelerations of the satellite COM in the cross-track and radial directions, respectively, which are the largest signals contained in the accelerations $\boldsymbol{a}_i$. The CM accelerations $a_{c,ij,x}$ contain a much smaller signal since the drag-free system compensates the linear accelerations in along-track direction acting on the satellite COM. This is reflected by the lower changes in the first column of Table 3.

7.5 Effect of bias correction

Table 3 shows that the gravity gradient V_{yy} is most sensitive to a bias in the element in row 5 and column 2 of the ICM $\boldsymbol{M}_{25}$. According to Eqs. (42) and (44), this particular ICM element is the differential scale factor $\Delta s_{25,y}$. In the bottom panel of Fig. 14, we observe a bias between the results from shaking data and nominal data for $\Delta s_{25,y}$. By taking the median of the differences between the linear interpolation of the baseline method (blue circles in Fig. 14) and the results of our method for nominal data (black dots in Fig. 14), we estimate that the bias is equal to -36×10^{-6}, which appears to be in good agreement with the plots presented in [Rispens and Bouman(2011)].

As discussed in Sect. 7.4, a bias in $\Delta s_{25,y}$ will result in a mapping of CM accelerations onto the gravity gradient V_{yy}. In order to study this effect in more detail, we show maps of the CM acceleration $a_{c,25,y}$ and differences ΔV_{yy} of calibrated gravity gradients with respect to the ITG-Grace2010s model for November and December 2009 in Fig. 17. We filtered all data in the maps to the frequency band 3–50 mHz in order to remove the long and short wavelength noise in the calibrated gravity gradients that would obscure the effect we want to study. Furthermore, we only show the data of ascending orbital tracks because the data is expressed in the GRF, whose cross-track axis has a completely different orientation for ascending and descending orbital tracks.

For ΔV_{yy}, we consider three scenarios. The first is using the ICMs of October 2009, which corresponds to the old implementation in the ground processing. The second is linearly interpolating the ICMs of the baseline method as suggested in Sect. 7.2, which corresponds to the current implementation in the ground processing. The third is linearly interpolating the ICMs of the baseline method and correcting $\Delta s_{25,y}$ for the bias of -36×10^{-6}. The CM accelerations $a_{c,25,y}$ in Fig. 17 show a distinct pattern near the magnetic poles. This pattern is most likely caused by large variations of the cross-track winds in the polar zones [Peterseim et al.(2011), Lühr(2007)]. Under the assumption that the differential scale factor $\Delta s_{25,y}$ needs to be corrected, the same pattern should be visible in ΔV_{yy}. In Fig. 17, we can see clearly that this is the case when using the ICM of October 2009, for which we expect $\Delta s_{25,y}$ to be farthest away from its correct value (cf. Fig. 14). Though the linear interpolation of the ICMs removes the largest part of the pattern in ΔV_{yy}, it is still clearly visible. When we linearly interpolate the ICMs and apply the estimated correction for the bias in $\Delta s_{25,y}$, the pattern is further reduced, which indicates that the bias correction improves the quality of the gravity gradients V_{yy}.

Table 4 provides standard deviations for the maps shown in Fig. 17. In case of using the ICMs of October 2009 (column A), the standard deviations of the magnetic poles are larger than the global ones, in particular the one of the magnetic south pole for ascending orbits. Further, the difference between the standard deviations of ascending and descending orbits is rather large, which might be a result of the difference in the respective flight directions of the satellite. When linearly interpolating the ICMs (column B), the standard deviations of the magnetic poles are almost cut in half while the global standard deviation is reduced by one third. Linearly interpolating the ICMs and correcting $\Delta s_{25,y}$ (column C) further reduces the standard deviations of the magnetic south pole by one half for ascending orbits and one quarter for descending orbits while the global standard deviations and the ones of the magnetic north pole show only very small changes. Even though the standard deviations have reduced a lot, the ones of the magnetic poles for ascending orbits remain slightly above the level of the global standard deviations.

We also studied maps of the gravity gradient trace (not shown) in order to assess the effect independently of the ITG-Grace2010s model, which confirmed the presented results for ΔV_{yy}. Further, it should be mentioned that other authors have noted the pattern near the magnetic poles, too. [Bouman et al.(2010)] write that the pattern does not represent a gravity signal and hypothesize that it is related to drifts in the differential scale factors. They show that linearly interpolating $\Delta s_{25,y}$ between the shaking events in October 2009 and January 2010, while otherwise using the calibration parameters of the shaking event in October 2009, improves the gravity gradient trace. [Bouman et al.(2011)] show that the pattern is present in differences ΔV_{yy} of GOCE gravity gradients to the EIGEN-5C [Foerste et al.(2008)] and EGM2008 [Pavlis et al.(2008)] gravity field models. They, too, write that the pattern does not represent a gravity signal and hypothesize that it is related to drifts in the differential scale factors. Further, they write that the pattern can be largely reduced by adjusting the calibration parameters. Thus, our findings are in good agreement with the work of the above mentioned authors and show that their hypotheses are correct.

7.6 Error analysis for increased drag conditions

The analysis in Sect. 7.1 revealed that the gravity gradients are very sensitive to ICM errors which map CM accelerations onto DM accelerations. In particular, we found that a correction of -36×10^{-6} for the differential scale factor $\Delta s_{25,y}$ improves the performance of the gravity gradients. These results were obtained for data in November and December 2009, when CM accelerations were rather small due to a low solar activity. Fig. 18 shows that the solar activity increased considerable at the beginning of 2011.

The increase in solar activity results in larger CM accelerations. Fig. 19 shows that the CM

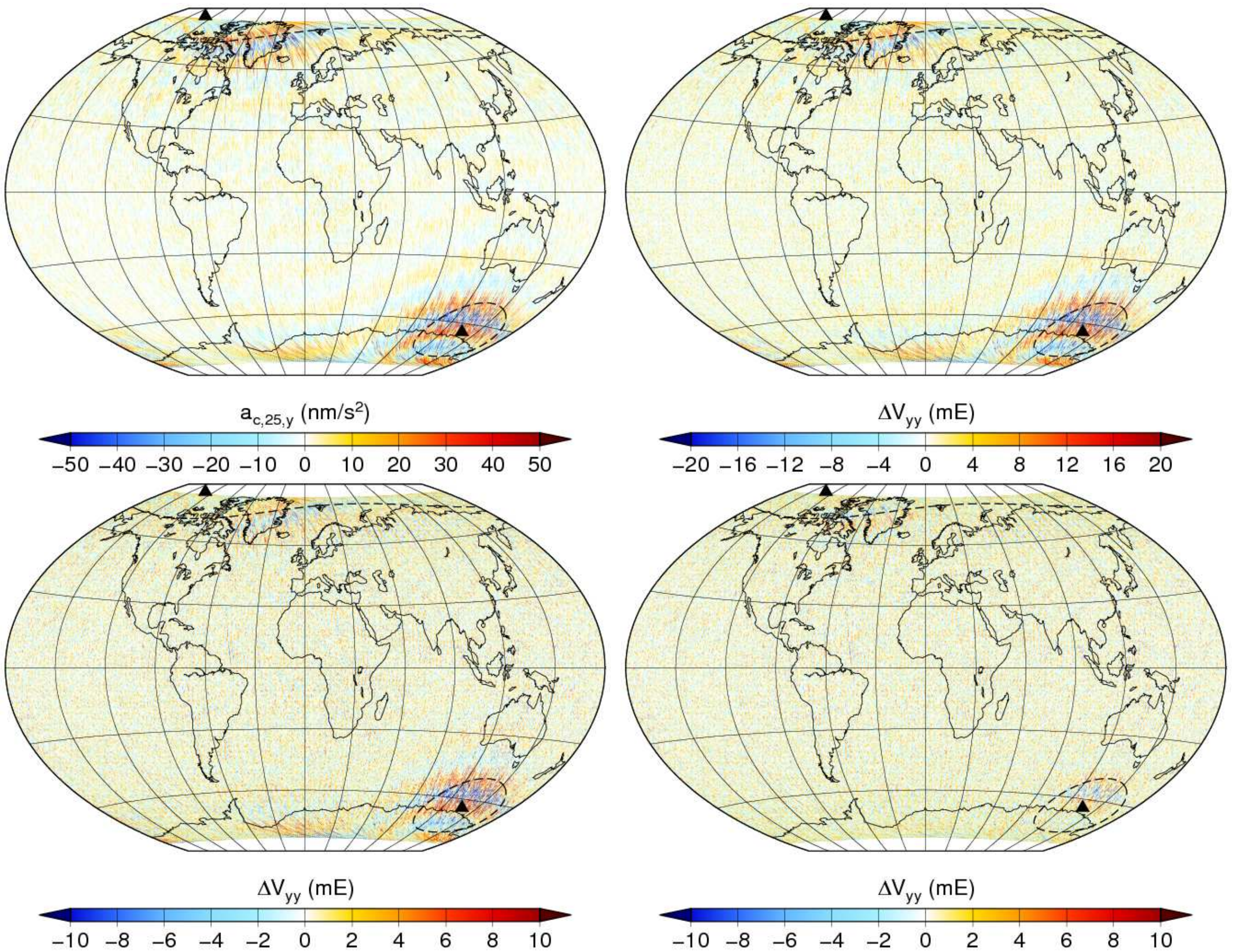

Figure 17: CM accelerations $a_{c,25,y}$ and differences ΔV_{yy} of calibrated gravity gradients to the ITG-Grace2010s model for ascending orbital tracks in November and December 2009, filtered to frequency band 3–50 mHz, and expressed in the GRF: $a_{c,25,y}$ (top left panel), ΔV_{yy} using the same calibration as implemented in the old ground processing (top right panel), ΔV_{yy} using the linearly interpolated ICMs of the baseline method as implemented in the current ground processing (bottom left panel), ΔV_{yy} using the linearly interpolated ICMs of the baseline method that are corrected for the bias -36×10^{-6} in $\Delta s_{25,y}$ (bottom right panel). The locations of the magnetic north and south pole are indicated by black triangles. The dashed black lines mark $15°$ spherical caps centered at the locations of magnetic north and south pole. Table 4 lists associated standard deviations.

Table 4: Standard deviations (mE) of differences ΔV_{yy} of calibrated gravity gradients to the ITG-Grace2010s model in November and December 2009, filtered to frequency band 3–50 mHz, and expressed in the GRF: Column A uses the same calibration as implemented in the old ground processing, column B uses the linearly interpolated ICMs of the baseline method as implemented in the current ground processing, column C uses the linearly interpolated ICMs of the baseline method that are corrected for the bias -36×10^{-6} in $\Delta s_{25,y}$. In addition to the global standard deviations, the standard deviations of the regions near the magnetic north and south pole that are indicated by the dashed black lines in Fig. 17 are listed.

region	tracks	A	B	C
global	all	3.8	2.6	2.4
	ascending	4.2	2.8	2.5
	descending	3.2	2.4	2.3
magnetic north pole	all	4.4	2.6	2.6
	ascending	4.6	2.7	2.8
	descending	4.1	2.5	2.5
magnetic south pole	all	9.4	4.8	2.7
	ascending	11.8	6.1	3.1
	descending	6.0	3.0	2.3

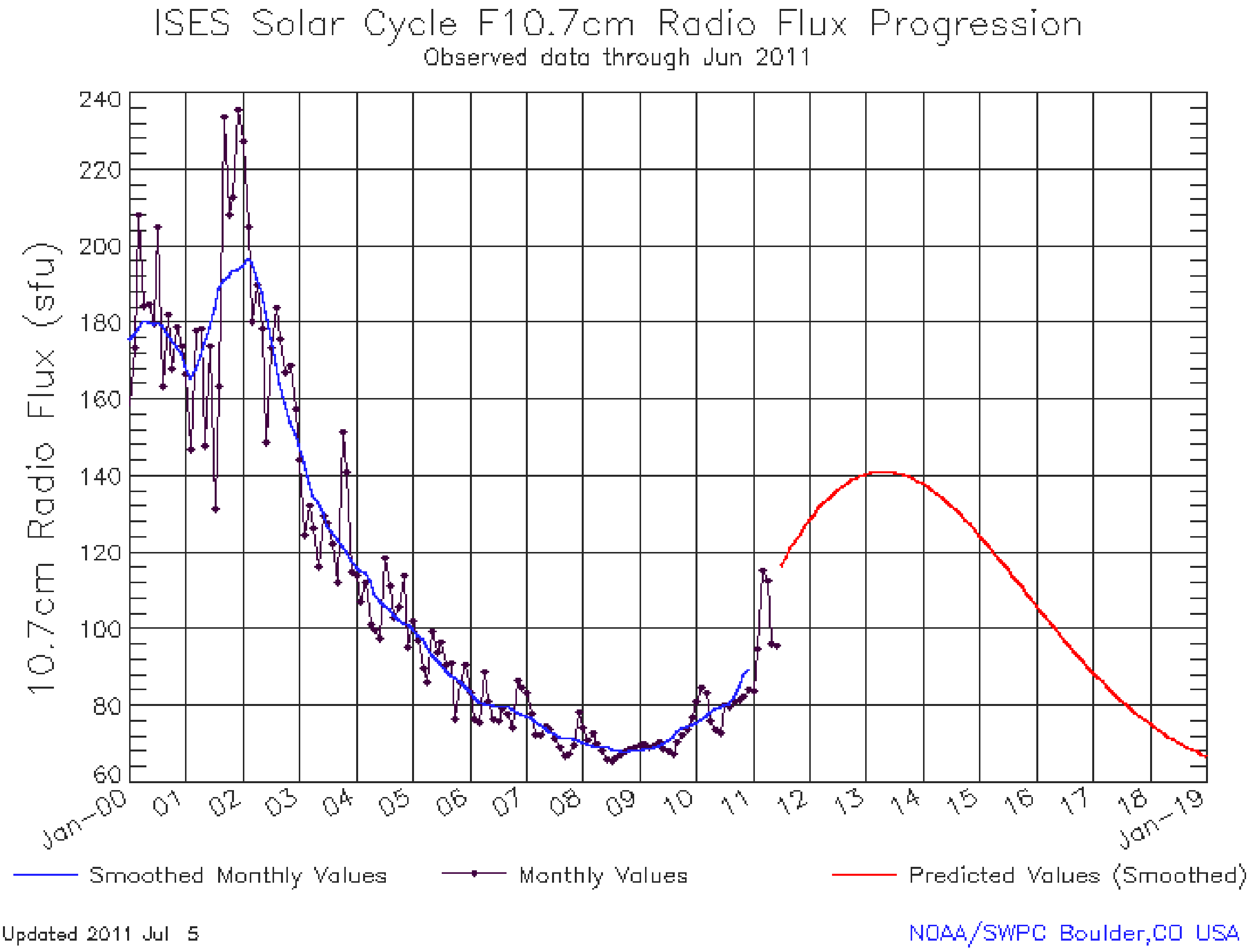

Figure 18: Solar activity, retrieved from `http://www.swpc.noaa.gov/SolarCycle/` on 3 August 2011.

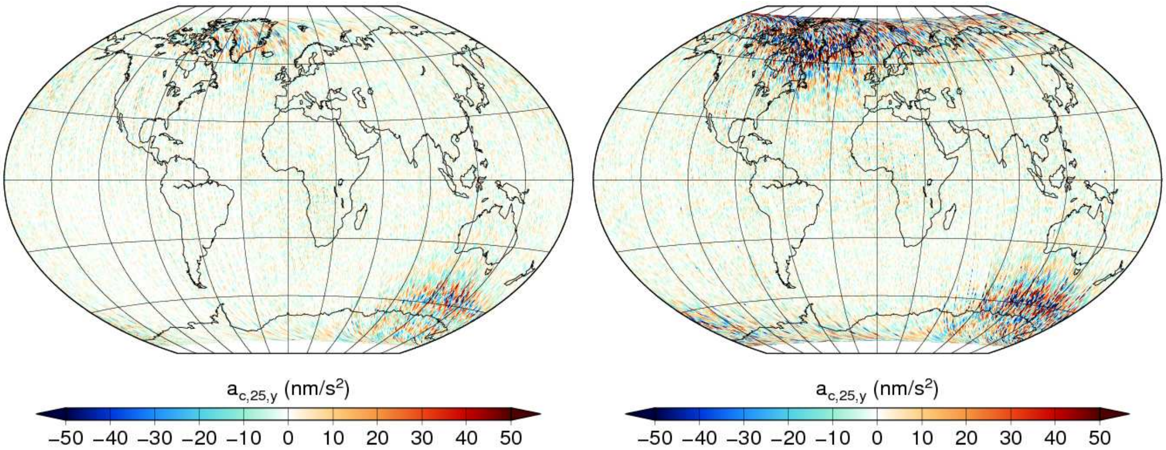

Figure 19: CM accelerations for ascending orbital tracks in November and December 2009 (top left panel) as well as in March and April 2011 (top right panel), both filtered to 5–100 mHz. The increase in the CM accelerations from 2009 to 2011 correlates with the increase in solar activity.

accelerations in March and April 2011 are approximately three times larger than in November and December 2009, when filtered to the measurement band 5–100 mHz. This is clearly visible near the magnetic poles, in particular near the magnetic north pole. This implies that the drag conditions are less quiet for the GOCE satellite, at least near the magnetic poles.

Fig. 20 shows the PSD of the gravity gradient trace in November and December 2009 and in March and April 2011. The latter is 2–3 times worse than the first between 1 and 10 mHz. This is most likely due to the larger CM accelerations because the maps of CM accelerations and the gravity gradient trace in Fig. 19 and Fig. 21, respectively, both show prominent signatures near the magnetic poles, in particular the magnetic north pole. Since the gravity gradients are much more sensitive to ICM errors when CM accelerations are larger, it is likely that more than one calibration parameter needs a correction. For this reason, we investigate the effects of all calibrations parameters on the gravity gradient trace. In case of the differential scale factor $\Delta s_{25,y}$, we saw a clear match of the geographical signature in maps of CM accelerations and differences ΔV_{yy} to the ITG-Grace2010s model(cf. Fig. 17). A similar match was found in the gravity gradient trace (not shown). In the following, we create one map for each ICM element in order to assess the magnitude of the effect of an error in that ICM element and identify its correlations to the gravity gradient trace. If we find that the effect of an error in a ICM element has a large magnitude and correlates with the geographical signature that we see in the gravity gradient trace, then we have identified a candidate for correction. Once all candidates are identified, we try to estimate the corrections to those calibration parameters.

Tables 7.6 – 7.6 list all possible effects of errors in the ICMs. Let us derive the effect of an error ε in row 2 and column 6 of the ICM $\boldsymbol{M}_{25}$. This serves as an example of how to derive the

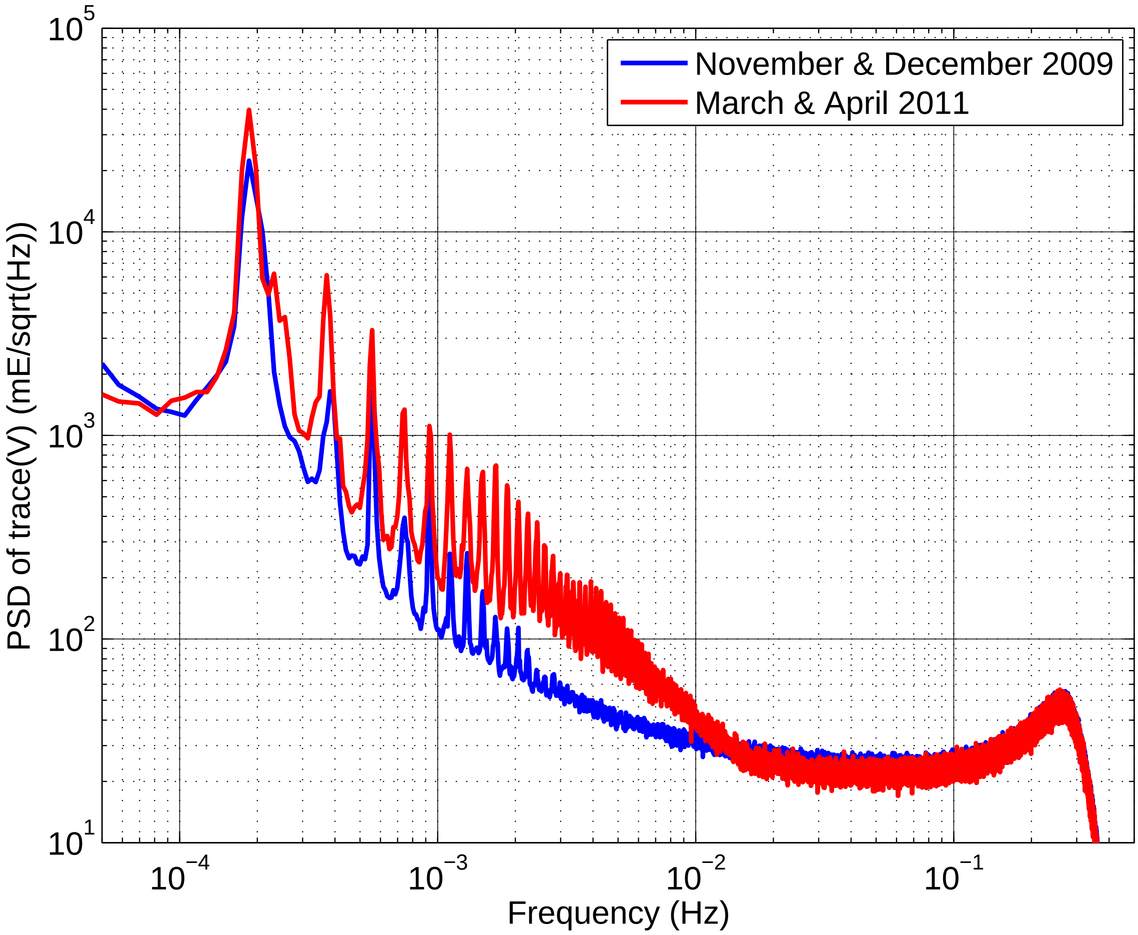

Figure 20: The trace of the gravity gradients worsens from 2009 to 2011 as a result of larger, dynamic CM accelerations.

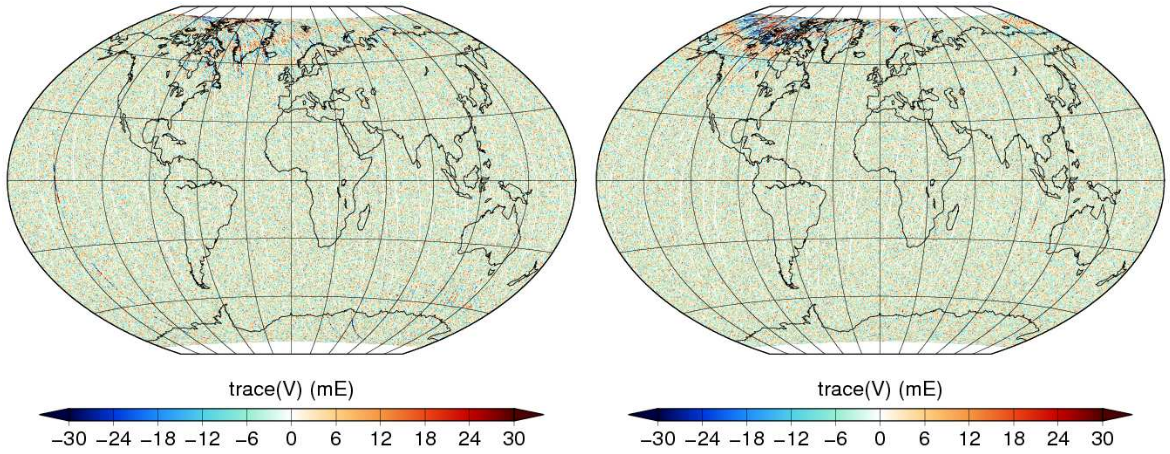

Figure 21: Gravity gradient trace for ascending (left panel) and descending (right panel) orbital tracks in March and April 2011, filtered to 5–100 mHz. Note the prominent signature near the magnetic north pole.

effect of an error in any of the ICM elements. We use the formulas presented in Sect. 3. First of all, the element of the ICM would change, i.e.

$$\boldsymbol{M}_{25}(2,6) \longrightarrow \boldsymbol{M}_{25}(2,6)+\varepsilon, \tag{149}$$

while all other elements of the ICMs remain unchanged. Note that we highlight all changes due to the error ε in red. The error in the ICM element causes an error in the calibrated DM acceleration $a_{d,25,y}$:

$$a_{d,25,y} \longrightarrow a_{d,25,y}+\varepsilon\tilde{a}_{c,25,z} \tag{150}$$

This in turn changes the gravity gradient V_{yy}:

$$V_{yy} \longrightarrow V_{yy}-\frac{2\varepsilon}{L_y}\tilde{a}_{c,25,z} \tag{151}$$

Finally, the effect on the trace is

$$V_{xx}+V_{yy}+V_{zz} \longrightarrow V_{xx}+V_{yy}+V_{zz}-\frac{2\varepsilon}{L_y}\tilde{a}_{c,25,z}. \tag{152}$$

This example shows the effect of an error ε via the DM acceleration terms in Eqs. (33)–(38). Since the propagation of an error ε via the centrifugal acceleration terms in Eqs. (33)–(38) is more complex, we study the effect of an error in row 3 and column 5 of ICM $\boldsymbol{M}_{25}$ as another example. Again, the ICM element changes, i.e.

$$\boldsymbol{M}_{25}(3,5) \longrightarrow \boldsymbol{M}_{25}(3,5)+\varepsilon, \tag{153}$$

while all other ICM elements remain unchanged. This leads to a change in the DM acceleration:

$$a_{d,25,z} \longrightarrow a_{d,25,z}+\varepsilon\tilde{a}_{c,25,y} \tag{154}$$

The effect on the angular velocity needs to take the combination of star sensor and gradiometer data into account. First, the effect on the gradiometer angular velocity is

$$\omega_x^{(\mathrm{GRAD})} \longrightarrow \omega_x^{(\mathrm{GRAD})} + \frac{\varepsilon}{L_y} \int \tilde{a}_{c,25,y}. \tag{155}$$

Then, the effect in the combined angular velocity reads

$$\omega_x \longrightarrow \omega_x + \text{high-pass}(\frac{\varepsilon}{L_y} \int \tilde{a}_{c,25,y}). \tag{156}$$

The highpass-filtering is a linear operation. Therefore, we can move the factor $\frac{\varepsilon}{L_y}$ in front of the filter operation:

$$\omega_x \longrightarrow \omega_x + \frac{\varepsilon}{L_y} \text{high-pass}(\int \tilde{a}_{c,25,y}) \tag{157}$$

Since we consider only small errors, i.e. $\varepsilon << 1$, we can assume that $\varepsilon^2 \approx 0$ and neglect quadratic terms $\mathcal{O}(\varepsilon^2)$ in the centrifugal accelerations:

$$\omega_x^2 \longrightarrow \omega_x^2 + \frac{2\varepsilon}{L_y} \omega_x \text{high-pass}(\int \tilde{a}_{c,25,y}) + \mathcal{O}(\varepsilon^2) \tag{158}$$

Next, we find the error in the gravity gradient

$$V_{yy} \longrightarrow V_{yy} - \frac{2\varepsilon}{L_y} \omega_x \text{high-pass}(\int \tilde{a}_{c,25,y}) + \mathcal{O}(\varepsilon^2). \tag{159}$$

and, finally, in the gravity gradient trace

$$V_{xx} + V_{yy} + V_{zz} \longrightarrow V_{xx} + V_{yy} + V_{zz} - \frac{4\varepsilon}{L_y} \omega_x \text{high-pass}(\int \tilde{a}_{c,25,y}) + \mathcal{O}(\varepsilon^2). \tag{160}$$

In this way, we derived all possible effects on the gravity gradient trace due to errors in the ICMs. These effects are listed in Table 7.6–7.6. We also list the magnitude $\mathcal{O}(\varepsilon)$ that the error must have to be a candidate for correction and whether the effect has a prominent signature near the magnetic poles as another criterion for identifying candidates for correction. This information was determined by manual inspection of maps of all effects (not shown). During the inspection, we found the following:

- The accelerations $\tilde{\boldsymbol{a}}_{c,ij}$ look the same for $ij = 14, 25, 36$ since the linear accelerations $\boldsymbol{d}$ acting on satellite are the dominating signal.
- The accelerations $\tilde{\boldsymbol{a}}_{d,ij}$ are different for $ij = 14, 25, 36$ because uncalibrated DM accelerations contain a fraction of the linear accelerations $\boldsymbol{d}$ depending on the differential parameters in the ICM sub-matrices $\boldsymbol{D}_{ij}$. This means that one element of $\tilde{\boldsymbol{a}}_{d,ij}$ may contain a combination of elements of $\boldsymbol{d}$).

- If the acceleration $\tilde{\boldsymbol{a}}_{d,ij}$ is judged to be a candidate for explaining the signature in the trace, then the fraction of the linear acceleration is the dominating signal in $\tilde{\boldsymbol{a}}_{d,ij}$.

Taking these points into account, only five different signatures remain as candidates for explaining the signature in the trace near the magnetic poles:

- CM accelerations $a_{c,x}$, $a_{c,y}$ and $a_{c,z}$ which affect V_{xx}, V_{yy} and V_{zz}
- Terms $\omega_y\,\text{high-pass}(\int a_{c,y})$ and $\omega_y\,\text{high-pass}(\int a_{c,z})$ which affect V_{xx} and V_{zz}

These five signatures were fitted to the trace in order to check whether a correction of the ICM could remove the peaks from the trace that we see in Fig. 22. This was done one time globally for all data of 27/03/2011 – 04/04/2011, and another time for each pass over a magnetic pole separately. The latter is not very practical, but shows how much the peaks can be removed at maximum. Fig. 22 shows that the also for the latter case it is not possible to remove all peaks.

In this section, we showed that the performance of the gravity gradients may worsen when the non-gravitational accelerations acting on the satellite increase. This is the case for the period March/April 2011 in comparison to the period November/December 2009. We highlighted that an error in an ICM element maps CM or DM accelerations onto the gravity gradients. In Sect. 7.1, we showed that such a mapping was caused by the differential scale factor $\Delta s_{25,y}$, resulting in a prominent geographical signature near the magnetic south pole in November/December 2009. Correcting the differential scale factor $\Delta s_{25,y}$ largely reduced that signature. Applying the same logic to the gravity gradient trace in March/April 2011, we tried to identify the ICM elements that may need to be corrected. For that purpose, we analyzed the geographical signatures caused by an hypothetical error in each individual ICM element. We identified five signatures tat may cause the signature that we see in the gravity gradient trace in Fig. 21. By fitting these signatures to the signature in the gravity gradient trace, we checked whether correcting ICM elements could remove the signature in the trace. Even though the geographical signature in the gravity gradient trace could be reduced in this way, a significant part of the signature remained visible. This means that besides correcting ICM elements, at least one other unidentified problem exists. Further research is required.

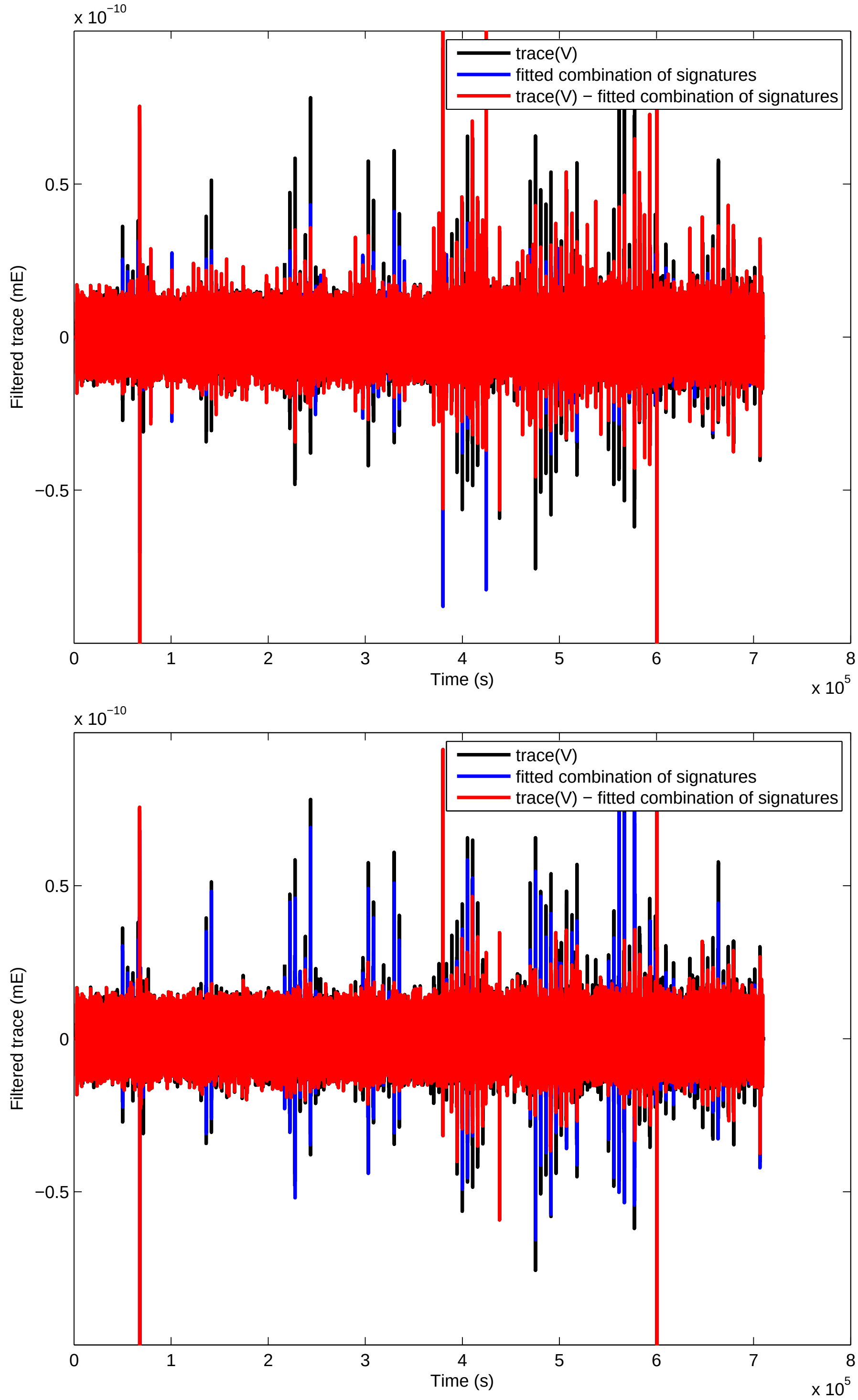

Figure 22: Fit of five candidate signatures to the trace for all data of 27/03/2011 – 04/04/2011 (top panel) and to data near the magnetic poles (bottom panel), both filtered to 5–50 mHz.

affected		ICM		magnitude	signature	
gradients	via	sub-matrix	effect	$\mathcal{O}(\varepsilon)$	mag. poles	candidate
V_{xx}	$-\frac{2}{L_x}a_{d,14,x}$	$\boldsymbol{D}$	$-\frac{2\varepsilon}{L_x}\tilde{a}_{c,14,x}$	10^{-3}	yes	yes
V_{xx}	$-\frac{2}{L_x}a_{d,14,x}$	$\boldsymbol{D}$	$-\frac{2\varepsilon}{L_x}\tilde{a}_{c,14,y}$	10^{-4}	yes	yes
V_{xx}	$-\frac{2}{L_x}a_{d,14,x}$	$\boldsymbol{D}$	$-\frac{2\varepsilon}{L_x}\tilde{a}_{c,14,z}$	10^{-4}	yes	yes
V_{xx}	$-\frac{2}{L_x}a_{d,14,x}$	$\boldsymbol{C}$	$-\frac{2\varepsilon}{L_x}\tilde{a}_{d,14,x}$	10^{-1}	no	no
V_{xx}	$-\frac{2}{L_x}a_{d,14,x}$	$\boldsymbol{C}$	$-\frac{2\varepsilon}{L_x}\tilde{a}_{d,14,y}$	10^{-3}	yes	yes
V_{xx}	$-\frac{2}{L_x}a_{d,14,x}$	$\boldsymbol{C}$	$-\frac{2\varepsilon}{L_x}\tilde{a}_{d,14,z}$	10^{-2}	no	no
V_{yy}	$-\frac{2}{L_y}a_{d,25,y}$	$\boldsymbol{D}$	$-\frac{2\varepsilon}{L_y}\tilde{a}_{c,25,x}$	10^{-3}	yes	yes
V_{yy}	$-\frac{2}{L_y}a_{d,25,y}$	$\boldsymbol{D}$	$-\frac{2\varepsilon}{L_y}\tilde{a}_{c,25,y}$	10^{-4}	yes	yes
V_{yy}	$-\frac{2}{L_y}a_{d,25,y}$	$\boldsymbol{D}$	$-\frac{2\varepsilon}{L_y}\tilde{a}_{c,25,z}$	10^{-4}	yes	yes
V_{yy}	$-\frac{2}{L_y}a_{d,25,y}$	$\boldsymbol{C}$	$-\frac{2\varepsilon}{L_y}\tilde{a}_{d,25,x}$	10^{-3}	yes	yes
V_{yy}	$-\frac{2}{L_y}a_{d,25,y}$	$\boldsymbol{C}$	$-\frac{2\varepsilon}{L_y}\tilde{a}_{d,25,y}$	10^{-2}	yes	no
V_{yy}	$-\frac{2}{L_y}a_{d,25,y}$	$\boldsymbol{C}$	$-\frac{2\varepsilon}{L_y}\tilde{a}_{d,25,z}$	10^{-2}	no	no
V_{zz}	$-\frac{2}{L_z}a_{d,36,z}$	$\boldsymbol{D}$	$-\frac{2\varepsilon}{L_z}\tilde{a}_{c,36,x}$	10^{-3}	yes	yes
V_{zz}	$-\frac{2}{L_z}a_{d,36,z}$	$\boldsymbol{D}$	$-\frac{2\varepsilon}{L_z}\tilde{a}_{c,36,y}$	10^{-4}	yes	yes
V_{zz}	$-\frac{2}{L_z}a_{d,36,z}$	$\boldsymbol{D}$	$-\frac{2\varepsilon}{L_z}\tilde{a}_{c,36,z}$	10^{-4}	yes	yes
V_{zz}	$-\frac{2}{L_z}a_{d,36,z}$	$\boldsymbol{C}$	$-\frac{2\varepsilon}{L_z}\tilde{a}_{d,36,x}$	10^{-1}	no	no
V_{zz}	$-\frac{2}{L_z}a_{d,36,z}$	$\boldsymbol{C}$	$-\frac{2\varepsilon}{L_z}\tilde{a}_{d,36,y}$	10^{-3}	no	no
V_{zz}	$-\frac{2}{L_z}a_{d,36,z}$	$\boldsymbol{C}$	$-\frac{2\varepsilon}{L_z}\tilde{a}_{d,36,z}$	10^{-2}	no	no

affected gradients	via	ICM sub-matrix	effect	magnitude $\mathcal{O}(\varepsilon)$	signature mag. poles	candidate
V_{yy}, V_{zz}	$-\omega_x^2$	$\boldsymbol{D}$	$-\frac{2\varepsilon}{L_y}\omega_x$high-pass$(\int \tilde{a}_{c,25,x})$	10^1	no	no
V_{yy}, V_{zz}	$-\omega_x^2$	$\boldsymbol{D}$	$-\frac{2\varepsilon}{L_y}\omega_x$high-pass$(\int \tilde{a}_{c,25,y})$	10^{-1}	yes	no
V_{yy}, V_{zz}	$-\omega_x^2$	$\boldsymbol{D}$	$-\frac{2\varepsilon}{L_y}\omega_x$high-pass$(\int \tilde{a}_{c,25,z})$	10^{-1}	no	no
V_{yy}, V_{zz}	$-\omega_x^2$	$\boldsymbol{C}$	$-\frac{2\varepsilon}{L_y}\omega_x$high-pass$(\int \tilde{a}_{d,25,x})$	10^0	no	no
V_{yy}, V_{zz}	$-\omega_x^2$	$\boldsymbol{C}$	$-\frac{2\varepsilon}{L_y}\omega_x$high-pass$(\int \tilde{a}_{d,25,y})$	10^1	no	no
V_{yy}, V_{zz}	$-\omega_x^2$	$\boldsymbol{C}$	$-\frac{2\varepsilon}{L_y}\omega_x$high-pass$(\int \tilde{a}_{d,25,z})$	10^0	no	no
V_{yy}, V_{zz}	$-\omega_x^2$	$\boldsymbol{D}$	$-\frac{2\varepsilon}{L_z}\omega_x$high-pass$(\int \tilde{a}_{c,36,x})$	10^1	no	no
V_{yy}, V_{zz}	$-\omega_x^2$	$\boldsymbol{D}$	$-\frac{2\varepsilon}{L_z}\omega_x$high-pass$(\int \tilde{a}_{c,36,y})$	10^{-1}	yes	no
V_{yy}, V_{zz}	$-\omega_x^2$	$\boldsymbol{D}$	$-\frac{2\varepsilon}{L_z}\omega_x$high-pass$(\int \tilde{a}_{c,36,z})$	10^0	no	no
V_{yy}, V_{zz}	$-\omega_x^2$	$\boldsymbol{C}$	$-\frac{2\varepsilon}{L_z}\omega_x$high-pass$(\int \tilde{a}_{d,36,x})$	10^1	no	no
V_{yy}, V_{zz}	$-\omega_x^2$	$\boldsymbol{C}$	$-\frac{2\varepsilon}{L_z}\omega_x$high-pass$(\int \tilde{a}_{d,36,y})$	10^1	no	no
V_{yy}, V_{zz}	$-\omega_x^2$	$\boldsymbol{C}$	$-\frac{2\varepsilon}{L_z}\omega_x$high-pass$(\int \tilde{a}_{d,36,z})$	10^1	no	no

affected gradients	via	ICM sub-matrix	effect	magnitude $\mathcal{O}(\varepsilon)$	pattern mag. poles	candidate
V_{xx}, V_{zz}	$-\omega_y^2$	$\boldsymbol{D}$	$-\frac{2\varepsilon}{L_x}\omega_y\text{high-pass}(\int \tilde{a}_{c,14,x})$	10^{-1}	yes	no
V_{xx}, V_{zz}	$-\omega_y^2$	$\boldsymbol{D}$	$-\frac{2\varepsilon}{L_x}\omega_y\text{high-pass}(\int \tilde{a}_{c,14,y})$	10^{-3}	yes	yes
V_{xx}, V_{zz}	$-\omega_y^2$	$\boldsymbol{D}$	$-\frac{2\varepsilon}{L_x}\omega_y\text{high-pass}(\int \tilde{a}_{c,14,z})$	10^{-2}	yes	no
V_{xx}, V_{zz}	$-\omega_y^2$	$\boldsymbol{C}$	$-\frac{2\varepsilon}{L_x}\omega_y\text{high-pass}(\int \tilde{a}_{d,14,x})$	10^{0}	no	no
V_{xx}, V_{zz}	$-\omega_y^2$	$\boldsymbol{C}$	$-\frac{2\varepsilon}{L_x}\omega_y\text{high-pass}(\int \tilde{a}_{d,14,y})$	10^{-1}	yes	no
V_{xx}, V_{zz}	$-\omega_y^2$	$\boldsymbol{C}$	$-\frac{2\varepsilon}{L_x}\omega_y\text{high-pass}(\int \tilde{a}_{d,14,z})$	10^{0}	no	no
V_{xx}, V_{zz}	$-\omega_y^2$	$\boldsymbol{D}$	$-\frac{2\varepsilon}{L_z}\omega_y\text{high-pass}(\int \tilde{a}_{c,36,x})$	10^{-1}	yes	no
V_{xx}, V_{zz}	$-\omega_y^2$	$\boldsymbol{D}$	$-\frac{2\varepsilon}{L_z}\omega_y\text{high-pass}(\int \tilde{a}_{c,36,y})$	10^{-3}	yes	yes
V_{xx}, V_{zz}	$-\omega_y^2$	$\boldsymbol{D}$	$-\frac{2\varepsilon}{L_z}\omega_y\text{high-pass}(\int \tilde{a}_{c,36,z})$	10^{-2}	yes	no
V_{xx}, V_{zz}	$-\omega_y^2$	$\boldsymbol{C}$	$-\frac{2\varepsilon}{L_z}\omega_y\text{high-pass}(\int \tilde{a}_{d,36,x})$	10^{0}	no	no
V_{xx}, V_{zz}	$-\omega_y^2$	$\boldsymbol{C}$	$-\frac{2\varepsilon}{L_z}\omega_y\text{high-pass}(\int \tilde{a}_{d,36,y})$	10^{0}	no	no
V_{xx}, V_{zz}	$-\omega_y^2$	$\boldsymbol{C}$	$-\frac{2\varepsilon}{L_z}\omega_y\text{high-pass}(\int \tilde{a}_{d,36,z})$	10^{0}	no	no

affected gradients	via	ICM sub-matrix	effect	magnitude $\mathcal{O}(\varepsilon)$	pattern mag. poles	candidate
V_{xx}, V_{yy}	$-\omega_z^2$	$\boldsymbol{D}$	$-\frac{2\varepsilon}{L_x}\omega_z$high-pass$(\int \tilde{a}_{c,14,x})$	10^1	yes	no
V_{xx}, V_{yy}	$-\omega_z^2$	$\boldsymbol{D}$	$-\frac{2\varepsilon}{L_x}\omega_z$high-pass$(\int \tilde{a}_{c,14,y})$	10^{-1}	yes	no
V_{xx}, V_{yy}	$-\omega_z^2$	$\boldsymbol{D}$	$-\frac{2\varepsilon}{L_x}\omega_z$high-pass$(\int \tilde{a}_{c,14,z})$	10^{-1}	yes	no
V_{xx}, V_{yy}	$-\omega_z^2$	$\boldsymbol{C}$	$-\frac{2\varepsilon}{L_x}\omega_z$high-pass$(\int \tilde{a}_{d,14,x})$	10^1	no	no
V_{xx}, V_{yy}	$-\omega_z^2$	$\boldsymbol{C}$	$-\frac{2\varepsilon}{L_x}\omega_z$high-pass$(\int \tilde{a}_{d,14,y})$	10^0	yes	no
V_{xx}, V_{yy}	$-\omega_z^2$	$\boldsymbol{C}$	$-\frac{2\varepsilon}{L_x}\omega_z$high-pass$(\int \tilde{a}_{d,14,z})$	10^1	no	no
V_{xx}, V_{yy}	$-\omega_z^2$	$\boldsymbol{D}$	$-\frac{2\varepsilon}{L_y}\omega_z$high-pass$(\int \tilde{a}_{c,25,x})$	10^1	yes	no
V_{xx}, V_{yy}	$-\omega_z^2$	$\boldsymbol{D}$	$-\frac{2\varepsilon}{L_y}\omega_z$high-pass$(\int \tilde{a}_{c,25,y})$	10^{-1}	yes	no
V_{xx}, V_{yy}	$-\omega_z^2$	$\boldsymbol{D}$	$-\frac{2\varepsilon}{L_y}\omega_z$high-pass$(\int \tilde{a}_{c,25,z})$	10^{-1}	yes	no
V_{xx}, V_{yy}	$-\omega_z^2$	$\boldsymbol{C}$	$-\frac{2\varepsilon}{L_y}\omega_z$high-pass$(\int \tilde{a}_{d,25,x})$	10^0	yes	no
V_{xx}, V_{yy}	$-\omega_z^2$	$\boldsymbol{C}$	$-\frac{2\varepsilon}{L_y}\omega_z$high-pass$(\int \tilde{a}_{d,25,y})$	10^0	yes	no
V_{xx}, V_{yy}	$-\omega_z^2$	$\boldsymbol{C}$	$-\frac{2\varepsilon}{L_y}\omega_z$high-pass$(\int \tilde{a}_{d,25,z})$	10^0	yes	no

8 Gradiometer level 1b processing

The processing scheme implemented in the GOCE payload data ground segment (PDGS) was designed pre-launch based on performance studies and simulations. The analysis of GOCE data showed that the actual performance of the gradiometer differs in some points from the one assumed pre-launch: The noise above 10 mHz is larger than expected while it is much lower than expected bellow 10 mHz. For this reason, the gradiometer processing scheme was revisited. The investigations showed that several steps in the processing could be improved, which lead to the upgrade of the gradiometer processing in the GOCE PDGS. In Sect. 8.1, we compare the old and the upgraded gradiometer processing. Then, we demonstrate the impact of the upgraded processing steps in Sect. 8.2.

8.1 Comparison of old and upgraded gradiometer processing

The gradiometer level 1b processing performs the computation of gravity gradients from accelerometer and star sensor data. We described the mathematical background of the gradiometer processing in Sect. 3.1. The main steps are

- the computation of the CM and DM accelerations,
- the calibration of the CM and DM accelerations,
- the computation of angular accelerations from calibrated DM accelerations,
- the rotation of star sensor data from the SSRFs to the GRF,
- the reconstruction of the angular rate and attitude of the satellite, and
- the computation of gravity gradients.

Fig. 23 provides an overview over the old and new processing scheme. Four processing steps are either upgraded or added in the new processing. These are the combination of star sensor data, the calibration of CM and DM accelerations, the reconstruction of the angular rate, and the reconstruction of the attitude. The latter two are performed in one step in the old processing while in the new processing they are performed in two separate steps. In the following, we discuss the differences in these processing steps and provide the mathematical background where needed.

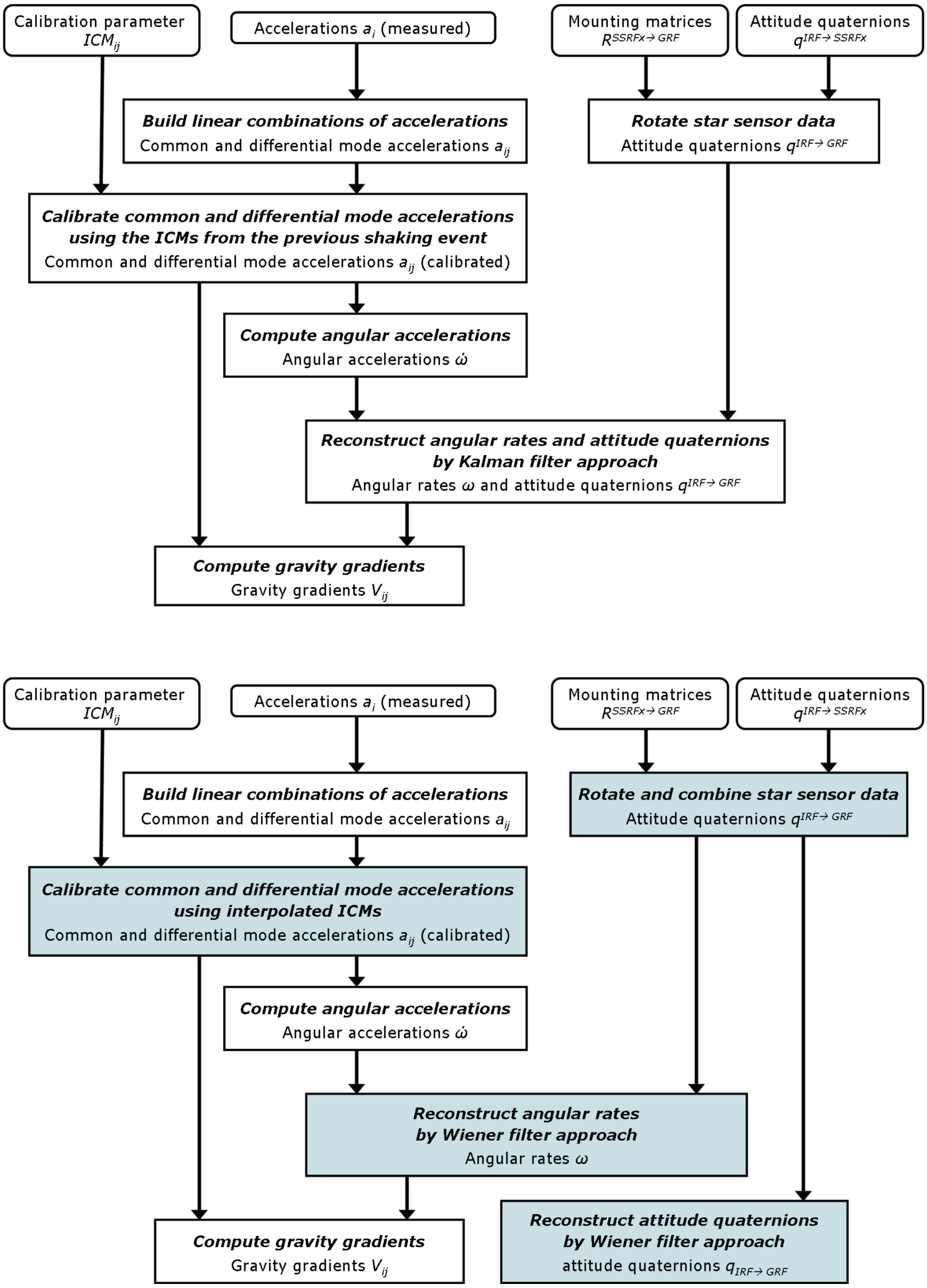

Figure 23: Overview over the old (top panel) and new (bottom panel) GOCE gradiometer level 1b processing. Upgraded processing steps are highlighted in blue.

8.1.1 Combination of star sensor data

In the old processing it was not foreseen to combine star sensors. Thus, this is completely new step in the processing. The combination is performed on the level of attitude quaternions. The mathematical background is provided in Sect. 4.1.

8.1.2 Calibration of accelerometer data

In Sect. 6 we discussed the calibration extensively. We showed that the calibration parameters were subject to linear drifts over time. Since pre-launch simulations suggested that these drifts would be negligible, the calibration in the old processing uses always the ICMs of the previous shaking event. This has the practical advantage that the final gravity gradients are available shortly after the respective gradiometer and star sensor data is down-linked. However, we demonstrated in Sect. 7.1 that the drifts cause a significant degradation of the gravity gradients if they are not taken into account. Therefore, the new gradiometer processing uses a linear interpolation of the ICMs of the previous and next shaking event. This implies that the final gravity gradients are only available up to the previous shaking event.

8.1.3 Reconstruction of the angular rate

The angular rate and attitude reconstruction were performed in one step by a Kalman filter approach in the old processing. In the new processing, the angular rate and attitude reconstruction are preformed in two separate steps. The angular rate reconstruction uses the Wiener filter approach described in [Stummer et al.(2011)]. The principle of the Wiener filter is to combine the angular rates from the gradiometer and star sensor based on their accuracy. As discussed in Sect. 3.1, the accuracy of gradiometer and star sensor angular rates is frequency dependent. In this case, a suitable representation of the accuracy is the PSD, which we can interpret as variance-per-frequency. This means that a value $P(f)$ of the PSD indicates the accuracy at the frequency f. The weights of the Wiener filters are defined in the spectral domain and depend on the PSDs of the angular rates from the gradiometer $P^{(\mathrm{GRAD})}(f)$ and the star sensor $P^{(\mathrm{STR})}(f)$:

$$H^{(\mathrm{STR})}(f) = \frac{P^{(\mathrm{GRAD})}(f)}{P^{(\mathrm{GRAD})}(f) + P^{(\mathrm{STR})}(f)} \tag{161}$$

$$H^{(\mathrm{GRAD})}(f) = \frac{P^{(\mathrm{STR})}(f)}{P^{(\mathrm{GRAD})}(f) + P^{(\mathrm{STR})}(f)} \tag{162}$$

Herein, $H^{(\mathrm{GRAD})}(f)$ and $H^{(\mathrm{STR})}(f)$ are the weights for gradiometer and star sensor angular rates, respectively. The Wiener filters are implemented by symmetric moving-average filters in

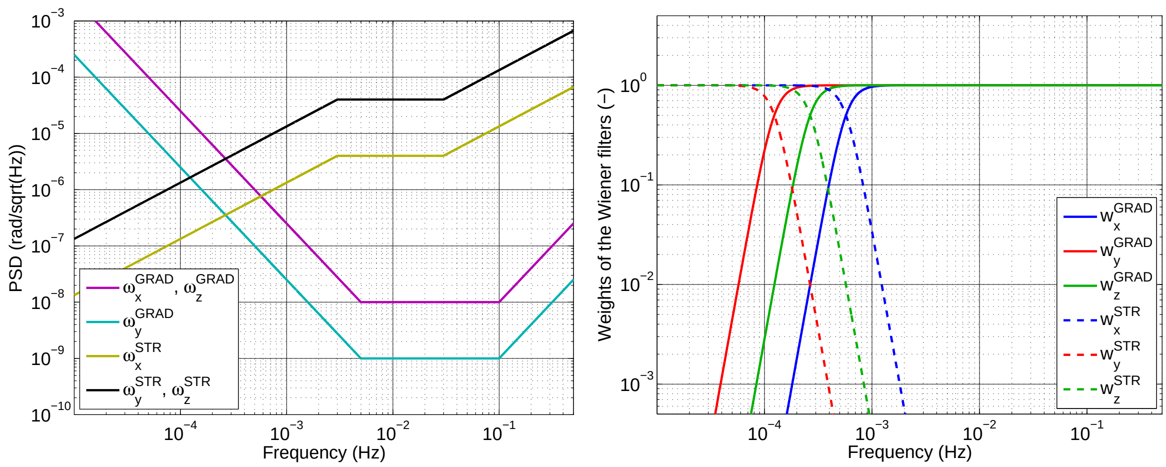

Figure 24: PSD of the noise in the angular rates of the gradiometer and star sensor (left panel) and resulting weights of the Wiener filter (right panel).

the time domain. The coefficients of these filters are obtained from the Wiener weights by the discrete inverse Fourier transform:

$$h_n^{(\mathrm{STR})} = \mathrm{IDFT}(H^{(\mathrm{STR})}(f_k)) \tag{163}$$

$$h_n^{(\mathrm{GRAD})} = \mathrm{IDFT}(H^{(\mathrm{GRAD})}(f_k)) \tag{164}$$

The filter coefficients for the gradiometer and star sensor angular rates are $h_n^{(\mathrm{GRAD})}$ and $h_n^{(\mathrm{STR})}$, respectively, while the indices n and k indicate the discretization. The reconstructed angular rate is obtained by a convolution in the time domain:

$$\omega_n = h_n^{(\mathrm{GRAD})} * \omega_n^{(\mathrm{GRAD})} + h_n^{(\mathrm{STR})} * \omega_n^{(\mathrm{STR})} \tag{165}$$

[Stummer et al.(2011)] suggest to use the following values for $P^{(\mathrm{GRAD})}(f)$ and $P^{(\mathrm{STR})}(f)$:

$$\sqrt{P^{(\mathrm{GRAD})}(f)} = \begin{cases} f^{-2} \text{ behavior} & < 5 \text{ mHz} \\ 1 \times 10^{-8} \text{ for } \omega_x \text{ and } \omega_z,\ \ 1 \times 10^{-9} \text{ for } \omega_x & 5\text{–}100 \text{ mHz} \\ f^{2} \text{ behavior} & > 100 \text{ mHz} \end{cases} \tag{166}$$

$$\sqrt{P^{(\mathrm{STR})}(f)} = \begin{cases} f^{1} \text{ behavior} & < 3 \text{ mHz} \\ 4 \times 10^{-6} \text{ for } \omega_x,\ \ 4 \times 10^{-5} \text{ for } \omega_y \text{ and } \omega_z & 3\text{–}30 \text{ mHz} \\ f^{1} \text{ behavior} & > 30 \text{ mHz} \end{cases} \tag{167}$$

Fig. 24 illustrates that this choice effectively leads to high-pass and low-pass filters for gradiometer and star sensor angular rates, respectively. The length of the Wiener filters is chosen as 8401 epochs.

8.1.4 Reconstruction of the attitude

The attitude is obtained by an integration process of the reconstructed angular rates. In the following, we describe the principle of this integration process. The mean of the angular rates of the previous and current epoch is

$$\bar{\boldsymbol{w}}_k = \frac{\boldsymbol{w}_k + \boldsymbol{w}_{k-1}}{2}. \tag{168}$$

The mean angular rate $\bar{\boldsymbol{w}}_k$ describes the rotation of the satellite from the previous to the current epoch. Thus, we can obtain the attitude of the current epoch by rotating the attitude of the previous epoch about $\bar{\boldsymbol{w}}_k$. This rotation can be written in terms of quaternions as

$$\boldsymbol{q}_k^{(\mathrm{INT})} = \boldsymbol{q}_{k-1}^{(\mathrm{INT})} \begin{bmatrix} \cos(0.5\,\phi_k) \\ \sin(0.5\,\phi)\boldsymbol{e}_k \end{bmatrix}, \tag{169}$$

where

$$\phi = ||\bar{\boldsymbol{w}}_k|| \tag{170}$$

is the rotation angle and

$$\boldsymbol{e}_k = \frac{\bar{\boldsymbol{w}}_k}{||\bar{\boldsymbol{w}}_k||} \tag{171}$$

is the rotation axis according to Euler's rotation theorem. Eq. (169) is used to integrate the quaternions. The integration starts at an initial quaternion $\boldsymbol{q}_0^{(\mathrm{INT})}$, which we take from the attitude quaternions $\boldsymbol{q}_k^{(\mathrm{STR})}$ of the star sensor combination, i.e. $\boldsymbol{q}_0^{(\mathrm{INT})} = \boldsymbol{q}_0^{(\mathrm{STR})}$. Any integration has the property to decrease noise in high frequencies and increase noise in low frequencies. For this reason, we combine the integrated quaternions with the attitude quaternions of the combined star sensors by the convolutions

$$\boldsymbol{q}_n(i) = h_n^{(\mathrm{GRAD})} * \boldsymbol{q}_n^{(\mathrm{INT})}(i) + h_n^{(\mathrm{STR})} * \boldsymbol{q}_n^{(\mathrm{STR})}(i), \quad i = 1,2,3,4 \tag{172}$$

using the same Wiener filters in Eqs. (163) and (164 that we used in the angular rate reconstruction. The index i indicates that the convolution is performed independently for each element of the quaternion while index n represents the epoch.

Since small errors in the reconstructed angular rates accumulate in the integration over time, we restart the integration for each step of the convolution. This means that the integrated quaternions $\boldsymbol{q}_k^{(\mathrm{INT})}$ in Eq. (172) are computed for each epoch n by evaluating Eq. (169) for $k = n - \mathrm{floor}(\frac{L}{2}), \ldots, n + \mathrm{floor}(\frac{L}{2})$ where L denotes the length of the Wiener filter. The initial quaternion is set to $\boldsymbol{q}_{n-\mathrm{floor}(\frac{L}{2})}^{(\mathrm{INT})} = \boldsymbol{q}_{n-\mathrm{floor}(\frac{L}{2})}^{(\mathrm{STR})}$. In this way, we avoid the error accumulation over time.

Table 5: Five cases of gradiometer level 1b processing. Case A represents the old processing while case E represents the new processing.

Case	Angular rate reconstruction	Star sensor combination	Calibration of accelerations	Attitude reconstruction
A	old	old	old	old
B	new	old	old	old
C	new	new	old	old
D	new	new	new	old
E	new	new	new	new

8.2 Impact of upgraded processing steps

We investigate the impact of the upgraded level 1b gradiometer processing step-by-step, beginning with the old processing and ending with the new processing. This means that we investigate five cases: Case A represents the old processing where none of the upgraded steps are used. From case B to E we subsequently replace the old processing steps by the new angular rate reconstruction, the combination of the star sensors' attitude quaternions, the interpolation of the corrected ICMs within the calibration of DM and CM accelerations, and the new attitude reconstruction. Thus, case E represents the new processing. Table 5 provides an overview over these case.

The investigations are based on the same data that we used in Sect. 7, i.e.

- EGG_NOM_1b (EGG_NCD_DS dataset)
  nominal CM and DM accelerations
- STR_VC2_1b, STR_VC3_1b
  star sensor inertial attitude quaternions
- AUX_EGG_DB
  lengths of the gradiometer arms, rotation matrices relating the SSRFs to the GRF
- AUX_ICM_1b
  ICMs

In addition, we correct the differential scale factor $\Delta s_{25,y}$ of the ICMs by -36×10^{-6}, as suggested in Sect. 7.1.

The comparison of case A–E is performed on the level of gravity gradients and gravity field models. This means that we analyze the improvement of GOCE level 1b products as well as GOCE level 2 products. On the level of gravity gradients we investigate the gravity gradient trace as well as the differences to the ITG-Grace2010s model. Thus, we perform two independent checks. However, it should be noted that the gravity gradient trace is invariant with respect to the attitude. Therefore, the improvement due to the upgrade of the attitude reconstruction (case E) is not assessed by analyzing the gravity gradient trace. On the level of gravity field models, we analyze differences of case A–E to the ITG-Grace2010s and EGM2008 models.

8.2.1 Impact on gravity gradients

We analyze the impact of the upgraded processing step-by-step. Fig. 25 shows PSDs of the gravity gradient trace and the differences of GOCE gravity gradients to the ITG-Grace2010s model for case A–E. It should be noted that the gravity gradient trace is invariant with respect to the attitude. Thus, the impact of the upgraded attitude reconstruction cannot be assessed by investigating the gravity gradient trace. When investigating Fig. 25, we see that the upgraded processing affects mainly low frequencies f: $f < 20$ mHz for the trace, $f < 9$ mHz for V_{xx}, $f < 30$ mHz for V_{yy}, $f < 8$ mHz for V_{xz}, and $f < 6$ for V_{zz}. Bellow these frequencies, the angular rate reconstruction (case A vs. B, red vs. blue lines) causes the largest improvement for the gravity gradient trace, V_{xx} and V_{zz}. The interpolation of the ICMs in the calibration of DM and CM accelerations (case C vs. D, cyan vs. magenta lines) causes the largest improvements in V_{yy}. Note that also the gravity gradient trace shows a similar improvement. We discussed the effect of this interpolation in Sect. 7.1. In comparison to the angular rate reconstruction and interpolation of the ICMs, the attitude reconstruction provides a rather small improvement (case E vs. D, green vs. magenta lines). The exception is V_{xz}, for which the attitude reconstruction is clearly the most important processing step. This can be explained by the fact that V_{xz} is very sensitive to the attitude. The combination of star sensor data leads only to small direct improvements. However, it should be noted that the attitude reconstruction benefits from the combination of star sensor data. Therefore, the improvement in V_{xz} may be partly attributed also to the combination of the star sensors.

Fig. 26–30 shows maps of the gravity gradient trace and the the gravity gradient trace and the differences of the gravity gradients V_{xx}, V_{xz}, V_{yy} and V_{zz} to the ITG-Grace2010s model, respectively, for case A–E. In order to enhance the visibility of interesting features, we filtered the data in the time domain to 1–50 mHz bevor creating the map.

The gravity gradient trace in Fig. 26 shows large errors in case of the nominal processing (see 1st row). The analysis in time domain (not shown here) shows that these errors could be caused by systematic errors in star sensor data with an correlation length of a few days. This indicates that these errors might be dependent on the field-of-view of the star sensors. The fact that the errors in the trace might be caused by systematic errors in the star sensor data is supported by the observation that they are largely reduced due to the upgraded angular rate reconstruction

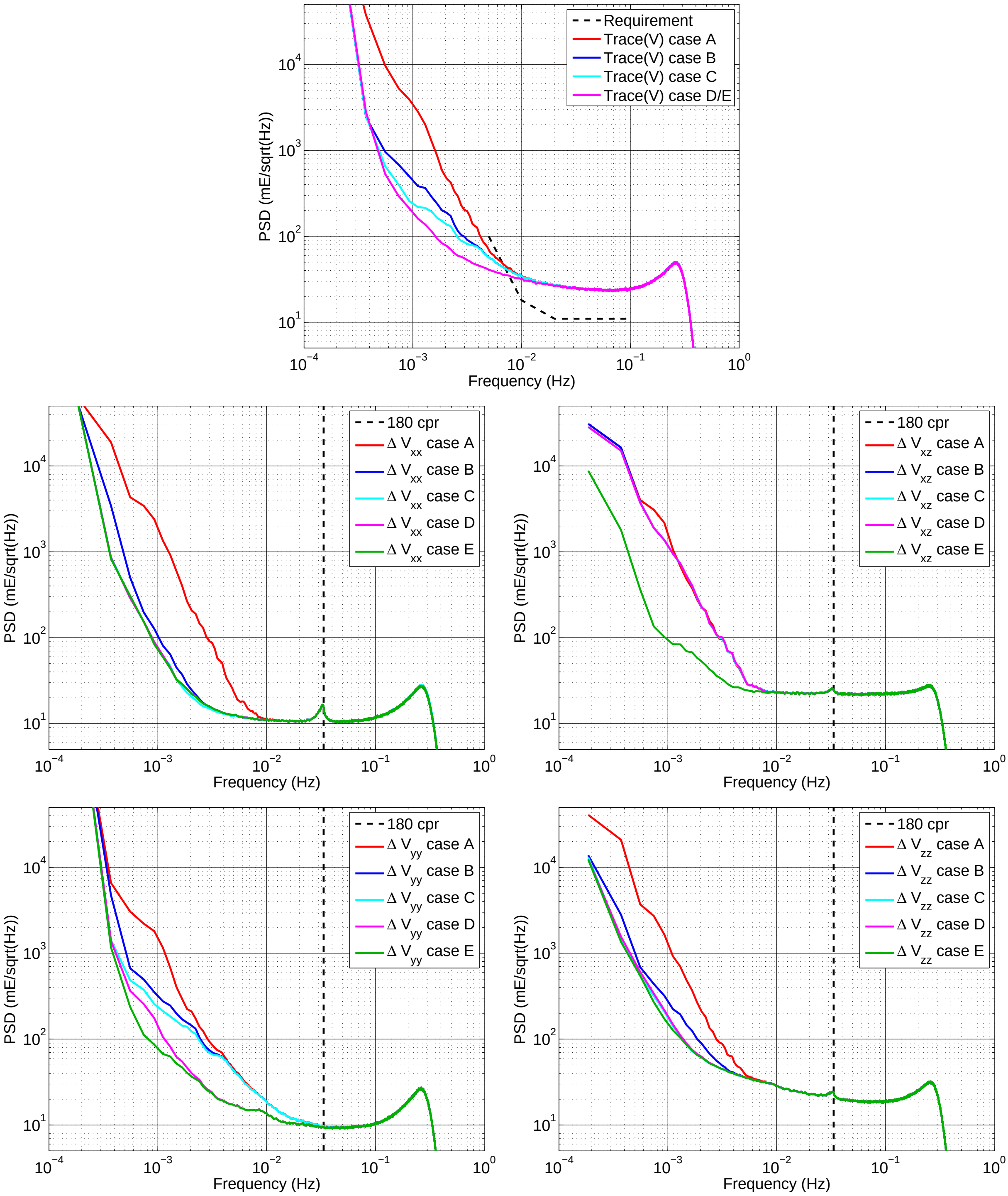

Figure 25: PSDs of the gravity gradient trace and differences of gravity gradients to the ITG-Grace2010s model for case A–E (see Table 5). Note that the trace is invariant with respect to the attitude.

(compare maps in 1st and 2nd row). However, we see for case B (2nd row) large, systematic signatures which appear to correlate with Earth's magnetic field, in particular with the magnetic equator and the magnetic poles. In case C (3rd row), where we combine the data of two star sensors instead of just one star sensor, the signatures along the magnetic equator are largely reduced. This implies that these signatures are caused by systematic errors in the star sensor attitude data which are reduced in the combination of star sensors. The special structure of the errors may result from the fact that the attitude is controlled by magnetic torquers. Because the magnetic torquers are not able to control the attitude about the direction of the magnetic field lines, the attitude of the satellite changes slightly within a couple of degrees with respect to the flight direction. This leads to a systematic yaw motion at poles and a systematic role motion at magnetic equator. Further investigations are needed to confirm this hypothesis. When we also interpolate the ICMs in the calibration of CM and DM accelerations (case D, 4th row), also the signature near the magnetic poles is largely reduced. As discussed in Sect. 7.1, this particular signature is caused by the false mapping of CM accelerations onto DM acceleration. However, we still see a small signature along the magnetic equator in the trace for case D. This implies that even after all efforts to improve the processing, further improvements might still be possible. Future investigations will have to identifiy the mechanism which causes this signature.

Similar discussions can be made for the gravity gradients V_{xx}, V_{yy} and V_{zz} shown in Fig. 27– 30, respectively. The gravity gradient V_{xz} is special due to its high sensitivity to the attitude. Note that we see the signature along the magnetic equator most clearly for V_{xz}. This hints that investigating attitude related issues such as systematic star sensor errors, errors in the relative alignment of the star sensors and the gradiometer and so on, could be a good starting point for future investigations.

8.2.2 Impact on gravity field model

In this Section, we analyze the impact of the upgrades on the level gravity field models. We compare the spherical harmonic coefficients of the gravity field models case A–E to those of the ITG-Grace2010s and EGM2008 gravity field models which serve as reference models. Note that the reference models are independent of GOCE data. Since the GOCE satellite has an inclination of 96.7°, a small area around the geographic poles is not covered by orbital tracks. We call these areas the polar gaps. Within the polar gaps, the gravity field models case A–E are not supported by measurements, which leads to large errors in the zonal and near zonal coefficients [ESA(2000)]. For this reason, we compare the degree standard deviation as well as the degree median. The latter is largely unaffected by the large errors in the zonal and near zonal coefficients and, therefore, reflects the accuracy of the models case A–E outside the polar gaps more realistically. The degree standard deviation is affected by the large errors in zonal and near zonal coefficients. Thus, degree standard deviations reflect partly the errors of the models case A–E inside the polar gaps.

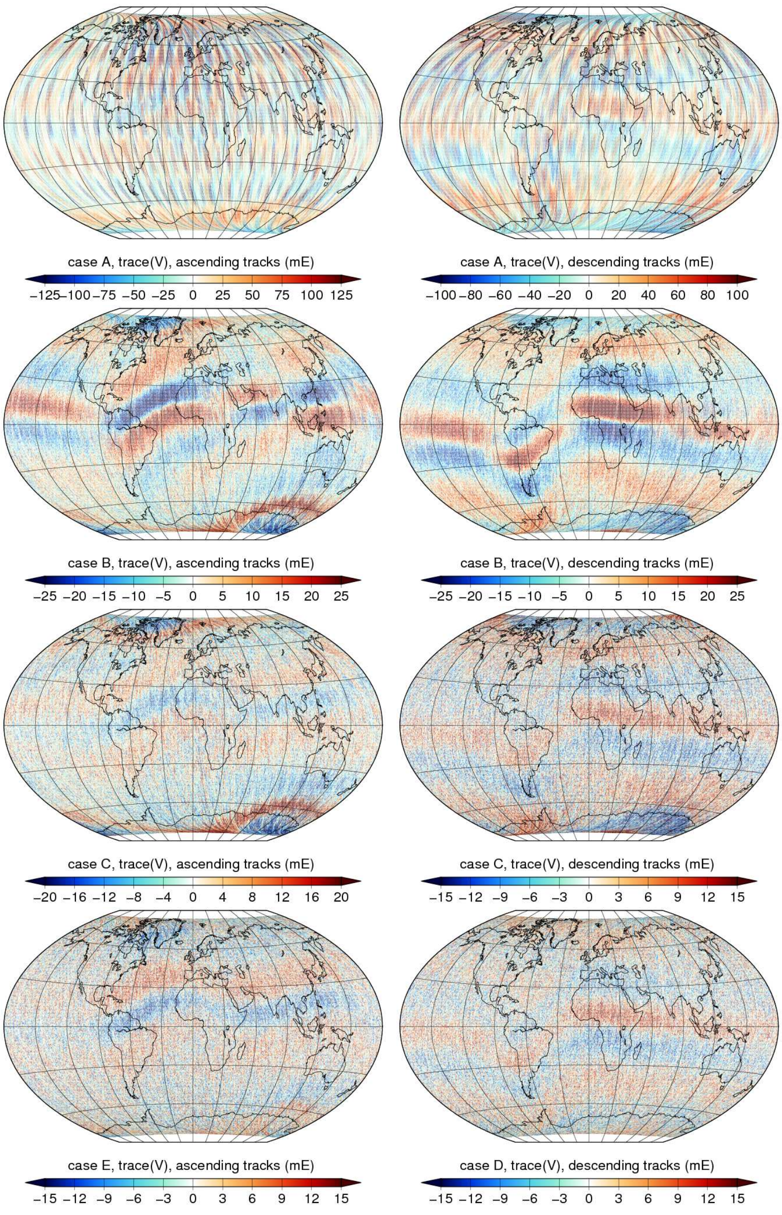

Figure 26: Gravity gradient trace for case A–E, filtered to 1–50 mHz.

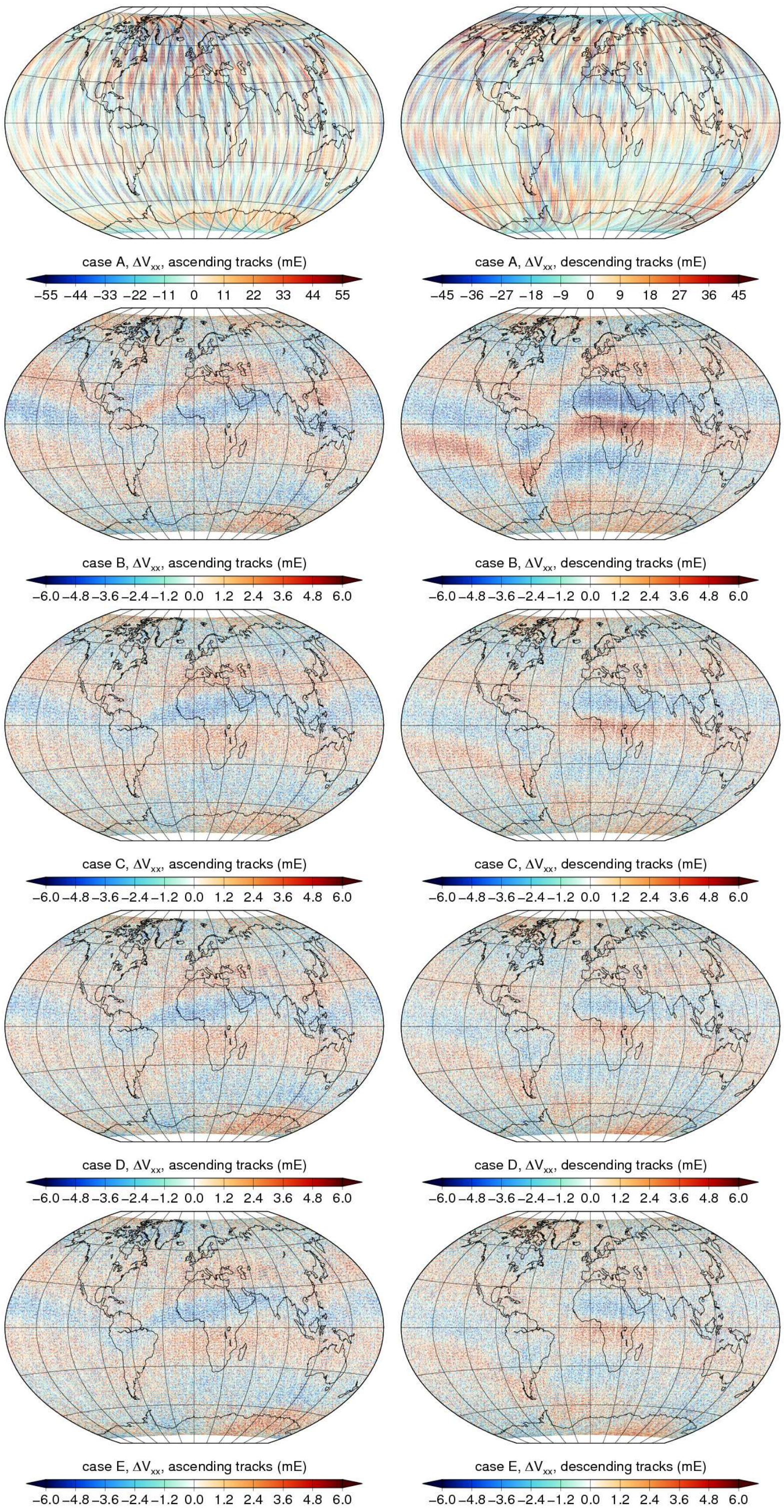

Figure 27: Differences of gravity gradient V_{xx} to the ITG-Grace2010s model for case A–E, filtered to 1–50 mHz.

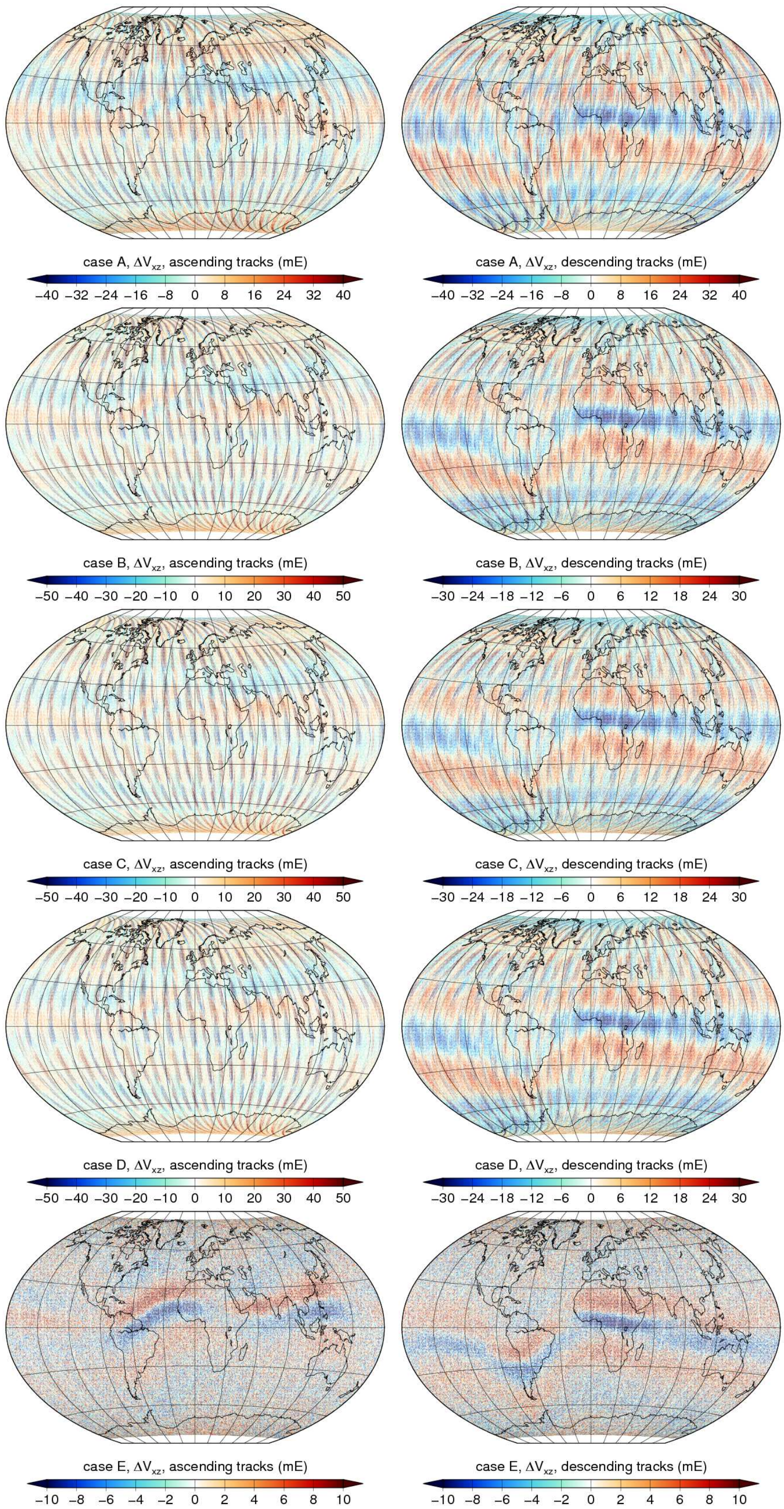

Figure 28: Differences of gravity gradient V_{xz} to the ITG-Grace2010s model for case A–E, filtered to 1–50 mHz.

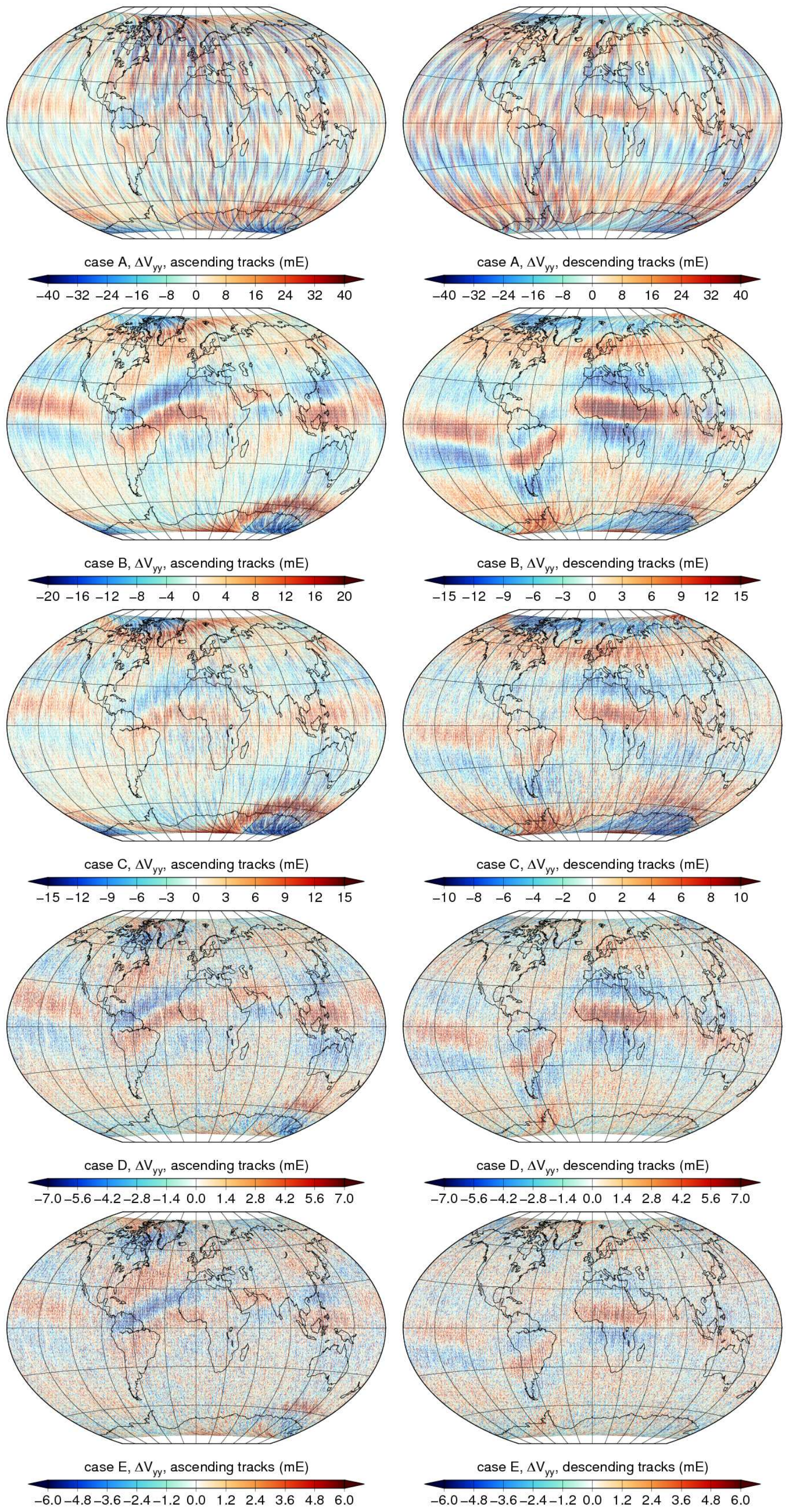

Figure 29: Differences of gravity gradient V_{yy} to the ITG-Grace2010s model for case A–E, filtered to 1–50 mHz.

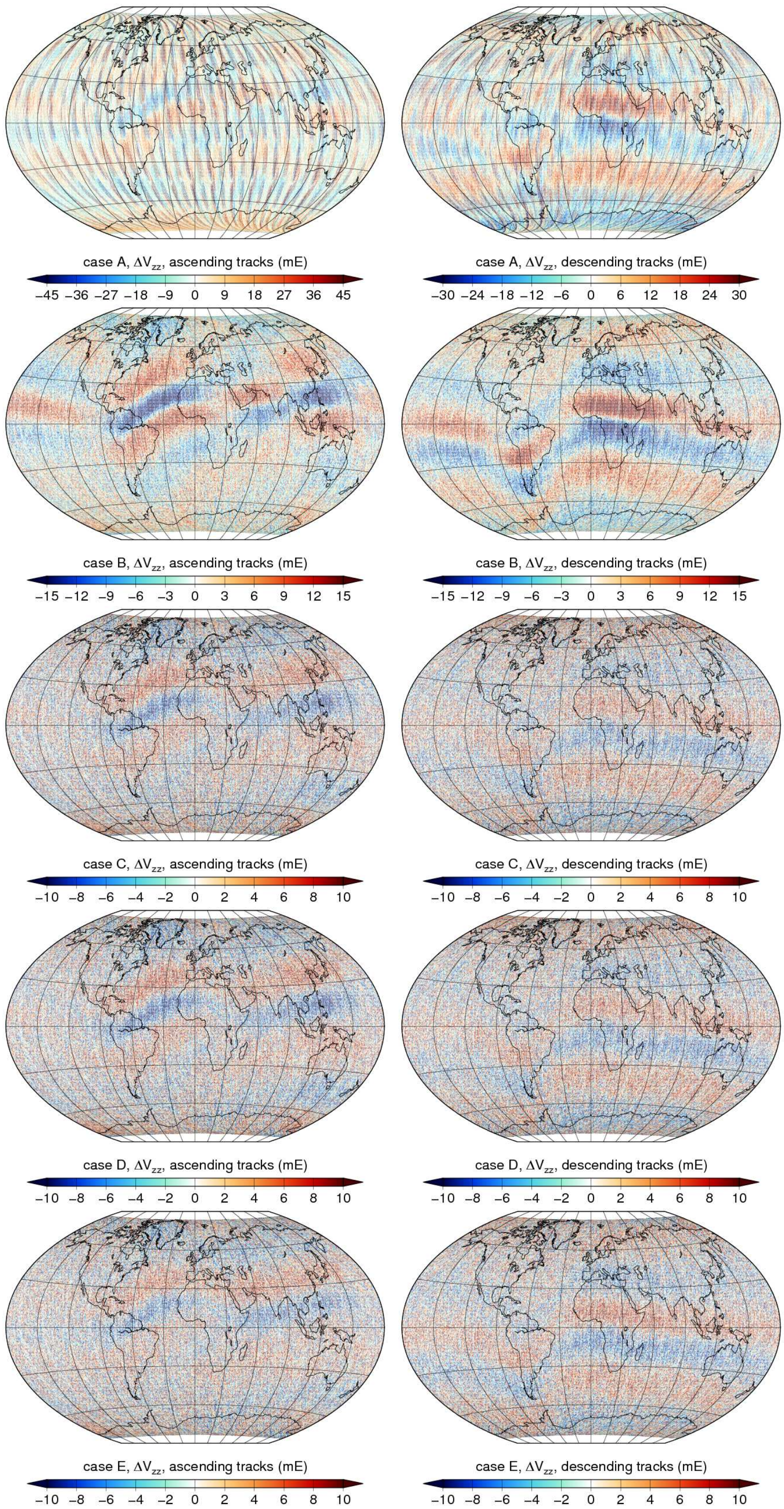

Figure 30: Differences of gravity gradient V_{zz} to the ITG-Grace2010s model for case A–E, filtered to 1–50 mHz.

Fig. 31 shows the reference signal (black solid lines and plus signs) and its formal errors (black dots and circles). Furthermore, it shows the absolute difference of the signal between the reference models and cases A–E (coloured solid lines and plus signs) and the formal errors of cases A–E (coloured dots and circles).

When we compare the degree median of the formal errors of the reference models (black dots) with that of case A–E (coloured dots) in Fig. 31, we observe that EGM2008 has larger formal errors than case A–E for spherical harmonic degrees 50-150. For ITG-Grace2010s, we observe larger errors than those of case A–E above degree 140. Therefore, we use EGM2008 as a reference above degree 160 and ITG-Grace2010s bellow degree 120, such that our reference is several times more accurate than cases A–E. This implies that the degrees 120–160 of cases A–E, which are based on only two months of gradiometer data, are already so accurately determined by GOCE that it is very difficult to validate these with independent data.

The degree standard deviation of the formal errors (coloured circles) of cases A–E shows a large bulge between degrees 20–190, which reflects the polar gap problem. An interesting feature is that the polar gap problem is slightly smaller for case E than for the other cases. This is confirmed by the degree standard deviation of signal differences (coloured plus signs). Thus, the upgrade of the attitude reconstruction helps to reduce the polar gap problem.

When comparing the degree median of the formal errors (coloured dots) of cases A–E, we see that every upgraded step of the processing reduces the formal errors. Comparing case A and B (red vs. blue dots) shows the improvement due to the upgraded angular rate reconstruction, which causes a large improvement in the degrees 2–80. The combination of star sensor (case C vs. B, blue vs. cyan dots) data gives another small improvement in the same range of degrees. The interpolation of the ICMs in the calibration of DM and CM acceleration improves all degrees (case D cs. C, cyan vs. magenta dots). This can be explained in the following way. By interpolating the ICMs, we remove a local signature near the magnetic poles (cf. Sect. 7.1). Since a local signature in the spatial domain spreads almost evenly over all degrees in the domain of spherical harmonics, we see an improvement for all degrees. The upgraded attitude reconstruction gives another minor improvement (case E vs. D, green vs. magenta dots). The degree median of the absolute signal differences confirms these observations, which indicates that the formal errors represent the real errors well. In summary, Fig. 31 demonstrates the largest improvements are due to the upgraded angular rate reconstruction and the interpolation of the ICMs in the calibration of DM and CM accelerations.

Another valuable tool for the analysis of gravity field models case A–E is the cumulative error per degree. Fig. 32 shows the cumulative errors per degree in terms of geoid heights and gravity anomalies. The cumulation has been performed starting at the highest degree, which is not according to common practice. However, this provides a better inside since the largest errors of models A–E are in the low degrees. Thus, if we started the cumulation at the lowest degree, the cumulative error would increase dramatically at the lower degrees and, therefore, we would not see any differences between the models A–E at higher degrees. Moreover, gravity gradient

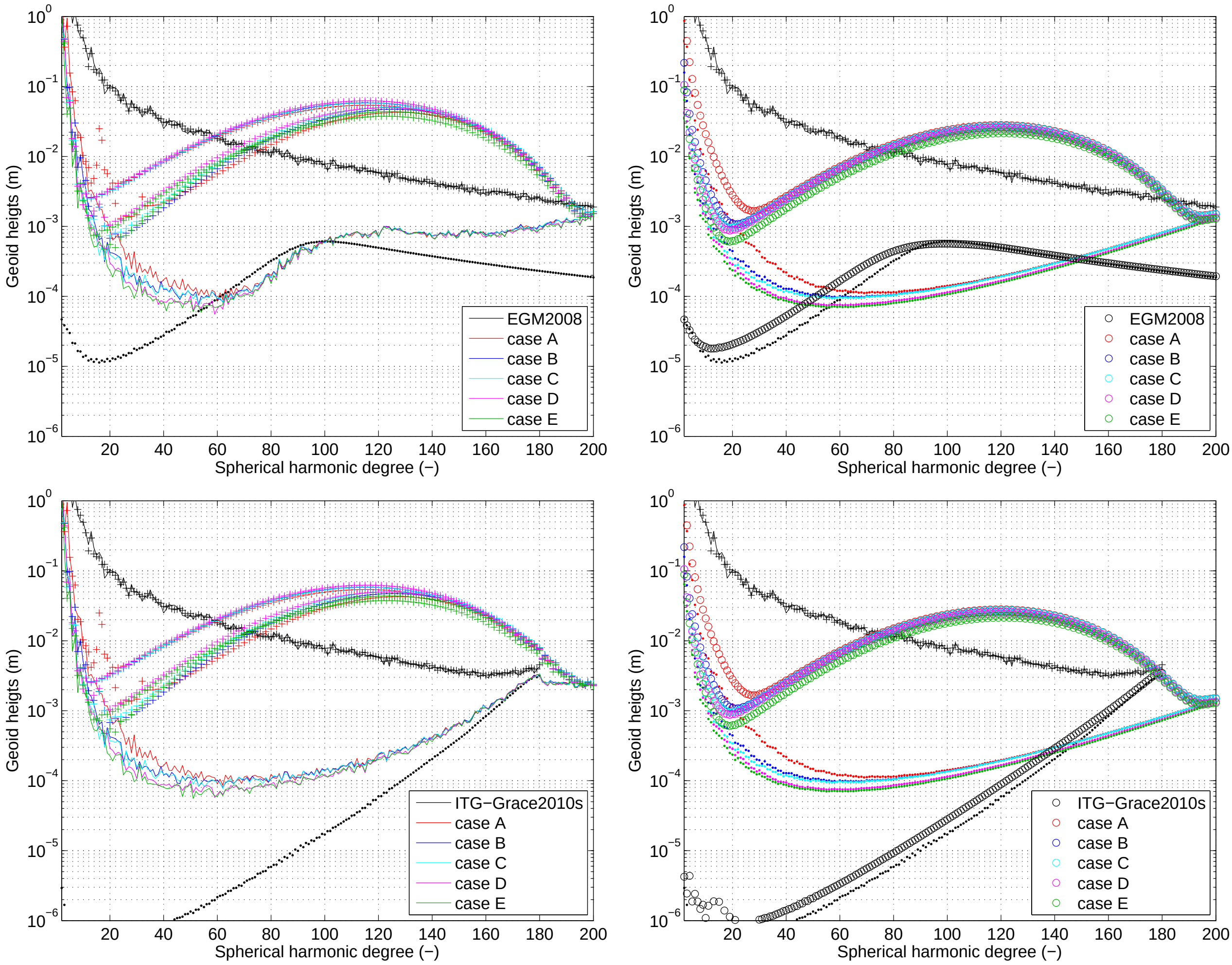

Figure 31: Comparison of the gravity field models case A–E to the EGM2008 (top row) and ITG-Grace2010s models (bottom row). The black solid lines and the black plus signs show the degree median and the degree standard deviation, respectively, of the signal in the EGM2008 and ITG-Grace2010s models. Other solid lines and plus signs reflect the degree median and degree standard deviation, respectively, of the signal differences of case A–E to EGM2008 and ITG-Grace2010s. Dots and circles show the degree median and the degree standard deviation, respectively, of the formal errors in the models. Note that the degree median of signal differences has been scaled by 1.4826 to match the corresponding degree standard deviations.

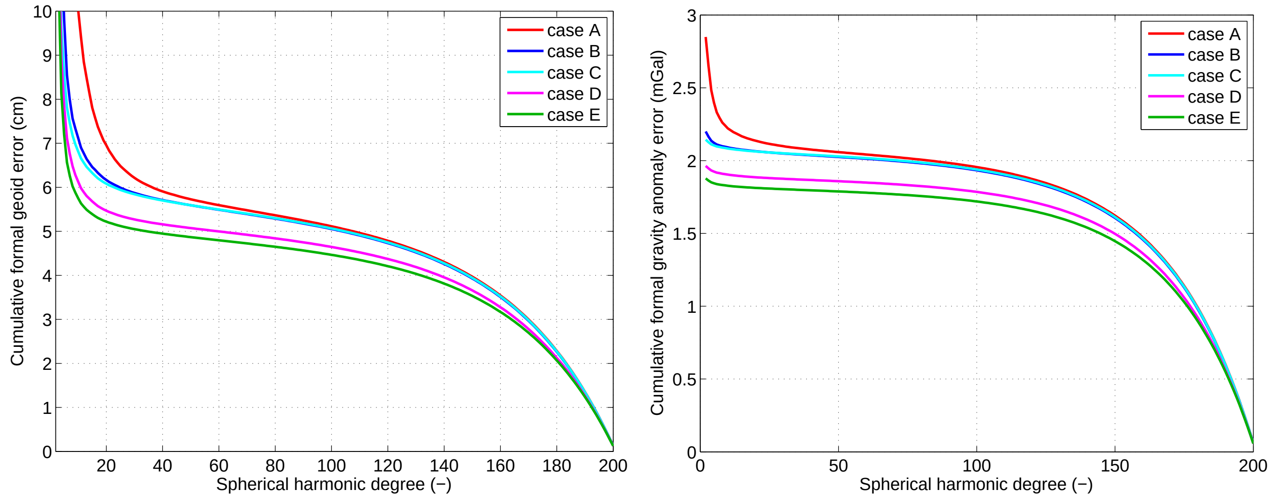

Figure 32: Cumulative formal geoid height errors (left panel) and cumulative formal gravity anomaly errors (right panel). The cumulation starts at degree 200 and ends at degree 2. The basis for the cumulation is the degree median of the standard deviations.

data is usually complemented by satellite-to-satellite tracking (SST) data, from which the long wavelength part of the gravity field model is estimated. Thus, by starting the cumulation at the highest degree, we can draw some conclusions for gravity field models based on gravity field models based on gravity gradient and SST data. The cumulative errors in Fig. 32 confirm the observation in Fig. 31 that the interpolation of the ICMs has the largest effect on the higher degrees (magenta vs. cyan line). Moreover, the upgraded angular rate reconstruction mainly affects the degrees bellow 80 (red vs. blue line). Surprisingly, the upgraded attitude reconstruction (green vs. magenta line) has the second largest impact on the cumulative errors, starting at degree 170 and continuing downwards. This could not be seen in Fig. 31, which can be explained by the fact that the differences between the models D and E are small but significant and within that range of degrees where neither ITG-Grace2010s or EGM2008 can serve as a reference.

Fig. 33 and 34 show maps of the differences of case A–E to the EGM2008 model in terms of geoid heights and gravity anomalies, respectively. In the creation of these maps, we omitted the spherical harmonic degrees 2–9 because the errors of case A–E in these degrees are so large that they would obscure every other error. Furthermore, it is emphasized that gravity gradient data will be ultimately combined with GPS-SST data, from which the low degree spherical harmonic coefficients are determined much more accurately. Therefore, omitting degrees 2–9 allows us to focus on those wavelengths which are more important in view of a gravity field model based on gravity gradient and GPS SST data.

In the top row of Fig. 33, we see the difference of case A to EGM2008. The most prominent feature is the north-south striping between ±60° degrees latitude in the order of ±60 cm. The striping is caused by large errors in the sectorial and near sectorial coefficients of spherical harmonic degree 16. These coefficients suffer from large errors in the gravity gradients at the orbital harmonic frequency and multiples thereof, i.e. 1, 2, 3, ... cycles-per-revolution corresponding to 0.186, 0.372, 0.558, ... mHz. These errors are clearly visible in Fig. 20. The left panel of the second row shows the differences of case B to EGM2008. The north-south striping is not visible any more, which indicates that the errors in the gravity gradients at the orbital harmonic frequency and multiples thereof are largely reduced by the upgraded angular rate reconstruction. The largest remaining differences are in the Amazon basin and the Andes in South America, Central Africa, and the Himalayas in Asia. Since these are regions where EGM2008 is either not supported by terrestrial gravity data or supported by terrestrial data of lower quality, we consider these differences to be errors in EGM2008. The right panel in the second row shows the differences between case A and B. Apart from the north-south striping, the differences are very smooth, which is in accordance to our observation in Fig. 31 that improvements due to the upgraded angular rate reconstruction are in the degree 2–60.

The left and right panel of the third row show the differences of case C to EGM2008 and case B, respectively. The latter shows a signature along the magnetic equator with a magnitude of ±6 cm. When we look closely at the Atlantic Ocean between South America and Africa, we can see that the signature is present in the differences of case B to EGM2008, despite the fact that it is largely obscured by short wavelength errors. In the differences of case C to EGM2008, it is even more difficult to spot the signature, which means that the combination of star sensor data removes large part of this particular error.

In the right panel of the fourth row of Fig. 20, we see the differences of case D to case C. The largest differences are near the magnetic south pole, which is located south of Australia. From Table 6, we can see that the magnitude of these differences is approximately ±40 cm. The comparison to EGM2008 reveals that the differences are present for case C but not for case D. Thus, we conclude that the interpolation of the ICMs remove a large local error near the magnetic south pole.

Finally, the fifth row shows the differences of case E to EGM2008 and case D. The latter show a north-south striping similar to the one that we observed in the differences of case A to B. However, the magnitude of the striping is only ±4 cm this time. Furthermore, we see systematically negative differences of -4 cm near the geographic north pole and positive differences of +6 cm near the geographic south pole. The comparison to EGM2008 shows that these differences are present for case D but not for case E. Since such differences can be attributed to the polar gap problem, we can conclude that in particular the upgraded attitude reconstruction reduces the polar gap problem.

Fig. 34 shows the same differences as Fig. 33 expressed in gravity anomalies instead of geoid heights. Since short wavelengths are emphasised by gravity anomalies in comparison to geoid heights, we can see some features in Fig. 34 that are not easily spotted in Fig. 33. In particular, the differences of case C to B as well as E to D show many short wavelength features. When

Table 6: WRMS of the geoid height differences in Fig. 33. The weights are set to zero outside ±80° latitude in order to exclude large error in and near the polar gap.

	WRMS (cm)	Min. (cm)	Max. (cm)		WRMS (cm)	Min. (cm)	Max. (cm)
Case A vs. EGM2008	26.6	-274.7	326.1				
Case B vs. EGM2008	17.0	-287.0	318.4	Case B vs. A	19.0	-71.8	77.3
Case C vs. EGM2008	16.9	-281.8	320.0	Case C vs. B	2.6	-17.4	15.6
Case D vs. EGM2008	15.9	-283.8	325.5	Case D vs. C	5.2	-41.6	42.1
Case E vs. EGM2008	15.7	-292.2	320.9	Case E vs. D	2.9	-18.2	17.0

closely inspected, we see that these features follow the 16 regularly spaced ground tracks of GOCE's orbit. This indicates that this feature is related to the geographic sampling. This is supported by the fact that we truncate about one day of the input data due to the filtering in the angular rate and attitude reconstruction as well as in the gravity field model estimation. The inspection of the ground tracks (not shown here) reveals that the feature occurs in places the sampling density is lower due to the truncation of data. Thus, many of the short wavelength features in the differences of case B to C and D to E should vanish if we used one more day of data to compensate for the truncation. Note that this discussion does not apply to the short wavelength features in the differences of case C and D. Otherwise, the discussion for Fig. 33 applies to Fig. 34, too.

Tables 6 and 7 provide some statistics of the maps shown in Fig. 33 and 34, respectively. The statistics are the weighted root-mean-squares (WRMS), the minimum and maximum of the differences. In the computation of the statistics, we omitted all data outside ±80 degrees latitude in order to exclude the polar gap. The WRMS of the differences to of cases A–E to EGM2008 shows that each step gives a further improvement. The minimum and maximum values of the differences of cases A–E to EGM2008 reflect the errors in EGM2008 in South America, Africa and Asia. Thus, they are not useful for assessing the impact of the upgraded processing. The WRMS of the differences between the cases shows that for geoid heights the upgraded angular rate reconstruction gives the largest improvements (19 cm WRMS) while for gravity anomalies the interpolation of the ICMs gives the largest improvements. The latter are 1.4 mGal in terms of the global wrms and 11 mGal locally, which we can see from the minimum and maximum differences.

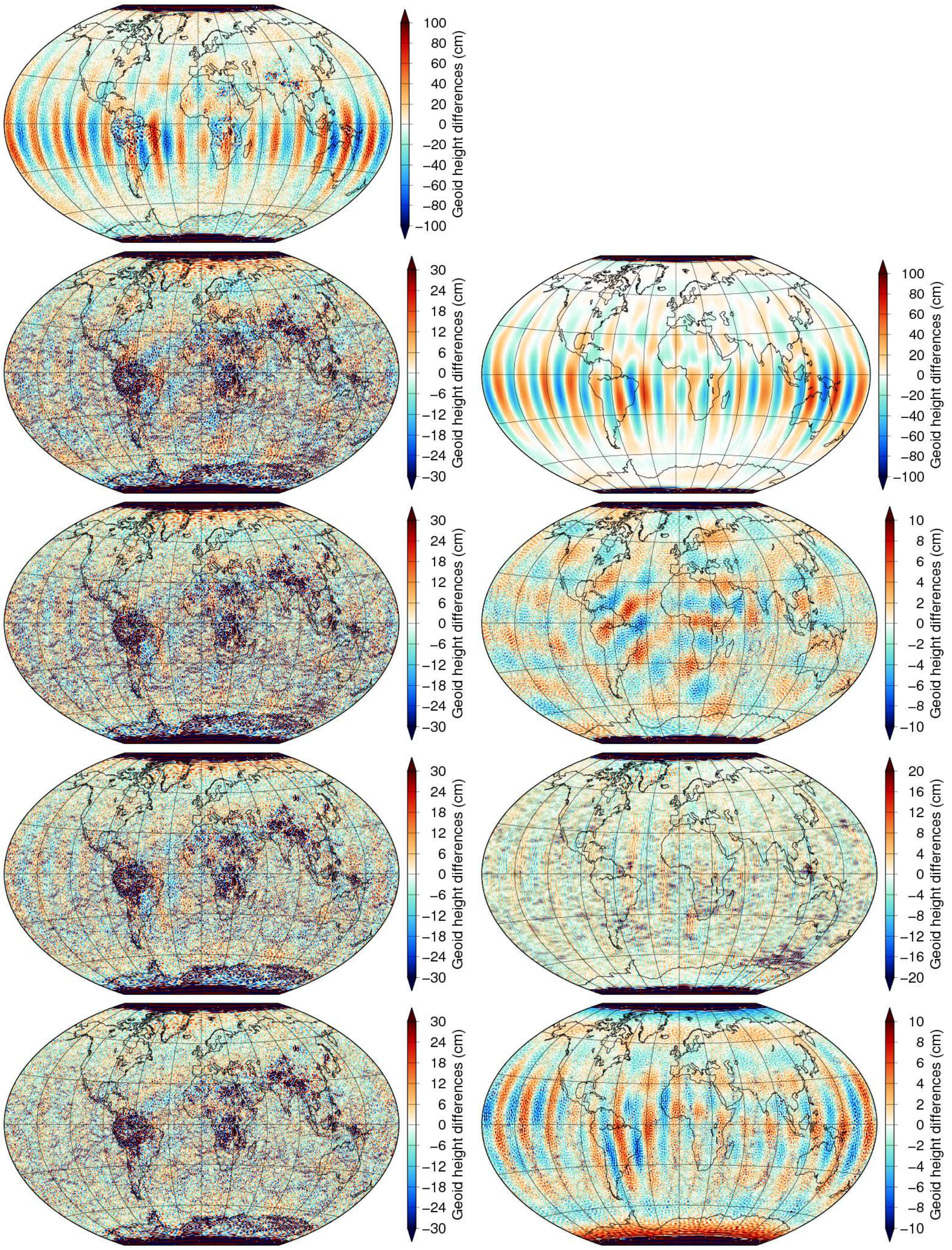

Figure 33: Improvements due to upgraded processing steps in terms of geoid heights for spherical harmonic degrees 10–200. The left column shows the differences of the models A–E to the EGM2008 model (case A–E from top to bottom). The right columns show the differences between cases A and B, B and C, C and D, as well as D and E from top to bottom.

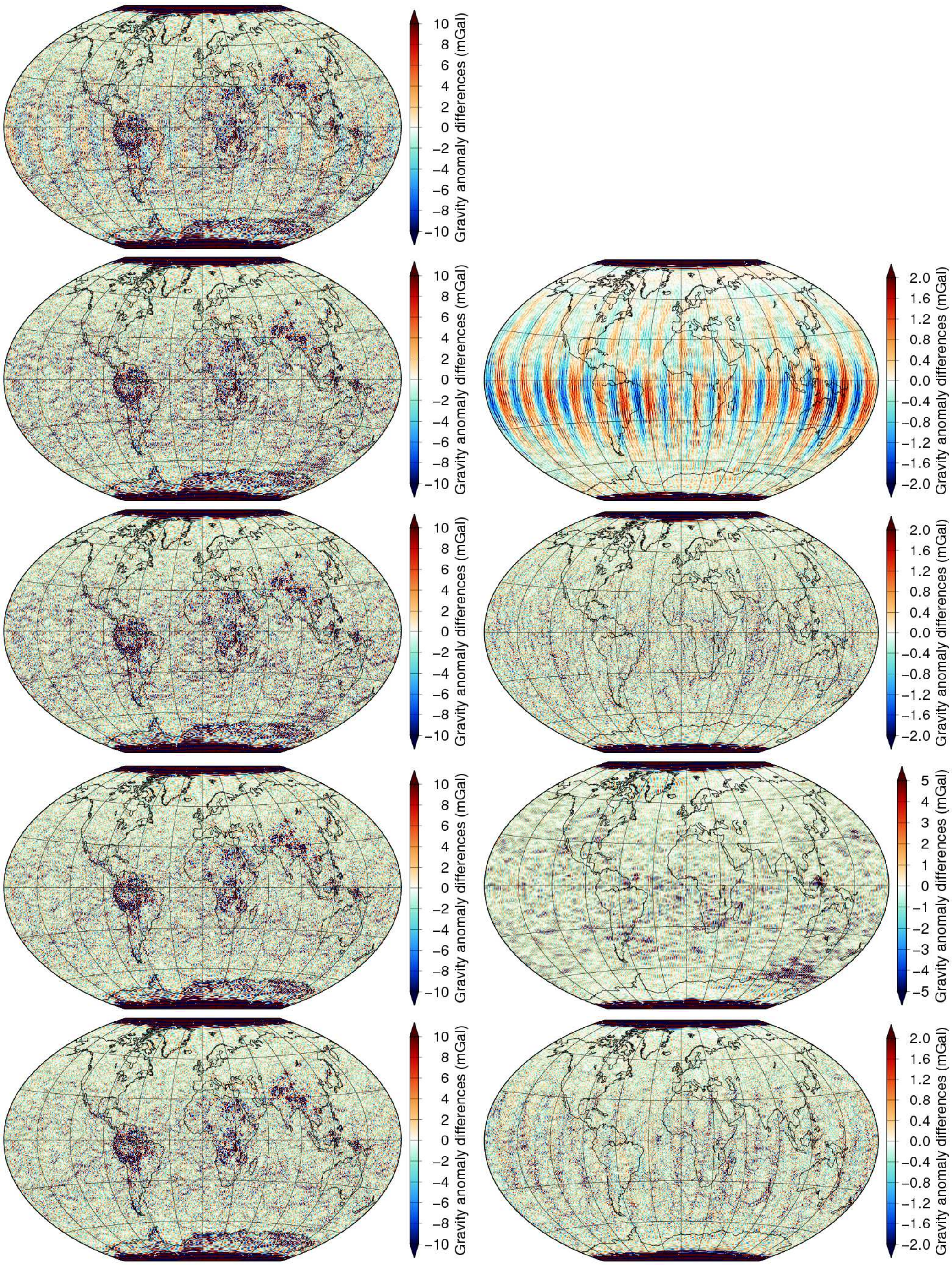

Figure 34: Improvements due to upgraded processing steps in terms of gravity anomalies for spherical harmonic degrees 10–200. The left column shows the differences of the models A–E to the EGM2008 model (case A–E from top to bottom). The right columns show the differences between cases A and B, B and C, C and D, as well as D and E from top to bottom.

Table 7: WRMS of the gravity anomaly differences in Fig. 34. The weights are set to zero outside ±80° latitude in order to exclude large error in and near the polar gap.

	WRMS (mGal)	Min. (mGal)	Max. (mGal)		WRMS (mGal)	Min. (mGal)	Max. (mGal)
Case A vs. EGM2008	4.303	-60.009	67.277				
Case B vs. EGM2008	4.261	-60.023	67.275	Case B vs. A	0.589	-2.814	3.022
Case C vs. EGM2008	4.257	-59.517	66.317	Case C vs. B	0.600	-3.957	3.797
Case D vs. EGM2008	3.967	-60.057	66.409	Case D vs. C	1.418	-11.511	11.111
Case E vs. EGM2008	3.942	-61.701	66.512	Case E vs. D	0.608	-4.012	3.607

9 Summary

We reported on two main developments for the GOCE mission: 1) the method for monitoring calibration parameters during nominal science mode and validation of the baseline, 2) the upgrade of the gradiometer level 1b processor. For both developments, we presented results for real mission data, which we validated by investigating the trace condition and comparing to non-GOCE gravity field models.

Though the calibration method also works with data of dedicated shaking events, it was developed with focus on estimating calibration parameters from data recorded during nominal science mode. The key feature of the method is the stochastic model for taking correlations into account. We estimated time series of calibration parameters for monitoring of their temporal evolution during nominal science mode. In addition, we validated the baseline's calibration parameters. A major finding from the results for data of 11/2009–5/2010 is that some calibration parameters show significant drifts between shaking events, which can be well approximated by linear interpolation. Further, we found a correction for the differential scale factor $\Delta s_{25,y}$, which largely reduces artefacts in the gravity gradient V_{yy} near the magnetic poles. The global RMS of the difference of V_{yy} to ITG-Grace2010s could be reduced from 3.88 mE to 3.26 mE, when filtered to the measurement band.

Based on that experience, we analyzed data of 3/2011–4/2011. Since the beginning of 2011, solar activity increased, leading to worse drag conditions, which in turn cause larger artefacts near the magnetic poles. The increased drag is reflected by CM accelerations, which have increased by a factor of three. We found that correcting $\Delta s_{25,y}$ alone does not reduce the artefacts satisfactorily. A systematic analysis of all possible error sources related to the calibration parameters identified four additional calibration parameters as candidates for correction. However, we were still not able to find corrections for these calibration parameters, which would reduce the artefacts satisfactorily. Thus, we conclude that the calibration parameters are not the only source leading to artefacts in the gradients near the magnetic poles. Future research will focus on identifying other sources which could cause these artefacts.

The gradiometer processing was designed based on pre-launch simulations. However, the actual performance of the gradiometer differs from the one assumed pre-launch. The gradiometer noise is larger than expected in the measurement band 5–100 mHz while it is lower than expected bellow 5 mHz. For this reason, the gradiometer level 1b processing was revisited. In particular, the finding that the interpolation of calibration parameters leads to a significant improvement of the gradients, triggered the investigations. We found that three steps in the processing could be improved and added one new step:

- The combination of data from two or three star sensors was introduced as a new step in the processing. While a single star sensor measures the attitude about the boresight less accurate by a factor of 10, the combined attitude does have this weakness.

- The calibration of accelerations is improved by linearly interpolating the ICMs between two shaking events. This prevents largely the leakage of CM accelerations into gravity gradients. Whether the correction of the differential scale factor $\Delta s_{25,y}$ of -36×10^{-6} will be used in the reprocessing of level 1b data is currently in discussion.

- The reconstruction of the angular rates is improved. We now use a Wiener filter to reconstruct the angular rates from the gradiometer and star sensor data. The advantage is that it makes use of the full noise characteristics of the gradiometer and star sensor data while its filter transient is very short (1.5 orbital revolutions) compared to that of the Kalman filter which is used in the old processing (8 orbital revolutions).

- The reconstruction of the attitude is improved. In the old processing, a Kalman filter performed the reconstruction of the angular rates as well as the attitude. In the new processing, we integrate the reconstructed angular rates to obtain integrated attitude quaternions. We use quaternions of the star sensor combination to initialize the integration. Then, we use the Wiener filter of the angular rate reconstruction for merging the integrated quaternions with the quaternions of the star sensor data combination.

The impact of these steps was analyzed step-by-step on the level of gravity gradients as well as gravity field models (level 1b and level 2). We found that for the gravity gradients V_{xx} and V_{zz} the angular rate reconstruction, for V_{yy} the interpolation of ICMs, and for V_{xz} the attitude reconstruction and star sensor combination are the most important steps. All improvements in the gravity gradients are bellow 30 mHz in the PSD. For V_{yy}, the improvement is related to reducing artefacts near the magnetic poles. The maps of the differences of the gravity gradients to ITG-Grace2010s show that some systematic effects remain in the gravity gradients. This indicates that further improvements of the level 1b gradiometer processing might be possible. Further, we compared gravity field models estimated from the gravity gradients to the EGM2008 and ITG-Grace2010s models. In the comparison in the spatial domain, we excluded the spherical harmonics degrees 2–9, which are not accurately determined from the gravity gradient data. The differences to EGM2008 in terms of geoid heights were reduced from 26.6 cm for the old processing to 15.7 cm for the upgraded processing. However, the largest part of that improvement is found in the long wavelengths. This means that for a gravity field model estimated from gravity gradients and GPS-SST data, we expect the improvement to be much smaller. Nevertheless, it should be emphasized there are users who work with gravity gradients directly rather than gravity field models.

It should be noted that the investigations contributed to an upgrade of the gradiometer level 1b processor and a subsequent reprocessing of gradiometer level 1b data. Today (21st November 2011), the upgrade of the gradiometer level 1b processor is integrated into the level 1b processor and the reprocessing is ongoing.

Acknowledgements

I would like to thank Roger Haagmans, Gernot Plank, Michael Kern, Rune Floberghagen, Michael Fehringer and Björn Frommknecht for their support, Daniel Lamarre for his support, sharing his knowledge and providing the data recorded during the satellite shakings including the results of the baseline method for the calibration of the gradiometer in the ground processing, Claudia Stummer for a fruitful collaboration and exchange of knowledge, Pieter Visser and Jose van den IJssel for providing quaternions describing the rotation from the Earth-fixed to the inertial reference frame and the orbits of GOCE. I also acknowledge the valuable remarks of Johannes Bouman on the developed calibration method.

A Robust trend estimation

In this section we explain the robust trend estimation method, which be can considered as a variant of the Danish method [Crüger Jørgensen et al.(1984)]. Let

$$\boldsymbol{l} + \boldsymbol{v} = \boldsymbol{A}\boldsymbol{x} \tag{173}$$

be the observation equations of the trend estimation problem, where $\boldsymbol{l}$ are the observations, $\boldsymbol{v}$ are residuals, $\boldsymbol{A}$ is the design matrix and $\boldsymbol{x}$ are the parameters. The parameters are estimated by

$$\boldsymbol{x} = (\boldsymbol{A}^T \boldsymbol{P} \boldsymbol{A})^{-1} \boldsymbol{A}^T \boldsymbol{P} \boldsymbol{l}, \tag{174}$$

where $\boldsymbol{P}$ is a diagonal weighting matrix. The diagonal elements of $\boldsymbol{P}$ are computed according to

$$P_{n,n} = \exp(-\boldsymbol{v}_n^2 / s_{\mathrm{MAD}}^2), \tag{175}$$

where s_{MAD} is a robust estimate of the standard deviation based on the median absolute deviation (MAD) [Venables and Ripley(2002), pp 121–122],

$$\begin{aligned} s_{\mathrm{MAD}} &= 1.4826 \times \mathrm{MAD}(\boldsymbol{v}) \\ &= 1.4826 \times \mathrm{median}(|\boldsymbol{v} - \mathrm{median}(\boldsymbol{v})|) \end{aligned} \tag{176}$$

of the residuals $\boldsymbol{v}$. The factor 1.4826 makes the MAD consistent with the standard deviation of normal distributed residuals. The estimation of the parameters $\boldsymbol{x}$ are initialized by $\boldsymbol{P} = \boldsymbol{I}$, and then iterated using in each iteration the new weighting matrix according to Eq. (175). The covariance matrix of the final parameters is obtained by

$$\boldsymbol{x} = (\boldsymbol{A}^T \boldsymbol{P} \boldsymbol{A})^{-1} s_{\mathrm{MAD}}^2. \tag{177}$$

References

[Bigazzi and Frommknecht(2010)] Bigazzi A, Frommknecht B (2010) Note on GOCE instruments Positioning. XGCE-GSEG-EOPG-TN-09-0007, Frascati, Italy. http://earth.esa.int/download/goce/

[Bouman et al.(2009)] Bouman J, Rispens S, Gruber T, Koop R, Schrama E, Visser P, Tscherning CC, Veicherts M (2009) Preprocessing of gravity gradients at the GOCE high-level processing facility. J Geod 83:659–678. doi:10.1007/s00190-008-0279-9

[Bouman et al.(2010)] Bouman J, Stummer C, Murböck M, Fuchs M, Rummel R, Pail R, Gruber T, Bosch W, Schmidt M (2010) GOCE gravity gradients: a new satellite observable. Geotechnologien Science Report No. 17: Observation of the System Earth from Space, pp 52–61. http://www.geotechnologien.de/portal/cms/Geotechnologien/Oeffentlichkeit/Download/Science+Reports, last accessed 06/10/2011

[Bouman et al.(2011)] Bouman J, Fiorot S, Fuchs M, Gruber T, Schrama E, Tscherning C, Veicherts M, Visser P (2011) GOCE gravitational gradients along the orbit. J Geod, under review

[Cesare(2008)] Cesare S (2008) Performance requirements and budgets for the gradiometric mission. Issue 4 GO-TN-AI-0027, Alenia Spazio, Turin

[Cesare and Catastini(2008)] Cesare S, Catastini G (2008) Gradiometer on-orbit calibration procedure analysis. Issue 3 GO-TN-AI-0069, Alenia Spazio, Turin

[Crüger Jørgensen et al.(1984)] Crüger Jørgensen P, Frederiksen P, Kubik K, Weng W (1984) Ah, robust estimation! Proc. of the XV Congress of ISPRS, Commision III, 268–277, Rio de Janeiro

[Drinkwater et al.(2007)] Drinkwater M, Haagmans R, Muzzi D, Popescu A Floberghagen R, Kern M, Fehringer M (2007) The GOCE gravity mission: ESA's first core explorer. In: 3rd GOCE user workshop, 6–8 November 2006, Frascati, Italy. ESA SP-627, pp 1–7

[ESA(1999)] ESA (1999) The four candidate Earth Explorer core missions - gravity field and steady-state ocean circulation. Reports for mission selection, ESA SP-1233(1).

[ESA(2000)] ESA (2000) From Eötvös to mGal. Final report, ESA/ESTEC Contract No. 13392/98/NL/GD.

[European GOCE Gravity Consortium(2008)] European GOCE Gravity Consortium (2008) GOCE Level 2 product data handbook. Issue 4, GO-MA-HPF-GS-0110

[Fehringer(2008)] Fehringer M, Andre G, Lamarre D, Maeusli D (2008) A Jewel in ESA's Crown. ESA Bulletin 133:14–23 www.esa.int/esapub/bulletin/bulletin133/bulletin133.pdf

[Foerste et al.(2008)] Foerste C, Flechtner F, Schmidt R, Stubenvoll R, Rothacher M, Kusche J, Neumayer K-H, Biancale R, Lemoine J-M, Barthelmes F, Bruinsma J, Koenig R, Meyer U (2008) EIGEN-GL05C - A new global combined high-resolution GRACE-based gravity field model of the GFZ-GRGS cooperation. General Assembly European Geosciences Union, Vienna, Austria, Geophysical Research Abstracts, Vol. 10, Abstract No. EGU2008-A-06944. http://op.gfz-potsdam.de/grace/results/grav/g007_eigen-05c_files/foerste_EGU2008-A-03426.pdf, last accessed 07/10/2011

[Frommknecht et al.(2011)] Frommknecht B, Lamarre D, Meloni M, Bigazzi A, Floberghagen R (2011) GOCE Level 1b Processing. J Geod, under revision.

[Harris(1978)] Harris F (1978) On the use of Windows for Harmonic Analysis with the Discrete Fourier Transform. Proc IEEE 66(1):51-83

[Jørgensen(2003)] Jørgensen J (2003) ASC GOCE design and performance report. Technical Note to ESA, GO-RP-DTU-2018, Issue 1.1.

[Kern et al.(2007)] Kern M, Haagmans R, Plank G, Floberghagen R, Drinkwater M (2007) In-flight validation and monitoring of gradiometric GOCE data. In: Proc. of the 3rd International GOCE User Workshop, 6–8 November 2006, Frascati, Italy, pp 141–148

[Liebe(2002)] Liebe CC (2002) Accuracy performance of star trackers – a tutorial. IEEE Trans Aerosp Electron Syst, 38(2):587–599.

[Lühr(2007)] Lühr H, Rentz S, Ritter P, Liu H, Häusler K (2007) Average thermospheric wind patterns over the polar regions, as observed by CHAMP. Ann Geophys 25:1093-1101

[Mayer-Gürr et al.(2011)] Mayer-Gürr T, Kurtenbach E, Eicker A (2011) ITG-Grace2010. Webpage, Institut für Geodäsie und Geoinformation, http://www.igg.uni-bonn.de/apmg/index.php?id=itg-grace2010, last accessed 06/10/2011

[NOAA/Space Weather Prediction Center(2009)] NOAA/Space Weather Prediction Center (2009) Solar Cycle Progression. http://www.swpc.noaa.gov/SolarCycle Accessed 20 Apr. 2011

[Pavlis et al.(2008)] Pavlis N, Holmes S, Kenyon S, Factor J (2008) An Earth Gravitational Model to Degree 2160: EGM2008. Presented at EGU General Assembly 2008, Vienna, Austria. http://earth-info.nga.mil/GandG/wgs84/gravitymod/egm2008/NPavlis&al_EGU2008.ppt, last accessed 07/10/2011

[Peterseim et al.(2011)] Peterseim N, Schlicht A, Stummer C, Yi W (2011) Impact of cross winds in polar regions on GOCE accelerometer and gradiometer data. In: Proc. of the 4th International GOCE User Workshop, 31 March–1 April 2011, Munich, Germany. ESA SP-696

[Petit and Luzum(2010)] Petit G, Luzum B (2010) IERS Conventions. IERS Technical Note No. 36, Verlag des Bundesamtes für Kartographie und Geodäsie, Frankfurt am Main, Germany. http://tai.bipm.org/iers/conv2010/conv2010.html

[Rispens and Bouman(2009)] Rispens S, Bouman J (2009) Calibrating the GOCE accelerations with star sensor data and a global gravity field model. J Geod 83:737–749. doi:10.1007/s00190-008-0290-1

[Rispens and Bouman(2011)] Rispens S, Bouman J (2011) External calibration of GOCE accelerations to improve derived gravitational gradients. J Geod Sci 1(2):114–126. doi:10.2478/v10156-010-0014-3

[Romans(2003)] Romans L (2003) Optimal combination of quaternions from multiple star cameras. Technical report, Jet Propulsion Laboratory. `ftp://podaac.jpl.nasa.gov/allData/grace/docs/quaternion_memo.pdf`

[Schuh(1996)] Schuh W-D (1996) Tailored numerical solution strategies for the global determination of the Earth's gravity field. Mitteilungen der geodätischen Institute der TU Graz, Folge 81

[SERCO/DATAMAT Consortium(2008)] SERCO/DATAMAT Consortium (2008) GOCE L1b products user handbook. Issue 2, GOCE-GSEG-EOPG-TN-06-0137

[Siemes et al.(2011)] Siemes C, Haagmans R, Kern M, Plank G, Floberghagen R (submitted) Calibration of the GOCE gradiometer - methodology and results. submitted to J Geod

[Stummer et al.(2011)] Stummer C, Fecher T, Pail R (2011) Alternative method for angular rate determination within the GOCE gradiometer processing. J Geod. DOI 10.1007/s00190-011-0461-3

[Stummer et al.(2011)] Stummer C, Siemes C, Pail R, Frommknecht B, Floberghagen R (submitted) Upgrade of the GOCE Level 1b gradiometer processor. submitted to Adv Space Res

[Stummer et al.(2011)] Stummer C, Siemes C, Pail R, Frommknecht B, Floberghagen R (2011) Upgrade of the GOCE Level 1b gradiometer processor. Adv Space Res (under review)

[Tapley et al.(2004)] Tapley B, Bettadpur S, Watkins M, Reigber C (2004) The gravity recovery and climate experiment: mission overview and early results. Geophys Res Lett 31:L09607. doi:10.1029/2004GL019920

[Venables and Ripley(2002)] Venables W, Ripley B (2002) Modern applied statistics with S, fourth edition. Springer, New York. ISBN 0-387-95457-0

[Visser(2008)] Visser P (2008) Exploring the possibilities for star-tracker assisted calibration of the six individual GOCE accelerometers. J Geod 82:591–600. doi:10.1007/s00190-007-0205-6

[Visser(2009)] Visser P, van den IJssel J, van Helleputte T, Bock H, Jäggi A, Beutler G, Švehla D, Hugentobler U, Heinze M (2009) Orbit determination for the GOCE satellite. Adv Space Res 43:760–768. doi:10.1016/j.asr.2008.09.016

[Welch(1967)] Welch PD (1967) The use of Fast Fourier Transform for the estimation of power spectra: A method based on time averaging over short modified periodograms. IEEE Trans Audio Electroacoust, AU-15:70–73